The Dynamical States and Mass Accretion Histories of Galaxy Clusters in IllustrisTNG

by

Rashaad Reid

A thesis
presented to the University of Waterloo
in fulfilment of the
thesis requirement for the degree of
Master of Science
in
Physics

Waterloo, Ontario, Canada, 2025

© Rashaad Reid 2025

Author's Declaration

I hereby declare that I am the sole author of this thesis. This is a true copy of the thesis, including any required final revisions, as accepted by my examiners.

I understand that my thesis may be made electronically available to the public.

Abstract

The concordance cosmological model describes the history and large-scale structure of the universe using a few key parameters. Two of these parameters, σ_8 and Ω_m, determine the clustering of matter due to the growth of density fluctuations in the early universe. Current constraints on these parameters measured from nearby large structures and from the early universe are in statistical tension. Our ability to resolve this tension is limited by the degeneracy between the parameters when measured from observations of nearby structure. Since galaxy clusters are the most massive gravitationally bound objects in the universe, their formation is sensitive to σ_8 and Ω_m. An improved understanding of the formation histories of galaxy clusters can break the measurement degeneracy, thus providing new insights into this tension in our cosmological model. Since the formation time scales of galaxy clusters are unobservable, we must use the structure of clusters to probe their formation histories.

In this thesis, we relate the observable structural properties of galaxy clusters to the mass accretion histories of their surrounding dark matter halos in the IllustrisTNG cosmological simulations. Structure formation in the universe is hierarchical, so recently formed galaxy clusters will have experienced recent mergers with other systems. We examine a set of structural properties that are related to the dynamical states of clusters as indications of recent mergers to relate the structures of clusters to their formation histories. Using the cluster formation history information that is available in IllustrisTNG, we classify clusters as dynamically relaxed or unrelaxed based on their structural properties and compare the mean mass accretion histories of the resulting groups.

We establish in this work that the stellar mass asymmetry and magnitude gaps of galaxy clusters are readily observable structural parameters that most effectively predict the mass accretion histories of halos. By comparing the gravitational lensing profiles of dynamically relaxed and unrelaxed clusters classified using different structural parameters, we demonstrate that the stellar mass asymmetry most reliably distinguishes between halos in different dynamical states with different density profiles. We also show that line of sight galaxy projection does not significantly affect IllustrisTNG cluster samples and that differences between 3D-identified clusters and optically selected clusters can be accounted for with accurate cluster mass estimates. However, we find that the density profiles traced by the weak gravitational lensing around relaxed and unrelaxed clusters in IllustrisTNG simulations and DLIS x UNIONS observations are discrepant. The structural differences between the simulated and observed galaxy clusters will be further explored in future work to better relate this work's findings to real astrophysical systems.

Overall, we find through cosmological simulations that the structural properties of galaxy clusters can be used to effectively trace their mass accretion histories. The findings of this thesis establish which observable properties of clusters can be targeted in both observations and simulations to grant us insight into the formation histories of the largest structures in the universe.

Acknowledgements

I would like to thank my supervisor, Dr James Taylor, for his guidance throughout my degree. I would also like to thank the members of my advisory committee, Mike Hudson and Niayesh Afshordi, for their comments and suggestions. All of the other members of the Waterloo Centre for Astrophysics deserve thanks for their community and contributions to my development.

Lastly, I would like to thank my family for their continuous encouragement and support over the course of my career.

Dedication

To all of those who helped carry me to this stage of my life and career.

Table of Contents

Author's Declaration ii

Abstract iii

Acknowledgements v

Dedication vi

List of Figures x

List of Tables xvi

List of Abbreviations xvii

1 Introduction 1

1.1 The Concordance Cosmological Model 1

1.1.1 Friedmann Equation and Cosmic Expansion 1

1.1.2 The Hot Big Bang and Inflation 2

1.1.3 Cosmological Parameters 3

1.1.4 Dark Matter 4

1.2 Hierarchical Structure Formation 5

1.2.1 Linear and Non-linear Growth Theory 6

1.2.2 Mergers and Dynamical Relaxation . . . 6
1.2.3 Cosmological Dependence of Structure Formation . . . 7
1.3 Galaxy Clusters . . . 10
1.3.1 Cluster Identification . . . 10
1.3.2 The NFW Profile . . . 11
1.4 Hydrodynamical Simulations . . . 12
1.4.1 Effects of Baryons on Clusters . . . 13
1.4.2 Modelling Feedback . . . 14
1.5 Motivation . . . 15
1.6 Outline of the Thesis . . . 18

2 Method **19**
2.1 IllustrisTNG . . . 19
2.2 Simulation Volume Cuts . . . 20
2.3 Structural Measurements . . . 23
2.3.1 Centre of Mass Offset . . . 23
2.3.2 Axis Ratio . . . 25
2.3.3 Concentration . . . 29
2.3.4 Asymmetry . . . 30
2.3.5 Magnitude Gap . . . 31
2.4 Velocity-Depth Cluster Identification . . . 33
2.5 Mass Accretion History . . . 35
2.6 Lensing Profiles . . . 37

3 Structure and Growth History **41**
3.1 Centre of Mass Offset . . . 41
3.2 Axis Ratio . . . 56
3.3 Concentration . . . 65
3.4 Asymmetry . . . 68
3.5 Magnitude Gap . . . 73

4 Radial Structure and Optical Selection **79**
4.1 Dynamical Splits . . . 79
4.1.1 Centre of Mass Offset & Galaxy Offset . . . 80
4.1.2 Total Mass Asymmetry & Stellar Mass Asymmetry . . . 82
4.1.3 Magnitude Gap . . . 85
4.1.4 Comparison and Summary . . . 90
4.2 Projection Effects . . . 92
4.3 Cluster Selection . . . 97
4.4 DLIS x UNIONS Collaboration . . . 108

5 Conclusion **114**
5.1 Summary and Discussion . . . 114
5.2 Future Work . . . 118

References **120**

List of Figures

1.1 Contours of constant age and abundance of galaxy clusters with virialized mass $M_{\rm vir} = 5 \times 10^{14}\, M_\odot/h$ at redshift $z = 0.3$. 9

1.2 Constraints on the cosmological parameters σ_8 and Ω_m both from low-redshift structure and from the CMB. 17

2.1 The total surface mass density Σ of a massive halo and its most massive subhalos at redshift $z = 0$ in the TNG300-1 simulation. 21

2.2 The surface mass density Σ of the most massive halo at redshift $z = 0$ in the TNG300-1 simulation. 22

2.3 The surface mass densities Σ of two massive halos at redshift $z = 0$, as defined via a friends-of-friends (FoF) algorithm by the TNG300-1 simulation. 24

2.4 The surface mass density Σ and principal axes of a massive projected halo at redshift $z = 0$ in the TNG300-1 simulation. 25

2.5 The surface mass density Σ and principal axes of a massive halo at redshift $z = 0$ in the TNG300-1 simulation. 28

2.6 The surface mass density Σ around a massive halo at redshift $z = 0$ in the TNG300-1 simulation, sorted into evenly spaced angular and radial bins. . 31

2.7 The stellar surface mass density Σ of a massive halo and its most massive subhalos at redshift $z = 0$ in the TNG300-1 simulation. 34

2.8 The spatial distribution of subhalos with non-zero stellar mass around the brightest galaxy of the 100th most massive cluster at redshift $z = 0$ in the TNG300-1 simulation. 36

2.9 The gravitational lensing profiles $\Delta\Sigma$ computed with different innermost radial bins for clusters with mass $M_{500c} \geq 1 \times 10^{14}\, M_\odot$ at redshift $z = 0$ in the TNG300-1 simulation. 39

3.1 The 3D centre of mass offsets plotted against the z_{75} mass history for halos with masses $1 \times 10^{13} < M_{200c}/M_{\odot} < 5 \times 10^{13}$ at redshift $z = 0$ in the TNG300-1 simulation. 42

3.2 The 3D centre of mass offsets plotted against the z_{75} mass history for halos with masses $1 \times 10^{13} < M_{200c}/M_{\odot} < 5 \times 10^{13}$ at redshift $z = 0$ in the TNG300-1 simulation. The left panel is a heat map of the distribution with a Gaussian smoothing applied. The right panel splits the distribution into groups using a 2-component Gaussian mixture model. 43

3.3 The median mass evolution histories within R_{200c} of relaxed and unrelaxed $1 \times 10^{13} < M_{200c}/M_{\odot} < 5 \times 10^{13}$ halos at redshift $z = 0$ in the TNG300-1 simulation. 45

3.4 Halos with masses $1 \times 10^{13} < M_{200c}/M_{\odot} < 5 \times 10^{13}$ at redshift $z = 0$ in the TNG300-1 simulation are split into groups using Gaussian mixture models with varying numbers of components. 46

3.5 The BIC and AIC for Gaussian mixture models fit to the 3D centre of mass offset and z_{75} mass history distribution, plotted against the number of model components. 48

3.6 The 3D centre of mass offsets and median mass accretion histories for halos with masses $1 \times 10^{13} < M_{200c}/M_{\odot} < 5 \times 10^{13}$ at redshift $z = 0$ in the TNG300-1 simulation. 49

3.7 The z-axis projected 2D centre of mass offsets and median mass accretion histories for halos with masses $1 \times 10^{13} < M_{200c}/M_{\odot} < 5 \times 10^{13}$ at redshift $z = 0$ in the TNG300-1 simulation. 50

3.8 The left panel shows the χ^2 difference between the median mass accretion histories of the relaxed and unrelaxed groups as a function of the split in z-axis projected centre of mass offsets for halos with masses $1 \times 10^{13} < M_{200c}/M_{\odot} < 5 \times 10^{13}$ at redshift $z = 0$ in the TNG300-1 simulation. The right panel shows the median mass accretion histories at the optimal split of $\log_{10}(\text{Offset Split}/R_{200c}) = -1.07$, which maximises χ^2. 52

3.9 The z-axis projected galaxy offsets plotted against the z_{75} mass history for halos with masses $1 \times 10^{13} < M_{200c}/M_{\odot} < 5 \times 10^{13}$ at redshift $z = 0$ in the TNG300-1 simulation. 54

3.10 The z-axis projected galaxy offsets and median mass accretion histories for halos with masses $1 \times 10^{13} < M_{200c}/M_{\odot} < 5 \times 10^{13}$ at redshift $z = 0$ in the TNG300-1 simulation. The left panel splits the distribution into groups using a 2-component, 2D Gaussian mixture model with the z_{75} mass history. 55

3.11 The z-axis projected galaxy offsets and median mass accretion histories for halos with masses $1 \times 10^{13} < M_{200c}/M_{\odot} < 5 \times 10^{13}$ at redshift $z = 0$ in the TNG300-1 simulation. The top left panel is the distribution of offsets fit with a 2-component, 1D Gaussian mixture model. The bottom left panel shows the χ^2 difference between the median z_{75} of the relaxed and unrelaxed groups as a function of the split in galaxy offset. 57

3.12 The z-axis projected galaxy offsets and median mass accretion histories for halos with masses $1 \times 10^{13} < M_{200c}/M_{\odot} < 5 \times 10^{13}$ at redshift $z = 0$ in the TNG300-1 simulation. The top left panel is the full distribution of projected galaxy offsets, and the top right panel splits the top and bottom 20% of halos into relaxed and unrelaxed groups based on this distribution. 58

3.13 The major-to-minor axis ratios $s = c/a$ plotted against the z_{75} mass history for halos with masses $1 \times 10^{13} < M_{200c}/M_{\odot} < 5 \times 10^{13}$ at redshift $z = 0$ in the TNG300-1 simulation. 60

3.14 The distribution of major-to-minor axis ratios $s = c/a$, z_{75} mass histories, and centre of mass offsets for halos with masses $1 \times 10^{13} < M_{200c}/M_{\odot} < 5 \times 10^{13}$ at redshift $z = 0$ in the TNG300-1 simulation. 61

3.15 The distribution of centre of mass offsets and axis ratios within R_{200c}, both in 3D and projected along the z-axis, for halos with masses $1 \times 10^{13} < M_{200c}/M_{\odot} < 5 \times 10^{13}$ at redshift $z = 0$ in the TNG300-1 simulation. 63

3.16 The projected galaxy axis ratio plotted against the z_{75} mass history for halos with masses $1 \times 10^{13} < M_{200c}/M_{\odot} < 5 \times 10^{13}$ at redshift $z = 0$ in the TNG300-1 simulation. 64

3.17 The NFW concentration plotted against the z_{75} mass history for halos with masses $1 \times 10^{13} < M_{200c}/M_{\odot} < 5 \times 10^{13}$ at redshift $z = 0$ in the TNG300-1 simulation. 66

3.18 The distribution of NFW concentrations, z_{75} mass histories, and centre of mass offsets for halos with masses $1 \times 10^{13} < M_{200c}/M_{\odot} < 5 \times 10^{13}$ at redshift $z = 0$ in the TNG300-1 simulation. 67

3.19 Halo asymmetry plotted against the z_{75} mass history for halos with masses $1 \times 10^{13} < M_{200c}/M_{\odot} < 5 \times 10^{13}$ at redshift $z = 0$ in the TNG300-1 simulation. 69

3.20 The asymmetry, projected centre of mass offset, and z_{75} mass history for halos with masses $1 \times 10^{13} < M_{200c}/M_{\odot} < 5 \times 10^{13}$ at redshift $z = 0$ in the TNG300-1 simulation. 70

3.21 The asymmetry and median mass accretion histories for halos with masses $M_{200c} > 5 \times 10^{13}\, M_{\odot}$ at redshift $z = 0$ in the TNG300-1 simulation. 72

3.22 The stellar mass asymmetry and median mass accretion histories for halos with masses $M_{200c} > 5 \times 10^{13}\, M_{\odot}$ at redshift $z = 0$ in the TNG300-1 simulation. 74

3.23 The magnitude and mass gaps of galaxies within R_{500c} for halos with masses $M_{500c} \geq 5 \times 10^{13}\, M_{\odot}$ at redshift $z = 0$ in the TNG300-1 simulation. 76

3.24 A colour-magnitude diagram for galaxies with stellar masses $M^* \geq 1 \times 10^{10}\, M_{\odot}$ at redshift $z = 0$ in the TNG300-1 simulation. 77

3.25 The median mass accretion histories for the relaxed and unrelaxed halos split by magnitude gaps in Figure 3.23. 78

4.1 The z-axis projected centre of mass offsets and mean lensing profiles for halos with masses $M_{500c} \geq 1 \times 10^{14}\, M_{\odot}$ at redshift $z = 0$ in the TNG300-1 simulation. 81

4.2 The z-axis projected galaxy offsets and mean lensing profiles for halos with masses $M_{500c} \geq 1 \times 10^{14}\, M_{\odot}$ at redshift $z = 0$ in the TNG300-1 simulation. 83

4.3 The asymmetries and mean lensing profiles of halos with masses $M_{500c} \geq 1 \times 10^{14}\, M_{\odot}$ at redshift $z = 0$ in the TNG300-1 simulation. 84

4.4 The stellar mass asymmetry and mean lensing profiles for halos with masses $M_{500c} \geq 1 \times 10^{14}\, M_{\odot}$ at redshift $z = 0$ in the TNG300-1 simulation. 86

4.5 The magnitude and mass gaps of galaxies within R_{500c} for halos with masses $M_{500c} \geq 1 \times 10^{14}\, M_{\odot}$ at redshift $z = 0$ in the TNG300-1 simulation. 88

4.6 The mean lensing profiles $\Delta\Sigma$ for the relaxed and unrelaxed halos are classified based on magnitude and mass gaps in the TNG300-1 simulation. . . 89

4.7 The mean lensing profiles $\Delta\Sigma$ for relaxed and unrelaxed halos with mass $M_{500c} \geq 5 \times 10^{13}\, M_{\odot}$ at redshift $z = 0.4$, classified based on asymmetry in the TNG300-1 simulation. 91

4.8 The mean fraction of the stellar mass in clusters as a function of member galaxy stellar mass M^* in the TNG300-1 simulation. 93

4.9 The mean fraction of the stellar mass in clusters as a function of galaxy stellar mass M_* relative to the total stellar mass of galaxies in the parent cluster $M_{*,\mathrm{tot}}$ in the TNG300-1 simulation. 95

4.10 The mean lensing profiles $\Delta\Sigma$ for the relaxed and unrelaxed halos, classified based on the magnitude gaps of 3D and projected member galaxies in the TNG300-1 simulation. 96

4.11 The z- and K-band magnitudes of galaxies as a function of stellar mass within a 30 kpc aperture in the TNG300-1 simulation. 98

4.12 The projected spatial distribution of massive galaxies and optically identified clusters in the TNG300-1 simulation. 100

4.13 The cumulative distribution function of the fraction of stellar mass in optically selected clusters that is a part of the true 3D clusters to which they correspond in the TNG300-1 simulation. 101

4.14 The mean fraction of stellar mass in optically selected clusters that is part of the true 3D clusters to which they correspond, as a function of line of sight depth around the BCG in the TNG300-1 simulation. 102

4.15 The number of optically selected clusters with estimated masses $M_{500} \geq 1 \times 10^{14}\,M_\odot$ as a function of line of sight depth around the BCG in the TNG300-1 simulation. 103

4.16 The mean gravitational lensing profiles $\Delta\Sigma$ for 3D identified clusters and optically identified clusters at redshifts $z = 0.0$ and $z = 0.4$ in the TNG300-1 simulation. These clusters have masses $M_{500c} \geq 1 \times 10^{14}\,M_\odot$. 104

4.17 The mean lensing profiles $\Delta\Sigma$ for 3D identified clusters and optically identified clusters at redshifts $z = 0.0$ and $z = 0.4$ in the TNG300-1 simulation. The real clusters' minimum mass was chosen so as to fit the W&H lensing profiles. 106

4.18 The mean lensing profiles $\Delta\Sigma$ for 3D identified clusters and optically identified clusters at redshift $z = 0.4$, split into dynamically relaxed and unrelaxed groups in the TNG300-1 simulation. 107

4.19 The magnitude and mass gaps of galaxies within R_{500} for clusters in the DLIS catalogue, split into relaxed and unrelaxed groups. 109

4.20 The distributions of stellar masses and redshifts of clusters in the DLIS catalogue, split into relaxed and unrelaxed groups. 110

4.21 The lensing profiles $\Delta\Sigma$ of stacked clusters in the DLIS catalogue, split into relaxed and unrelaxed groups. 111

4.22 The lensing profiles $\Delta\Sigma$ for dynamically relaxed and unrelaxed clusters in the TNG300-1 simulation are compared to those from the DLIS catalogue. 113

List of Tables

4.1 The mean masses and uncertainties of relaxed and unrelaxed halo samples are classified based on magnitude and mass gaps. 89

4.2 The mean masses and uncertainties of relaxed and unrelaxed halo samples classified based on asymmetry. 90

List of Abbreviations

AGN active galactic nuclei 13, 14, 19

AIC Akaike information criterion 47, 48

BCG brightest cluster galaxy 20, 23, 24, 30–33, 35, 36, 39, 41, 51, 53, 62, 64, 68–74, 80, 82, 83, 85, 87, 92–94, 97–99, 101–104, 108, 110

BIC Bayesian information criterion 47, 48

CMB cosmic microwave background 3–5, 8, 11, 15–17

DESI Dark Energy Spectroscopic Instrument 79

DLIS DESI Legacy Imaging Survey 79, 97, 99, 108–113, 116–119

FLRW Friedmann–Lemaître–Robertson–Walker 1, 2

FoF friends-of-friends x, 20–25, 27–29, 31, 34, 35, 37, 70, 92, 99, 103, 104, 106, 107, 113

MHD magnetohydrodynamical 19, 75, 119

NFW Navarro-Frenk-White 11, 29, 65–67, 73

SZ Sunyaev–Zel'dovich 11

UNIONS Ultraviolet Near Infrared Optical Northern Survey 79, 97, 108, 111–113, 116–118

Chapter 1

Introduction

1.1 The Concordance Cosmological Model

The concordance cosmological model, often referred to as ΛCDM, is the most widely accepted description of the large-scale structure and evolution of the universe. This model assumes a Friedmann–Lemaître–Robertson–Walker metric of spacetime (Abdalla et al., 2022; Koussour et al., 2024), a Hot Big Bang (Ostriker & Steinhardt, 1995; Mo et al., 2010), cosmic inflation from nearly scale-invariant fluctuations in the matter density field (Guth, 1981; Frenk & White, 2012; Bullock & Boylan-Kolchin, 2017; Abdalla et al., 2022), and a spatially flat universe with dark energy, radiation, and matter comprised of Standard Model particles and cold dark matter (Ostriker & Steinhardt, 1995; Spergel et al., 2007).

1.1.1 Friedmann Equation and Cosmic Expansion

The Friedmann–Lemaître–Robertson–Walker (FLRW) metric is a description of the geometry of spacetime under Einstein's theory of general relativity (Ryden, 2016; Koussour et al., 2024). This metric describes the universe as homogenous and isotropic, thus obeying the cosmological principle. The ΛCDM cosmological model also describes the universe as expanding. From the FLRW metric, Einstein's field equations were solved by Alexander Friedmann to produce the Friedmann equations (Ryden, 2016; Koussour et al., 2024). In the context of ΛCDM cosmology, the first Friedmann equation is typically expressed as:

$$H^2 = \left(\frac{\dot{a}}{a}\right)^2 = \frac{8\pi G}{3}\rho - \frac{kc^2}{a^2} + \frac{\Lambda c^2}{3}\,, \tag{1.1}$$

where H is the Hubble parameter which describes the expansion rate, a is the scale factor, G is the gravitational constant, ρ is the energy density of matter and radiation, k is the spatial curvature of the universe, c is the speed of light, and Λ is the cosmological constant (Ryden, 2016). The scale factor a describes the scale of the universe relative to the present day, such that $a_0 = a(t_0) = 1$ where t_0 is the current age of the universe. Given this definition, we see that the Friedmann equation describes the expansion rate of the universe. In an expanding universe, distances may be represented in comoving coordinates so as to scale with the expansion. A comoving distance is defined as $\chi = d(t)/a(t)$, where $d(t)$ is the proper distance between two points and $a(t)$ is the scale factor. In this work, comoving megaparsecs and kiloparsecs are denoted as cMpc and ckpc, respectively. Besides the matter density and curvature, a key ingredient in Equation 1.1 that drives the expansion of the universe is the cosmological constant Λ, which parametrises dark energy. With properly tuned values of curvature, matter and radiation density, and dark energy, the FLRW metric and its assumptions of homogeneity and anisotropy have successfully described large-scale observations of the universe (Räsänen et al., 2015). This has cemented the cosmological parameter Λ as part of the concordance cosmological model.

Due to the expansion of space under the FLRW scheme, the wavelength of any emitted light λ_e at time t_e is stretched such that an observer at time t_0 observes a wavelength λ_0 as given by:

$$\frac{\lambda_0}{\lambda_e} = \frac{a(t_0)}{a(t_e)}\,, \tag{1.2}$$

as derived in, e.g., Mo et al. (2010); Ryden (2016). The cosmological redshift z is defined as the fractional increase in the wavelength of light emitted from some source:

$$z = \frac{\lambda_0 - \lambda_e}{\lambda_e} = \frac{a(t_0)}{a(t_e)} - 1\,. \tag{1.3}$$

The redshift z of light is thus a direct measurement of the expansion of the universe since the time that the light was emitted (Mo et al., 2010; Ryden, 2016). Given a model for the evolution of the scale factor from Equation 1.1, the redshift of a source yields the age of the universe at the time the light was emitted.

1.1.2 The Hot Big Bang and Inflation

The FLRW metric and resultant Friedmann equations, along with the expansion of the universe first observed by Hubble, imply that the universe was previously in a hot, dense state. This is the foundation for the Hot Big Bang model. The concordance cosmology

is a configuration of the Hot Big Bang model, which includes a period of inflation in the early universe (Ostriker & Steinhardt, 1995). These concepts are important to the ΛCDM cosmology since they describe the origin of structure formation and account for some key observables, such as features in the power spectrum of the cosmic microwave background (CMB) (Ryden, 2016). The inflation model proposes that prior to the Hot Big Bang, the universe experienced a period of rapid expansion. This expansion explains multiple observables, such as the homogeneity and flatness of the universe (Guth, 1981; Spergel et al., 2007; Ryden, 2016). Given a period of inflation, regions of the universe which otherwise do not appear to be in causal contact would indeed have interacted in the early universe. This justifies the uniformity of the CMB and the low fluctuations observed in it (Guth, 1981; Ryden, 2016). Inflation would also have pushed the scale of any spatial curvature beyond our horizon, explaining the near-zero curvature of the observable universe (Guth, 1981; Ryden, 2016). Perhaps most notably to ΛCDM, the Hot Big Bang and inflation models explain the origin of the initial conditions of the structure growth in the universe (Turner, 1999). Quantum fluctuations in the primordial universe prior to inflation are thought to have been frozen in as seed perturbations for the resultant growth of galaxies, clusters and large-scale structure as described in Section 1.2. These initial conditions, along with the existence of cold dark matter, enable us to reconstruct not only the structure seen in the present universe but also in the power spectrum of the CMB.

1.1.3 Cosmological Parameters

Concordance cosmology proposes that the energy density Ω_0 of the universe includes several components, namely, spatial curvature Ω_K, matter Ω_m, radiation Ω_r, and dark energy Ω_Λ (Condon & Matthews, 2018; Planck Collaboration et al., 2020). More precisely, the energy densities Ω_i of the components i are given by:

$$\Omega_i = \frac{\rho_i}{\rho_{\text{crit}}}\,, \tag{1.4}$$

where ρ_i is the physical energy density of the component and ρ_{crit} is the critical density of the universe (Mo et al., 2010; Ryden, 2016; Condon & Matthews, 2018). The critical density is the energy density of matter and radiation required to halt the expansion of the universe. It can be derived from Equation 1.1 and is given in, e.g., Mo et al. (2010); Ryden (2016) as:

$$\rho_{\text{crit}} = \frac{3H^2}{8\pi G}\,. \tag{1.5}$$

The relative energy densities are related such that $\Omega_K = 1 - (\Omega_m + \Omega_r + \Omega_\Lambda)$. Constraints from observations of the CMB are consistent with a flat universe where $\Omega_K = 0$, and thus the total energy density of the universe is $\Omega_0 = \Omega_m + \Omega_r + \Omega_\Lambda = 1$.

The radiation component of the universe's energy density is comprised of photons and neutrinos. At the present day, the best fit values of Ω_r are of order 10^{-5} (Planck Collaboration et al., 2020). The matter density is made up of two distinct components: Standard Model particles, which are often referred to broadly as baryons in the context of cosmology, and dark matter. Dark matter interacts gravitationally with baryons and negligibly through other channels. The concordance cosmology assumes the dominance of cold dark matter (CDM) (Blumenthal et al., 1984). In this context, dark matter being cold means that it is non-relativistic at the time that it thermally decouples from the other components of the early universe (Ryden, 2016). In other words, dark matter is moving at far less than the speed of light, and thus its kinetic energy is negligible compared to its rest mass energy. The temperature, or alternatively kinetic energy, of dark matter determines how readily it clumps under the influence of gravity and thus how structures grow as the universe ages. Hot dark matter is able to free-stream over large distances due to its greater kinetic energy, which would cause the small-scale fluctuations visible in the matter spectrum to be washed out (Blumenthal et al., 1984). As a result, CDM is necessary for the concordance cosmology.

In addition to the energy densities of the different components of the universe, there are a few other cosmological parameters that are used to specify the concordance cosmology. A notable parameter relevant to this work is the amplitude of matter density fluctuations, σ_8. This parameter is defined as the root mean square of the density fluctuations relative to the mean density of the universe at the present day within $8\,\mathrm{Mpc}/h$ spheres, where $h = H_0/\left(100\ \mathrm{km\ s^{-1}Mpc^{-1}}\right)$ is the dimensionless Hubble parameter (Amoura et al., 2021). A greater value of σ_8 implies greater fluctuations in the matter field, which produce more bound structures in the low-redshift universe, such as galaxies and galaxy clusters (Amoura et al., 2021).

1.1.4 Dark Matter

Due to apparent discrepancies between our understanding of gravitation through general relativity and the behaviour of some astronomical objects, dark matter has been posited to account for gravitational phenomena that are not well described by the Standard Model (Bertone et al., 2005). Evidence for the existence of dark matter extends across many cosmological scales. On the galactic scale, the rotation curves of galaxies point to unobserved mass in extended halos around galaxies. The rotational velocity of gas in the

outer regions of galaxies is expected to drop off with radius since the gravitational force further from the dense regions of the galaxy should be weaker. However, we see that the rotation curves flatten out at large radii, as observed through 21-cm emission from neutral hydrogen gas and optical surface photometry. This points to a halo of unobserved mass around galaxies (Bertone et al., 2005; Arbey & Mahmoudi, 2021). Other evidence of unseen mass on the galactic scale includes strong gravitational lensing around massive galaxies, weak lensing of galaxies, velocities of dwarf galaxies, and more (Bertone et al., 2005). On the scale of galaxy clusters, the large velocity dispersion of galaxies within the clusters provides more evidence for the existence of dark matter, as does the discrepancy between the actual temperature of cluster gas and the expected temperature in hydrostatic equilibrium with the observed mass of baryons (Bertone et al., 2005). The strong gravitational lensing of distant galaxies around galaxy clusters also provides evidence of mass that is separated from the gas in clusters observed via X-ray emission (Arbey & Mahmoudi, 2021). On cosmological scales, temperature fluctuations in the CMB can be mapped to large-scale density fluctuations. The inferred evolution of these fluctuations is consistent with dark matter making up approximately 85% of the matter in the universe (Bertone et al., 2005; Arbey & Mahmoudi, 2021). Due to dark matter only interacting significantly through gravity, its imprint on the power spectrum of the CMB is very distinct from that of baryons, which produce oscillations due to acoustic feedback and direct interaction with photons. Potential particle candidates for dark matter outside of the Standard Model are numerous, and their masses span many orders of magnitude (Bertone et al., 2005). Despite this uncertainty in what constitutes dark matter, its distribution through the universe can be mapped using its gravitational influence.

1.2 Hierarchical Structure Formation

Hierarchical structure formation is the "bottom-up" way in which gravitationally bound structures in the universe form. That is to say, small objects form first and then gradually merge together into larger structures (Voit, 2005; Mo et al., 2010). The initial seeds of structure in the early universe are small fluctuations in the matter density field. Such fluctuations are visible in the CMB, and their amplitude relative to the mean density of the universe is parametrised by the cosmological parameter σ_8. Overdensities in these fluctuations gradually collapse into small, gravitationally bound structures. This occurs primarily under the influence of cold dark matter (CDM), given that it makes up the majority of the universe's mass (Turner, 1999; Voit, 2005). The baryonic gas that falls into these dark matter halos governs the formation of early populations of stars and protogalaxies, which

then merge into larger galaxies and groups. This hierarchical collapse eventually forms the largest gravitationally bound structures in the universe, galaxy clusters. Hierarchical formation is also responsible for the large-scale structure in which groups and clusters of galaxies are imbedded, namely the filaments and voids that make up the cosmic web (Turner, 1999; Voit, 2005).

1.2.1 Linear and Non-linear Growth Theory

The growth of small fluctuations in the matter field governed by gravity is described by linear growth theory. The linear growth equation, which models the evolution of density contrasts $\delta = (\rho - \bar{\rho})/\bar{\rho}$ relative to a background density $\bar{\rho}$, is given as follows:

$$\ddot{\delta} + 2H\dot{\delta} = 4\pi G\bar{\rho}\delta\,, \tag{1.6}$$

where H is the Hubble parameter and G is the gravitational constant (Huterer, 2023). This is the pressureless form of the linear growth equation, which is valid for dark matter and for baryonic matter on scales larger than the Jeans length, where pressure support can be neglected. In general, given the expansion of the universe encapsulated by H and the matter density given by $\bar{\rho}$, we can solve for the growth of perturbations numerically. However, Equation 1.6 is only valid in the limit that the density fluctuations are small, $\delta \ll 1$. Once perturbations grow to be larger such that $\delta \gtrsim 1$, linear growth theory breaks down, and over-dense regions form gravitationally bound structures that interact and merge. For this regime of structure growth, numerical simulations are generally required to solve for the complex behaviour (Angulo & Hahn, 2022).

1.2.2 Mergers and Dynamical Relaxation

When large, gravitationally bound structures such as groups and clusters of galaxies merge together, they are initially in a complex dynamical state. Unrelaxed dynamical states are generally characterised by irregular mass distributions, large bulk velocities of recently merged material, and shocks in cluster gas (Zhang et al., 2022; Kelkar et al., 2023). Over time, the merged system relaxes dynamically until it reaches a stable state. Several processes contribute to a halo's relaxation, including violent relaxation, dynamical friction, and tidal stripping. Violent relaxation refers to how the orbits of objects within a cluster become perturbed due to the rapid changing of the gravitational potential within the cluster during a merger (Lynden-Bell, 1967). This randomisation of orbits redistributes the energy of objects in a cluster, allowing the cluster to reach a new stable state. Dynamical

friction is a process which causes the orbits of objects such as infalling galaxies to decay within a cluster (Adhikari et al., 2016). As dense structures like galaxies move through the less dense intra-cluster medium, they attract background matter and create a wake of particles following their motion. This wake pulls on the galaxy gravitationally, causing it to lose orbital energy and relax into the centre of the cluster's gravitational potential. Lastly, tidal stripping pulls loosely bound particles in subhalos or galaxies away from these structures due to the gradient in the strong gravitational field of the cluster (Merritt, 1983; Mo et al., 2010). This process redistributes the mass in a cluster, smoothing out the gravitational potential. All of these processes and others act over time to relax the dynamical states of recently merged systems.

1.2.3 Cosmological Dependence of Structure Formation

Given that the gravitational collapse of structure is hierarchical, the largest structures in the universe formed most recently. As a result, galaxy clusters are relatively recent developments in the history of the universe, and many of them are in complex dynamical states as they undergo mergers. Due to their recent formation, the number density, mass distribution and ages of galaxy clusters in the nearby universe are sensitive to cosmological parameters that determine structure growth (Gilbank et al., 2004; Amoura et al., 2021). In particular, the population of galaxy clusters is influenced by the matter density Ω_m and the amplitude of mass density fluctuations σ_8. As a result of hierarchical structure formation, the abundance and evolution of clusters provide insight into key parameters of the concordance cosmological model.

As is given in Section 1.1.3, the amplitude of mass density fluctuations σ_8 is defined as the root mean square of the density fluctuations in the universe at the present day within $8\,\mathrm{Mpc}/h$ spheres (Amoura et al., 2021). Greater fluctuations in the early matter density field of the universe grow into larger fluctuations and bound structures over time. This results in a more clustered distribution of matter at the present day and thus a greater value of σ_8. The matter density Ω_m describes the total amount of matter in the universe and thus also determines the number and size of gravitationally bound structures that can have developed from the early fluctuations to the present day. Due to these relationships of σ_8 and Ω_m with structure formation, measurements of the abundance of large structures in the low-redshift universe have been used to constrain the values of these cosmological parameters (Joudaki et al., 2018; Abdalla et al., 2022; Wright et al., 2025). Such constraints are often expressed in terms of the parameter $S_8 = \sigma_8\sqrt{\Omega_m/0.3}$, which is defined so as to capture the degenerate effects of both σ_8 and Ω_m on structure formation. A common way to produce constraints on these parameters is to simply count the number of massive

galaxy clusters in the universe from large surveys. Given a survey with well-understood completeness and contamination, cluster counts can offer useful measurements of structure formation. Another common way of measuring structure is through weak gravitational lensing, which is further discussed in Section 2.6. In brief, the distortion of light around massive structures such as galaxies and clusters, or around large-scale structure in the case of cosmic shear, traces the density profile along the line of sight from the light source. Such light distortions enable the measurement of the mass structure between the source and observer. These and other low-redshift measurements of structure produce similar constraints on both σ_8 and Ω_m (Abdalla et al., 2022).

While both σ_8 and Ω_m influence the amount of structure in the late universe, they differ in how they influence the formation of that structure. Given the hierarchical growth of structure in the universe, the amplitude of density fluctuations best traces the size of fluctuations in the early universe, while the matter density best traces how significantly those fluctuations grow. Thus, greater values of σ_8 correspond to older structures, while greater values of Ω_m correspond to more recently formed structures (Amoura et al., 2021). An understanding of the assembly times of halos can thus provide a unique probe of both σ_8 and Ω_m, granting valuable cosmological insight.

Recent work has probed how the structure of halos may reflect the assembly time of clusters (Wong & Taylor, 2012; Amoura et al., 2021). Amoura et al. (2021) made use of theoretical predictions of halo assembly to explore how halo mass accretion history varies as a function of cosmological parameters. They also used numerical simulations to investigate the relationship between halo structures and their formation histories. Amoura et al. (2021) demonstrated that high matter density fluctuations σ_8 and a low matter density parameter Ω_m do indeed produce early structure formation, whereas low σ_8 and high Ω_m produce more recent structure formation. Figure 1.1 from Amoura et al. (2021) shows the constraints achieved for these two cosmological parameters from cluster counts and mean cluster age measurements at a particular halo mass and redshift. We see from the background colour contours in the figure that the abundance of structures in the universe is influenced similarly by both σ_8 and Ω_m, with a clear degeneracy between the parameters. The dashed lines confirm that the median cluster age is greater for high σ_8 and low Ω_m, and lower for low σ_8 and high Ω_m. We note that the abundance and age contours are nearly perpendicular around the best-fit values from CMB measurements by Planck Collaboration et al. (2020), indicating that these two properties of large structures can be used to constrain the cosmological parameters in a very complementary way.

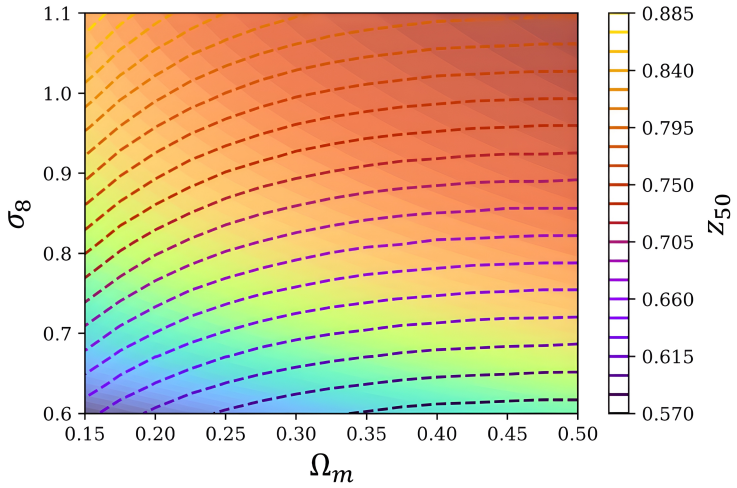


Figure 1.1: Contours of constant age and abundance of galaxy clusters with virialized mass $M_{\rm vir} = 5 \times 10^{14}\, M_\odot/h$ at redshift $z = 0.3$. The solid coloured contours are logarithmically spaced curves of constant cluster number density per unit $\log_{10}(M_{\rm vir})$. The dashed lines are curves of constant median formation time z_{50}, as defined in Section 2.5. Cluster abundances and formation times were computed analytically, assuming the ellipsoidal collapse of halos. Modified from Amoura et al. (2021).

1.3 Galaxy Clusters

Galaxy clusters are the largest and most massive gravitationally bound structures in the universe. Clusters are primarily bound by the gravity of their dark matter halos, as the velocity dispersions of their member galaxies greatly exceed what could be bound by the mass of the observed baryonic matter (Kravtsov & Borgani, 2012). Between the galaxies in a cluster, there is an intracluster medium of ionised gas. This plasma constitutes the majority of the baryonic mass in clusters (Kravtsov & Borgani, 2012).

1.3.1 Cluster Identification

Galaxy clusters can be identified in a variety of ways. A common and straightforward way of identifying galaxy clusters is by simply recognising overdensities of galaxies in optical or infrared surveys (Gilbank et al., 2004). The disadvantage of this approach is that an observed overdensity of galaxies could be due to the projection of galaxies at significantly different distances along the line of sight rather than due to genuine clustering. To mitigate the effects of projection, distance estimates to galaxies can be obtained in a variety of ways. Distances are most commonly estimated in large surveys using redshift measurements of the emission from galaxies (Gilbank et al., 2004; Aliş, 2024). Spectroscopic measurements determine the redshift of galaxies directly from their emission spectra, which provide reliable measurements of their recession velocities. These measurements allow us to infer distances to galaxies due to the expansion of the universe and thus identify clustering along the line of sight. Given that spectroscopic redshifts require measurements of individual galactic spectra, photometric redshifts are more commonly used (Aliş, 2024). Photometric redshifts rely on inferring the redshifts of galaxies based on how their observed magnitudes in different photometric bands compare to their predicted colours using template model fitting. Photometric redshifts have much greater uncertainties than spectroscopic redshifts, leading to poorer constraints on line of sight distances and clustering (Benítez, 2000). However, given the relative convenience of the measurement, photometric redshifts are used for cluster identification in many catalogues.

An alternative method for identifying clusters method is by measuring the X-ray emission from the intracluster medium (Gilbank et al., 2004). Due to the high masses of galaxy clusters, they have very deep gravitational potential wells compared to less massive groups of galaxies. The gas that forms the intracluster medium is heated through various mechanisms, including its infall into the deep gravitational well, mergers of other structures into the well of the cluster, and feedback from supermassive black holes. These processes heat

the gas so that it radiates X-rays through thermal bremsstrahlung (Rosati et al., 2002). A common way of identifying galaxy clusters is thus by searching for extended X-ray sources, which mark the presence of hot gas. In fact, galaxy clusters are often defined relative to less massive groups in terms of whether they have observable X-ray properties (Rosati et al., 2002). This highlights that X-ray detections have limited sensitivity and generally detect more massive clusters than optical surveys. Studying the luminosity of these X-ray emissions in the intracluster medium allows us to probe the depths of the gravitational potential throughout a cluster, granting insight into their structure and mass distributions (Rosati et al., 2002; Kravtsov & Borgani, 2012).

Another interesting way of identifying galaxy clusters is through the Sunyaev–Zel'dovich (SZ) effect (Sunyaev & Zeldovich, 1972; Rephaeli et al., 2006). The SZ effect occurs when low-energy photons from the CMB are scattered to higher energies by free electrons in hot, ionised gas via inverse Compton scattering. The intracluster medium upscatters low-energy CMB photons via this effect, resulting in higher-energy distortions and anisotropies in the observable CMB signal. Such distortions can be detected in SZ mapping surveys to identify the locations of galaxy clusters (Rephaeli et al., 2006). Similarly to X-ray detections, the SZ effect has limited sensitivity and generally detects more massive clusters than optical surveys. However, a benefit of this detection method is that the distortions in the CMB due to interactions with intracluster media are not strongly dependent on the redshifts of the clusters. As a result, the SZ effect enables us to identify clusters without the common surface brightness limitations of distant galaxies (Rephaeli et al., 2006).

1.3.2 The NFW Profile

The dark matter halos around galaxies and clusters dominate the mass of each system. As such, it is crucial to be able to model their structure in order to model galaxies and clusters more broadly. Navarro et al. (1996, 1997) conducted N-body simulations of halos and found that the radial density of dark matter halos is well fit by what is now called the Navarro-Frenk-White (NFW) profile. This profile is given by:

$$\rho(r) = \frac{\rho_0}{\frac{r}{r_s}\left(1 + \frac{r}{r_s}\right)^2},$$

where the characteristic density ρ_0 and scale radius r_s are parameters of the system (Navarro et al., 1996, 1997). The NFW profile identifies two distinct regions of the halo: an inner region in which the density drops off as $\rho \propto r^{-1}$, and an outer region in which $\rho \propto r^{-3}$. These two regions may reflect two phases in the formation of the halo, with

an initial rapid phase where the profile builds up more densely and a later slower phase where the outer region forms around the centre (Taylor, 2010). The boundary between the regions corresponds roughly to the scale radius r_s. The concentration c of the halo is defined in terms of the scale radius and virial radius r_{vir} of a halo, $c = r_{\text{vir}}/r_s$ (Navarro et al., 1997). The virial radius marks the region in which the mass reaches equilibrium under gravitational collapse. It is often used to define the boundaries of gravitationally collapsed or merged regions during structure formation. The virial radius of a halo roughly corresponds to the radius in which the mean density is 200 times the critical density of the universe (Navarro et al., 1997). We use this approximation of the virial radius throughout this work and denote it as R_{200c}. Similarly, the radius within which the mean density is 500 times the critical density is denoted R_{500c}.

1.4 Hydrodynamical Simulations

Cosmological simulations are numerical simulations that model the evolution of galaxies, groups and clusters. These simulations generally start with a nearly uniform matter distribution that mimics the early universe, from which anisotropies grow into large structures (Amoura, 2023). Simulations conducted to model individual galaxies or clusters are often zoom-in simulations, where a large volume is simulated to get the properties of the area surrounding a structure, then the galaxy or cluster is re-simulated with higher resolution (Schaye et al., 2015; Muratov et al., 2015).

Cosmological simulations can be divided into two broad categories: N-body simulations and hydrodynamical simulations (Amoura, 2023). N-body simulations involve a set of particles which represent some amount of matter under the influence of some force or forces. In the case of cosmological simulations, we generally use dark matter mass elements acting under the influence of mutual gravity (Amoura, 2023). By contrast, hydrodynamical simulations are capable of modelling more complex systems by solving the equations that govern fluids. These simulations are further divided into two common categories: Lagrangian particle-based simulations and Eulerian grid-based simulations (Shu, 1992; Amoura, 2023). Lagrangian particle-based simulations discretise the fluid into a set of sample particles, which are then smoothed and weighted over a space. Eulerian grid-based simulations divide a volume into a grid, then record and evolve the properties of each cell. Popular algorithms make use of adaptive grid sizes to grant higher resolution to regions with a greater density (Amoura, 2023). These methods are important in testing and calibrating our understanding of structure formation in conjunction with observational data.

1.4.1 Effects of Baryons on Clusters

Since dark matter dominates the mass of galaxy clusters, models and simulations of clusters often do not consider the effects of baryons on their structure and formation, or do so only in a simplified fashion. However, the effects of baryons are significant in altering the density profiles of halos, and so they should be better understood through simulation (Amoura et al., 2021). The density profile of a cluster can be modified by radiative cooling, star formation, and feedback from supernovae and active galactic nuclei (AGN) (Shirasaki et al., 2018). For example, models and simulations by Shirasaki et al. (2018) showed that these baryonic processes change the relationship between the density within a cluster and the critical density of the universe at the time of the cluster's formation. They found that the mass accretion histories of halos were not affected by baryonic effects, but that the concentration of those halos was increased. Given that structural properties such as concentration are significantly affected by baryons, these effects should be considered in cluster models and simulations (Shirasaki et al., 2018).

In recent years, simulations have been conducted to better understand the impact of baryonic physics on dark matter halos. These studies are valuable since our understanding of the structure of halos impacts our ability to accurately and precisely constrain cosmological parameters (Rudd et al., 2008; Shirasaki et al., 2018). Velliscig et al. (2014) demonstrated that including baryonic physics in simulations has a similar effect on cluster abundance as changing the cosmological parameters from those measured by WMAP7 (Komatsu et al., 2011) to those measured by Planck Collaboration et al. (2014). Similarly, Shirasaki et al. (2018) showed that the concentration of halos is more sensitive to the nature of baryonic physics than it is to the background cosmology. As a result, accurate simulations of baryonic effects on galaxies and clusters are necessary to properly model the growth of structure in the universe.

Baryonic physics alters the matter power spectrum on moderate scales by changing the mass distribution in virialized objects (Rudd et al., 2008). Different baryonic processes have different impacts on halos, and our treatment of these physics in simulations determines the structure of halos. Radiative cooling causes baryons to condense in the centre of a halo, deepening the gravitational potential and dragging dark matter into the centre (Rudd et al., 2008; Duffy et al., 2010). This in turn increases the concentration of the halo. Feedback due to supernovae and AGN moderates this effect by pushing material outward and reducing contraction (Duffy et al., 2010; Velliscig et al., 2014). In addition to changes in concentration, the efficiency of stellar and AGN feedback also affects the masses of halos. Velliscig et al. (2014) found in the OverWhelmingly Large Simulations (OWLS) that for halo masses of approximately $10^{11.5}\,M_\odot$ to $10^{12.5}\,M_\odot$, supernova feedback results

in a 20% reduction in the mass of a halo compared to dark matter only simulations. They also found that for halos up to 10^{15} solar masses, AGN could produce a similar decrease in mass. Using the same simulation suite, Duffy et al. (2010) also found that feedback can reduce the baryon content in clusters by a factor of a few. Similarly, Schaller et al. (2015a) made use of the Evolution and Assembly of Galaxies and their Environment (EAGLE) simulations and found that the mass of halos less than $10^{11}\,M_{\odot}$ is reduced by $\sim 30\%$ due to stellar feedback compared to dark matter only simulations. The mass reduction becomes fuelled by AGN for higher mass halos, and it gradually decreases until the halo is about 10^{14} solar masses. These results across a variety of simulations make clear that baryonic effects must be accurately modelled in order to properly compare simulations to real clusters and derive cosmological constraints.

1.4.2 Modelling Feedback

The two primary methods of implementing hydrodynamics in galactic simulations are Eulerian grid-based implementations and Lagrangian particle-based implementations, as discussed at the beginning of Section 1.4. For either of these implementations, hydrodynamical equations that conserve mass, momentum and energy are used to evolve the system (Shu, 1992). The implementation of feedback is particularly concerned with the heating and cooling of baryons, which we address presently.

Feedback is energy injected into a cosmological system from one of many different sources. Common sources of feedback are stellar winds, supernovae and AGN (Duffy et al., 2010; Muratov et al., 2015; Schaye et al., 2015, 2023). Feedback mechanisms transfer energy and momentum to nearby gas particles, preventing them from cooling and condensing. This in turn suppresses star formation (Duffy et al., 2010; Muratov et al., 2015). Very energetic feedback can push gaseous material outside of the galactic disc, changing the structure of galaxies significantly (Muratov et al., 2015).

Directly modelling feedback at the relevant physical scales would require spatial and mass resolutions that are computationally prohibitive in cosmological simulations. As a result, subgrid models are implemented to approximate these phenomena (Muratov et al., 2015; Schaye et al., 2015, 2023). A subgrid model is a framework within a simulation that estimates and implements the impact of processes that are not directly resolved. For example, a stellar feedback subgrid model records the density or pressure within simulation cells and converts gas particles to stars based on the state of each cell. The cell then models the energy and momentum transfer due to stellar winds and supernovae (Schaye et al., 2015, 2023).

Since subgrid physics are necessary to model hydrodynamical effects that are not directly resolved, the proper way to implement these processes is not immediately clear from physical first principles. As a result, the unresolved physics has led to inconsistencies between simulations and observations (Duffy et al., 2010; Schaye et al., 2015). For example, when energy from stellar feedback is distributed thermally to nearby particles, cosmological simulations have historically overcooled the systems. That is to say, the thermal energy dissipates radiatively before it can dynamically affect the system, and so it doesn't sufficiently suppress star formation (Muratov et al., 2015; Schaye et al., 2015, 2023). Since each particle in a simulation contains many solar masses of material, the feedback distributed over a few adjacent particles in a simulation may lead to far lower energy transfer per unit mass than would be expected in a real system (Schaye et al., 2015). Some of these challenges in modelling baryonic effects have been addressed in recent years. In the case of stellar feedback, a method that has been used to prevent this overcooling is to distribute the energy stochastically to fewer adjacent particles. This process increases the energy transfer per unit mass and has improved the results of simulations relative to observations (Schaye et al., 2015, 2023). However, some structural inconsistencies remain.

1.5 Motivation

Upcoming large astronomical surveys such as Euclid (Euclid Collaboration et al., 2019) and Vera C. Rubin Observatory's Legacy Survey of Space and Time (LSST) (Ivezić et al., 2019) will expand the available catalogues of observed galaxy clusters by more than an order of magnitude. This substantial increase in data provides opportunities to solve astrophysical questions and improve our understanding of the structure and evolution of the universe. This work aims to identify the observable properties of clusters in hydrodynamical simulations that can be used to constrain our cosmological model. By relating the properties of simulated clusters to existing observations, we aim to position ourselves to best leverage the coming increase in observational data.

Our concordance cosmological model outlined in Section 1.1 describes the history and large-scale structure of the universe using a few key parameters. As detailed in Section 1.1.3, the fraction of the universe's energy density comprised of matter Ω_m and the amplitude fluctuations in the matter distribution σ_8 determine the growth of structure in the universe. Modern constraints on these parameters derived from galaxy cluster abundance, gravitational lensing and other low-redshift tests are in statistical tension with constraints derived from observations of the CMB. This tension is highlighted in Figure 1.2, which compares a representative set of low-redshift measurements from the KiDS survey to

recent CMB constraints (Joudaki et al., 2018). We see in Figure 1.2 that the constraints on Ω_m and σ_8 from low-redshift measurements differ from Planck Collaboration et al. (2016) constraints from the CMB by ~ 2 standard deviations. Through the most recent results from the KiDS survey (Wright et al., 2025) are no longer in tension with Planck Collaboration et al. (2020) results, a recent review by Abdalla et al. (2022) shows the consistent discrepancy between CMB measurements and different low-redshift measurements using a variety of techniques. These low-redshift constraints generally feature the degeneracy between Ω_m and σ_8 highlighted in Figure 1.2. The difference between these low-redshift and high-redshift parameter constraints could be due to systematic errors in our measurements or due to some redshift evolution not captured by the concordance cosmological model. In either case, resolution of the tension would improve our understanding of the large-scale structure and history of the universe. It is also clear from Figure 1.2 that there is a degeneracy between the measurements of Ω_m and σ_8 from low-redshift structure, as is discussed in Section 1.2.3. Our ability to resolve the tension with CMB constraints is limited by the low-redshift measurement degeneracy. As is indicated by the nearly perpendicular cluster abundance and formation time contours in Figure 1.1, an improved understanding of galaxy cluster formation history can break the Ω_m and σ_8 degeneracy (Amoura et al., 2021). Estimates of median cluster age or abundances of recently formed structures would provide new insights into this tension in our cosmological model.

Given that the time scales of galaxy cluster formation are far too long to be observed directly, we must rely on structural properties of clusters that indicate their formation histories. In this work, we seek to relate observable parameters of clusters to their mass accretion histories. We do so by identifying the dynamical states of galaxy clusters from their optical properties and mass distributions. Since large structures grow hierarchically as described in Section 1.2, young clusters will have experienced recent mergers with other systems. As a result, they are dynamically unrelaxed, which is reflected in their structure. We identify dynamically relaxed and unrelaxed systems using a variety of structural measurements, then investigate the correlations between dynamical state and mass accretion history. With this understanding of halo formation times, we compare the structures of simulated galaxy clusters to observations of real clusters so that our results can be used with upcoming observational catalogues to better constrain our cosmological model and understand the tension with early-universe measurements.

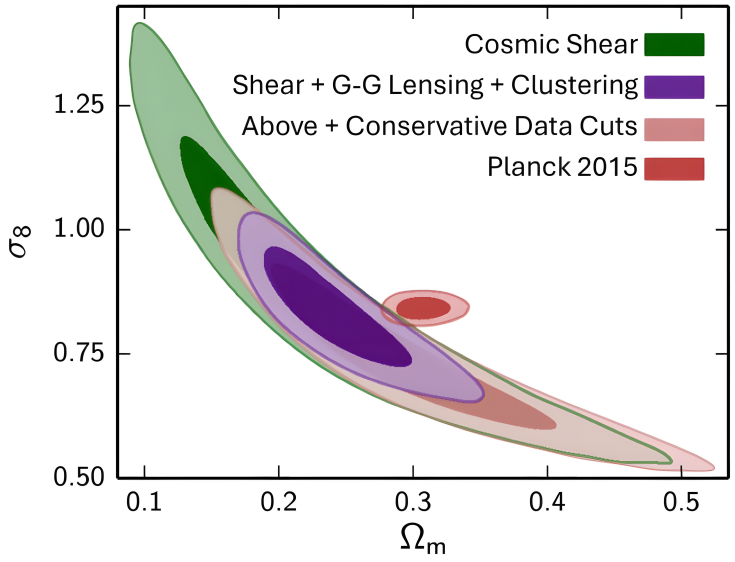


Figure 1.2: Constraints on the cosmological parameters σ_8 and Ω_m both from low-redshift structure and from the CMB. The green contours are constraints from cosmic shear measurements from the Kilo-Degree Survey (KiDS) by Joudaki et al. (2018). The purple contours combine cosmic shear, galaxy-galaxy lensing, and clustering through redshift-space power spectra. The pink contours are analogous to the purple contours, but with conservative data cuts on the spatial scales of lensing and the power spectra. The red contours are constraints from the Planck Collaboration et al. (2016) observations of the CMB. All inner contours are 68% confidence intervals, and outer contours are 95% confidence. Modified from Joudaki et al. (2018).

1.6 Outline of the Thesis

The main goal of this work is to relate the observable structure of galaxy clusters to the mass accretion histories of their dark matter halos. In Chapter 2, we discuss the suite of simulations that we use, the structural measurements that we perform on clusters, and the ways in which we compare the mass accretion histories of halos. In Chapter 3, we use the structural properties of galaxy clusters as indications of their recent merger history, and we compare the median mass accretion histories of clusters with different dynamical states. In Chapter 4, we discuss the optical selection of clusters, contrast the gravitational lensing profiles of dynamically relaxed and unrelaxed halo samples, and compare the structure of simulated clusters to that of real clusters from observational surveys. In Chapter 5, we summarise our main findings and discuss future work that will enable further applications of our results.

Chapter 2

Method

This chapter describes the suite of simulations analysed in this work, the structural measurements made on simulated halos, the mass accretion histories of those halos, and how we computed gravitational lensing profiles around them. The concepts and definitions established in this chapter will be used in Chapters 3 and 4 to explore the relationships between simulated galaxy cluster structure and formation history.

2.1 IllustrisTNG

The Next Generation Illustris (IllustrisTNG) is a suite of cosmological simulations that model the evolution of large sections of the universe from early fluctuations in the matter field to the formation of galaxies and galaxy clusters (Springel et al., 2018; Pillepich et al., 2018b; Nelson et al., 2018; Marinacci et al., 2018; Naiman et al., 2018). The suite features both dark matter only and magnetohydrodynamical (MHD) simulations with various volumes and resolutions. The dark matter only simulations are N-body simulations that model the gravitational interactions between representative dark matter particles. The MHD simulations also include gas, stellar and black hole particles that interact via magnetic fields, radiative cooling, star formation and feedback, metal enrichment and AGN feedback. The interactions of these baryonic processes are governed by adaptive grid physics. The grid cells conserve the mass, momentum, energy and magnetic field, and they evolve the baryonic components of the simulation (Pillepich et al., 2018a). The adaptive grid follows the flow of baryonic particles in the simulation and improves its resolution in high-density areas. All IllustrisTNG simulations assume a ΛCDM cosmology

with cosmological parameters from the Planck Collaboration et al. (2016) results. Notably, $\Omega_\Lambda = 0.6911$, $\Omega_m = 0.3089$, $\Omega_b = 0.0486$, and $H_0 = 67.74$ km/s/Mpc. This work primarily makes use of the TNG300-1 simulation. This is the highest-resolution realisation of IllustrisTNG's largest volume baryonic simulation. TGN300-1 is run in a cubic box with 205 cMpc/h side lengths and periodic boundary conditions. It contains 2500^3 dark matter particles with masses of $5.9e7\,M_\odot$, and it contains an equal number of baryonic particles. Unless otherwise stated, all simulation results presented in this work are derived from the TNG300-1 simulation.

In the publicly available IllustrisTNG data[1], subhalos represent galaxies and satellites, while halos represent groups and clusters of galaxies. Halos are identified using a FoF algorithm with a linking length $b = 0.2$ times the mean inter-particle distance. The FoF algorithm considers any two particles within the maximum linking length b as "friends." It then groups all particles that are "friends of friends" into a single halo (Press & Davis, 1982; More et al., 2011). Subhalos are defined using the SUBFIND algorithm, which identifies gravitationally bound overdensities of particles within halos (Springel et al., 2001; Onions et al., 2012). The most massive subhalo within each parent halo contains the most massive galaxy in the parent, but also includes the particles from most of the less dense regions of the halo. The rest of the subhalos typically contain only local overdensities within the parent. These components are illustrated in Figure 2.1, which shows the total surface mass density of a massive halo in the TNG300-1 simulation and its three most massive subhalos. The top left panel shows the mass distribution of the full halo, and the top right panel shows the most massive subhalo. We see that the primary subhalo contains the brightest cluster galaxy (BCG), as well as all of the diffuse mass in the halo. The bottom two panels show the next most massive subhalos, which contain only the local mass associated with their respective galaxies.

2.2 Simulation Volume Cuts

The particle data in a full TNG300-1 simulation snapshot comprises 4.0 TB of data. The positions, masses and types of all particles in a snapshot comprise 1.2 TB of that data. Since the data set is so large, only small divisions of the data can be used at a time. The data structure provided by IllustrisTNG enables all of the particles associated with a FoF halo as described in Section 2.1 to be loaded in a manageable format. However, for certain properties of galaxy clusters, such as asymmetry in Section 3.4 or gravitational lensing in

[1] https://www.tng-project.org/data/

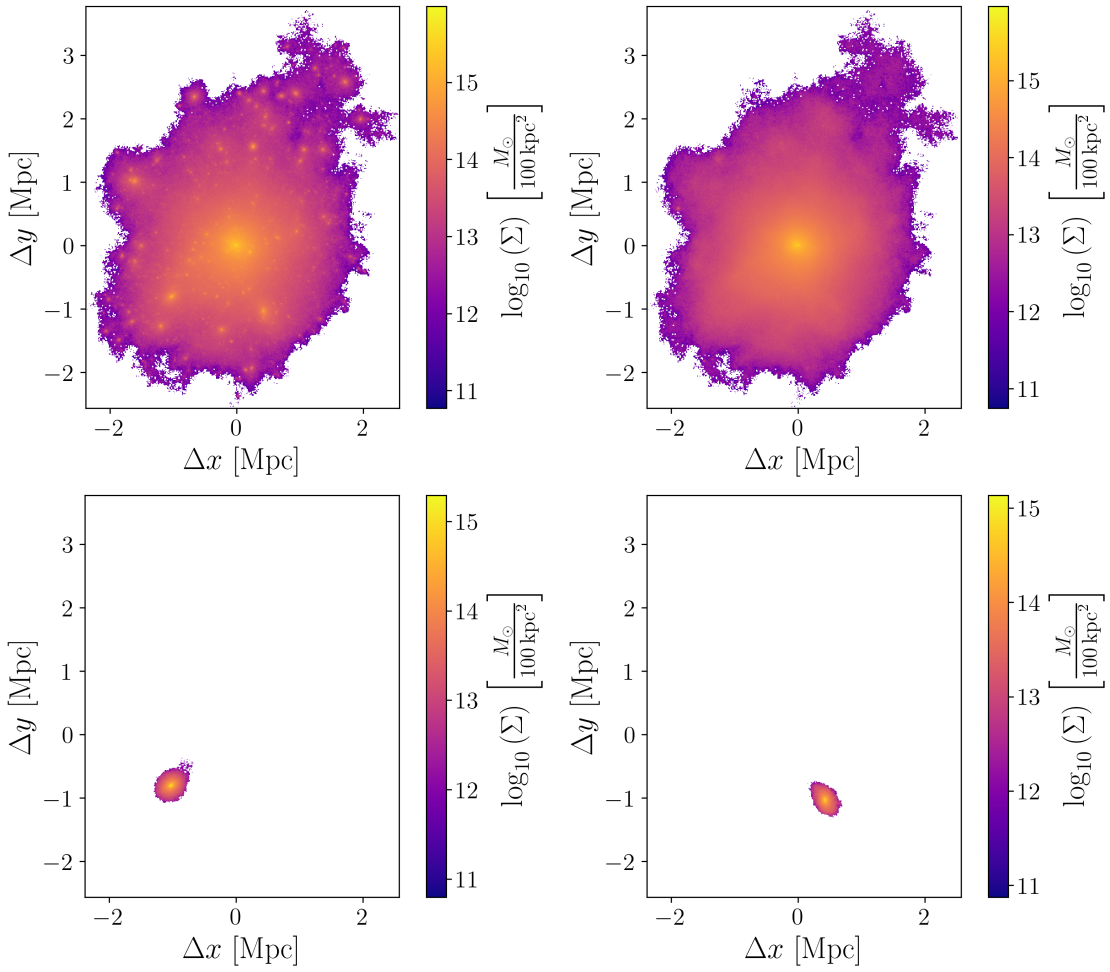


Figure 2.1: The total surface mass density Σ of a massive halo and its most massive subhalos at redshift $z = 0$ in the TNG300-1 simulation. The total mass of all components is projected along the z-axis, with the surface mass density in colour scale. The top left panel shows all of the mass associated with the halo, as defined by IllustrisTNG's FoF algorithm. The top right panel shows the mass associated with the most massive subhalo, as defined by IllustrisTNG's SUBFIND algorithm. The bottom two panels show the mass associated with the next two most massive subhalos.

Chapter 4, we make use of full volumes of particles from the TNG300-1 simulation that extend beyond FoF halos. There is no native structure within the IllustrisTNG data that enables loading small volumes of particles in arbitrary positions without searching through the positions of all particles in the simulation. This makes loading volumes of particles around halos impractical. To solve this problem, we created a catalogue of 9261 files that divide the TNG300-1 simulation volume into cubic chunks with 10 Mpc/h side lengths. These files contain the positions, masses and types of all particles in the simulation, and they range from a few MB to a few GB in size. These volume chunks enable us to determine the mass distributions within arbitrary volumes of the IllustrisTNG simulation.

An application of our volume chunking is presented in Figure 2.2, which depicts the surface mass density of the most massive halo in the TNG300-1 simulation. The left panel shows the mass distribution of all particles within the FoF halo defined by IllustrisTNG. The right panel shows the surface mass density of all particles within the eight volume chunks surrounding the same halo. We see that the halo in the left panel of Figure 2.2 is also visible in the mass distribution on the right. Nearby galaxies, groups and large-scale structures surrounding the halo are also visible in the full-volume cutout.

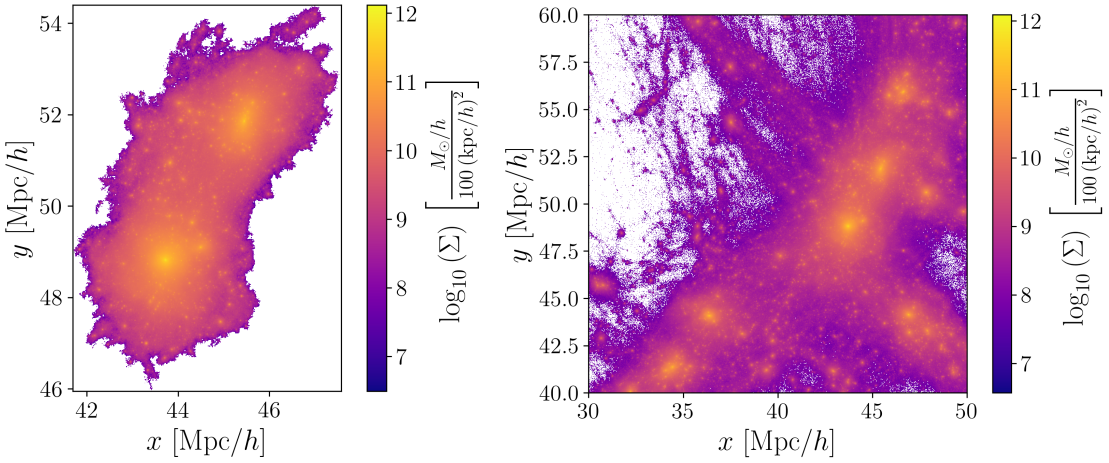


Figure 2.2: The surface mass density Σ of the most massive halo at redshift $z = 0$ in the TNG300-1 simulation. The total mass of all components of the halo is projected along the z-axis, with the surface mass density in colour scale. The left panel shows only the particles considered as part of the halo as defined by IllustrisTNG's FoF algorithm. The right panel shows all particles within a cubic volume which contains the halo with 20 Mpc/h side length.

2.3 Structural Measurements

This section provides definitions of the structural measurements of halos that are used as indicators of dynamical state and mass accretion history throughout this work. Analyses of the correlations between these measurements, the mass accretion histories of halos, and other indicators of structure are presented in Chapters 3 and 4.

2.3.1 Centre of Mass Offset

The centre of mass offset of a halo is defined by Amoura (2023) as the distance between the centre of mass and the peak of the density contours in a halo. It is similarly defined by Power et al. (2012) as the distance between the centre of mass and the centre of density. In contrast, Macciò et al. (2007) define the offset as the distance between the centre of mass and the most bound particle in a halo, which they take to be the centre of the density profile. In this work, we define the centre of mass offset relative to the location of the most bound particle in a halo. In the IllustrisTNG simulations, this is identified as the particle with the most negative potential energy. The most bound particle generally lies in the centre of the BCG, which makes it an easy point to identify observationally as well as in simulations.

In order to compute the centre of mass for each halo, we require the locations of the most bound particle and the centre of mass. The IllustrisTNG simulation results contain a data field for each halo that specifies the coordinates of the most bound particle. We compute the centre of mass ourselves using the standard formula:

$$x_{\mathrm{cm}} = \frac{\sum_{i=1}^{N} m_i x_i}{\sum_{i=1}^{N} m_i}\,, \tag{2.1}$$

where x_{cm} is the position of the centre of mass along some axis, and where m_i and x_i are the mass and position along the same axis of the i^{th} halo particle. Three-dimensional centres of mass are computed along the axes of the simulation box. Projected centres of mass simply discard position information along the chosen line of sight axis. Our centre of mass computation was validated by comparing it with the simulation's own determination of the centres of mass of various halos, which are only available for the Illustris-3 simulation run.

The centre of mass can be computed either from all of the particles in the FoF halo identified by IllustrisTNG or from only the particles within some radius around the most

bound particle. Unless otherwise stated, the results shown in this work compute centres of mass only from the particles within R_{200c}. The centre of mass offset within this radius is more stable during halo mergers than the offset computed from the full FoF halo. In FoF halos, the centre of mass instantaneously increases when two merging systems come within the somewhat arbitrary FoF linking length. In contrast, the centre of mass offset within R_{200c} increases gradually during mergers as infalling material enters the target radius.

The positions of the centre of mass and the most bound particle are plotted over the surface mass densities of two massive halos in Figure 2.3. In this figure, the centre of mass is computed from all of the particles in the FoF halo so as to maximise the visual difference between its position and that of the most bound particle. The left panel depicts a merging system in which we see that the most bound particle is in the centre of the most dense region, while the centre of mass is offset toward the middle of the halo's mass distribution. The right panel depicts a dynamically relaxed system in which the most bound particle and the centre of mass are at nearly the same point in the centre of the halo.

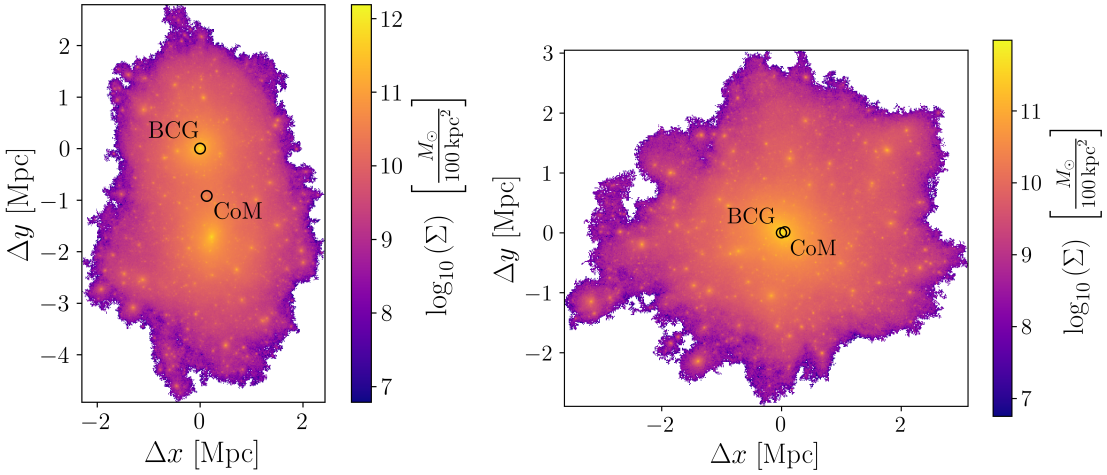


Figure 2.3: The surface mass densities Σ of two massive halos at redshift $z = 0$, as defined via a FoF algorithm by the TNG300-1 simulation. The total mass of all components of the halos are projected along the z-axis, with the surface mass densities in colour scale. The circles labelled "BCG" are centred on the most bound particle, which resides in the centre of the BCG. The circles labelled "CoM" are at the centres of mass of the clusters.

2.3.2 Axis Ratio

The axis ratio of a halo is the ratio of the lengths of the principal axes of the halo. The principal axes are equivalent to the preferred axes of rotation of an object with a similar mass distribution (Bett, 2012). This structural measurement is computed from the mass distribution of a halo, and it indicates the elongation of the system. Axis ratios are an indicator of dynamical state, as young and disturbed systems are often elongated due to mergers, while old and relaxed systems are more spherical. The principal axes of a massive halo in the TNG300-1 simulation and their relative lengths are illustrated in Figure 2.4. The directions of the black lines represent the principal axes of the halo, and their relative lengths indicate the elongation of the mass distribution along those axes.

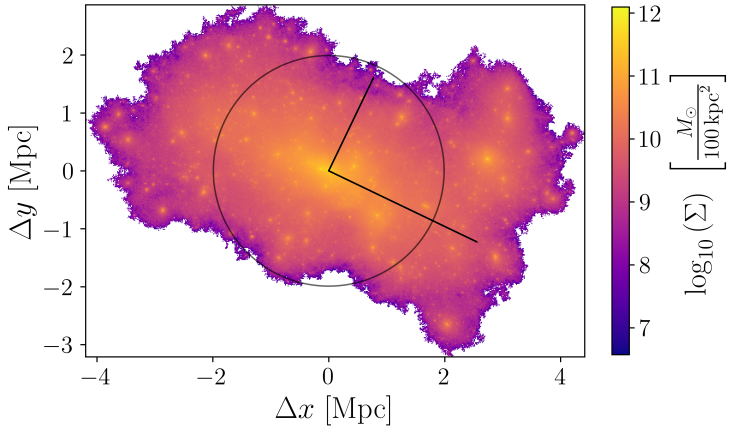


Figure 2.4: The surface mass density Σ and principal axes of a massive projected halo at redshift $z = 0$ in the TNG300-1 simulation. The total mass of all components of the FoF halo are projected along the z-axis, with the surface mass density in colour scale. The black circle represents R_{200c}, centred on the most bound particle. The two black lines begin at the most bound particle and extend in the direction of the principal axes of the projected particle distribution within R_{200c}. The relative lengths of the lines indicate the elongation of the mass distribution of the halo in each direction.

Axis ratios for halos in the IllustrisTNG simulation suite have been computed by Anbajagane et al. (2022) and made publicly available in a supplementary data catalogue[2]. The

[2] https://www.tng-project.org/data/docs/specifications/

axes of a halo are defined in Anbajagane et al. (2022) as the eigenvectors of the tensor:

$$M_{ij} = \frac{1}{N}\sum_{k=1}^{N}\left(x_{k,i} - \langle x_i\rangle\right)\left(x_{k,j} - \langle x_j\rangle\right) , \tag{2.2}$$

where $x_{k,i}$ is the $i^{\rm th}$ Cartesian component of the $k^{\rm th}$ particle within R_{200c} of the halo, and $\langle x_i\rangle$ is the $i^{\rm th}$ Cartesian component of the most gravitationally bound particle in the halo. Anbajagane et al. (2022) refer to this tensor as the "quadrupole moment tensor". In other works, it is alternatively referred to as the "tensor of the quadrupole moments of the mass distribution" (Bett, 2012) and the "second moment of the mass distribution" (Wong & Taylor, 2012). Bett (2012) shows that the tensor M is related to the inertia tensor I, such that:

$$I_{ij} = {\rm Tr}(M)\delta_{ij} - M_{ij} . \tag{2.3}$$

The axes computed from the tensor M can equivalently be determined by diagonalising the moment of inertia tensor I, though this is generally more difficult (Bett, 2012; Wong & Taylor, 2012). The eigenvectors of M give the principal axes of the halo, which are the principal axes of an ellipsoid with the same moment of inertia (Bett, 2012). The square roots of the eigenvalues of M are then the relative lengths of these principal axes (Bett, 2012; Wong & Taylor, 2012; Anbajagane et al., 2022). More explicitly:

$$a = \sqrt{\lambda_1} \quad > \quad b = \sqrt{\lambda_2} \quad > \quad c = \sqrt{\lambda_3} , \tag{2.4}$$

where $\lambda_1 > \lambda_2 > \lambda_3$ are the eigenvalues of the matrix M, and $a > b > c$ are the relative lengths of the axes. Note that the magnitudes of a, b and c are not taken here to be physically meaningful in themselves. Rather, their ratios are used as measurements of the elongation of a halo. The axis ratios are naturally given by:

$$s = \frac{c}{a} = \sqrt{\frac{\lambda_3}{\lambda_1}} \quad , \quad q = \frac{b}{a} = \sqrt{\frac{\lambda_2}{\lambda_1}} \quad , \quad p = \frac{c}{b} = \sqrt{\frac{\lambda_3}{\lambda_2}} , \tag{2.5}$$

as is shown in Anbajagane et al. (2022). We note here that when computing the axis ratios, the factor of $1/N$ in Equation 2.2 cancels out in Equation 2.5. As such, the term is not included in the equivalent expressions for M defined in Bett (2012); Wong & Taylor (2012). If the particles over which the shape of a halo is computed have non-uniform masses m_k, then their masses must be included in the tensor M as follows:

$$M_{ij} = \sum_{k=1}^{N} m_k \left(x_{k,i} - \langle x_i\rangle\right)\left(x_{k,j} - \langle x_j\rangle\right) . \tag{2.6}$$

Particle masses were included in the expression for M by Bett (2012) as well as Wong & Taylor (2012), but omitted by Anbajagane et al. (2022) since the dark matter particles over which they computed axis ratios are of equal mass.

Since dark matter halos are generally triaxial, we define the minor-to-major axis ratio as $s = c/a$ and the middle-to-major axis ratio as $q = b/a$. Most results involving axis ratios presented in this work were produced using both of these measures. All of the correlations between these two axis ratios and other parameters were very similar, though correlations with $s = c/a$ tended to be slightly stronger. Thus, only minor-to-major axis ratios $s = c/a$ are presented in this work for brevity.

To compute an axis ratio from a projected particle distribution, we simply constructed the quadrupole moment tensor from Equation 2.6 while omitting the Cartesian coordinate along the line of sight axis. Due to the reduction in dimension, the projected distribution gives a 2x2 tensor rather than a 3x3 tensor. Since this only produces two eigenvalues, the ratio of these eigenvalues is the sole axis ratio that can be computed for a projected halo. It should be noted that the axes identified from the projected mass distribution of a halo are not the same as the projection of the axes computed from the three-dimensional mass distribution. Rather, since the line of sight information is lost to projection prior to the calculation of the principal axes, the axes identified from the projected mass are in general different in direction and length ratio than in the three-dimensional case. This is illustrated in Figure 2.5, where the dashed lines represent the projection of the three-dimensional axes of a massive halo, while the solid lines represent the axes of the projected mass distribution.

The catalogue of halo axis ratios provided in the IllustrisTNG data by Anbajagane et al. (2022) makes some approximations in its computation of the quadrupole moment tensor in Equation 2.2. Firstly, their computation of the halo shape was done using only the dark matter particles in the simulation, while omitting the gas, stars and black holes. In order to get results that reflect the entire mass distribution of a halo, baryons should be included for the hydrodynamical simulations. In addition, Anbajagane et al. (2022) constructed the tensor in Equation 2.2 from only the particles in the primary subhalo for each system, not from all of the particles in the total halo. The difference between the primary subhalo and total halo in IllustrisTNG is highlighted in Figure 2.1 and explained in Section 2.1. While the most massive subhalo accounts for the majority of the halo's total mass, the overdensities representing most member galaxies are omitted. This affects the computation of axis ratios, which are based on the mass distribution and should in general include those galaxies. The axis ratios shown in this work, both three-dimensional and projected, include the mass of all particle types in the total FoF halos as an improvement on the process outlined by Anbajagane et al. (2022).

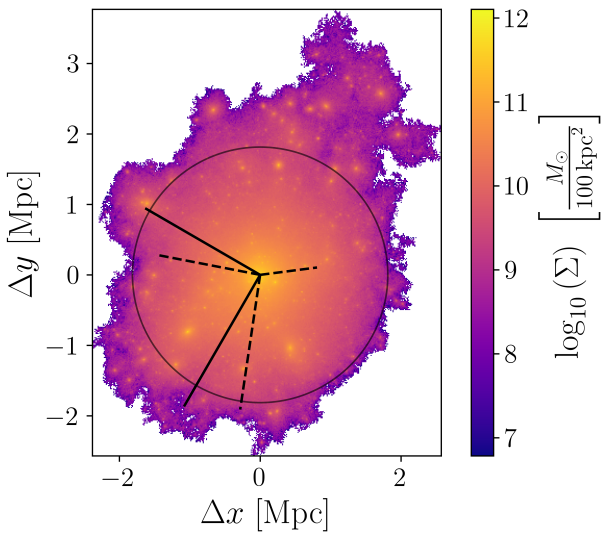


Figure 2.5: The surface mass density Σ and principal axes of a massive halo at redshift $z = 0$ in the TNG300-1 simulation. The total mass of all components of the FoF halo are projected along the z-axis, with the surface mass density in colour scale. The black circle represents R_{200c}, centred on the most bound particle. The two solid black lines represent the principal axes of the projected particle distribution within R_{200c}. The three dashed black lines represent the same for the 3D particle distribution, projected into the xy-plane. The lines begin at the most bound particle, and their relative lengths indicate the elongation of the mass distribution of the halo in each direction.

Axis ratios can be computed either from all particles in the FoF halo identified by IllustrisTNG or from only the halo particles within some radius of the most bound particle. The results shown in this work compute axis ratios only from the particles within R_{200c}. This provides a measurement that is more stable during halo mergers, as the axis ratio does not instantaneously change when two merging systems come within the FoF linking length. Rather, the axis ratio changes gradually during mergers as infalling material enters the R_{200c} radius.

2.3.3 Concentration

As described in Section 1.3.2, the concentration c of a halo is defined in terms of the NFW density profile of the halo (Navarro et al., 1996, 1997). In particular, it is defined as $c = r_{\rm vir}/r_s$, where $r_{\rm vir}$ is the virial radius of the halo, and r_s is the scale radius as defined in Equation 1.3.2. The virial radius indicates the boundary of the spherical region within which the kinetic energy of the mass reaches equilibrium under gravitational collapse (Mo et al., 2010). The scale radius is computed by fitting an NFW profile with free parameter r_s to the mass distribution of a halo.

A supplementary data catalogue produced by Anbajagane et al. (2022) is provided with the IllustrisTNG simulation data, which contains concentration values for all halos identified by the friend-of-friends algorithm. This concentration is defined as:

$$c_{200c} = R_{200c}/r_s \,, \tag{2.7}$$

where R_{200c} is the radius around the most bound particle of a halo within which the mean density is 200 times the critical density of the universe, and where r_s is the NFW scale radius. In halos, R_{200c} roughly corresponds to the virial radius $r_{\rm vir}$, and it is in general much easier to identify (Navarro et al., 1997). Anbajagane et al. (2022) computed the scale radius r_s by fitting a three-dimensional NFW profile to the dark matter density profile of the most massive subhalo of each halo. The difference between the primary subhalo and total halo in IllustrisTNG is highlighted in Figure 2.1 and explained in Section 2.1. The concentration could in principle be recomputed to trace the entire mass distribution of the halo, including gas, stars, black holes and galaxy subhalos. Given the small modification that these factors have on the shape of halos, we expect that the concentrations would only be modified at the few percent level with the same corrections.

For simplicity, the c_{200c} concentrations provided in the IllustrisTNG catalogue by Anbajagane et al. (2022) are used throughout this work. While definitions of concentration based on more precise measurements of the virial radius $r_{\rm vir}$ and of the scale radius r_s may

slightly alter the values for each halo, they are not expected to have a significant impact on the correlations between concentration and other parameters presented in Section 3.3.

2.3.4 Asymmetry

The asymmetry of a halo is a measurement of the fluctuations in the projected mass or brightness distribution that are not symmetric around the BCG. Asymmetry is quantified by the symmetry number A, which is defined by Conselice (1997) as:

$$A^2 = \frac{\sum 1/2 \left(I_0 - I_{180}\right)^2}{\sum I_0^2}\,, \tag{2.8}$$

where I_0 is the image of an object and I_{180} is the image rotated by 180°. This expression quantifies how much signal from the image of a halo is not equally represented on the other side of the halo centre. Motivated by this definition of asymmetry A, we adopt the following measurement for asymmetry from a simulated particle distribution:

$$A_{\rm halo} = \frac{\sum_i \left(m_i - m_{i,180}\right)^2}{\sum_i m_i^2}\,, \tag{2.9}$$

where m_i is the mass in a bin i of the projected particle distribution, and $m_{i,180}$ is the mass in the bin 180° around the halo at the same radius. In Chapters 3 and 4, we compare the values of $\log_{10}(A_{\rm halo})$ for various clusters. Since our analysis depends only on the relative values of asymmetry between systems, we omit the scalar factor of 1/2 from Equation 2.8 in the definition of $A_{\rm halo}$ for simplicity. Likewise, we define $A_{\rm halo}$ rather than $A^2_{\rm halo}$ in Equation 2.9 since the factor of 2 would reduce to a scalar when taking $\log_{10}(A_{\rm halo})$. When computing the halo asymmetry in practice, it is more computationally efficient to only compute the numerator in Equation 2.9 for half of the angular bins and then multiply the sum by 2. This gives the same result for $A_{\rm halo}$ as a full calculation of Equation 2.9 since the rotated and stacked halos are symmetric about any line through the halo centre.

In this work, we compute asymmetry by dividing the projected mass distribution around the most bound particle of a halo into equally spaced radial and angular bins, then applying Equation 2.9 to the mass in the bins. The most bound particle generally lies in the centre of the BCG, which provides a clear shared reference point between simulations and observational data. We consider only particles within some specified radius tangent to the line of sight and some depth along the line of sight from the most bound particle, which produces a cylinder of mass along the line of sight. An example of the particle binning is provided in Figure 2.6. The left panel of this figure shows the surface mass density of a

massive halo in the TNG300-1 simulation. The right panel shows the same distribution split into 6 radial and 12 angular bins, yielding a total of 72 bins. For the analyses in Sections 3.4 and 4.1, we split the halo surface masses into 20 radial bins and 50 angular bins. These bin numbers were chosen as asymmetry measurements were found to be robust to changes in bin number around these values.

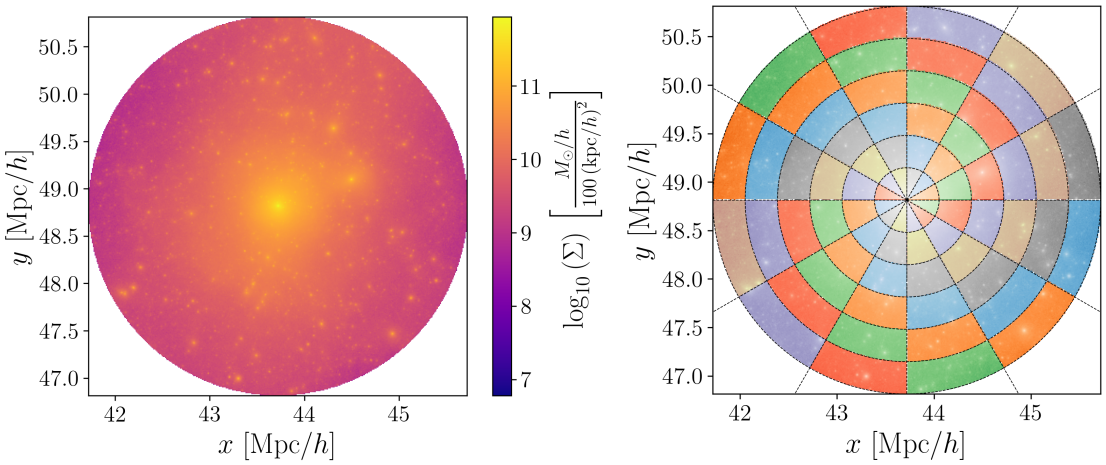


Figure 2.6: The surface mass density Σ around a massive halo at redshift $z = 0$ in the TNG300-1 simulation, sorted into evenly spaced angular and radial bins. The total mass of all components within a 2 Mpc/h radius tangent to the z-axis and ± 5 Mpc/h along the z-axis around the most bound particle in the halo are projected into the xy-plane. The left panel shows the surface mass density in colour scale. The right panel shows the same information, with the colour scale of the histogram changed for particles in different bins.

In contrast to other structural measurements described in this section, we compute the asymmetry of halos from full volume cuts of particles rather than only from particles associated with the FoF halo. This enables us to sample the total mass distribution at greater distances from the centre of the halo.

2.3.5 Magnitude Gap

The magnitude gap of a galaxy cluster is typically defined as the difference between the magnitudes in a given spectral band of two bright galaxies in the cluster (Dariush et al., 2010; More, 2012). Magnitude gaps are sometimes taken between the two most luminous galaxies within some radius of the BCG, such as a multiple of r_{vir} (Jones et al., 2003).

They may also be computed between the brightest galaxy and the third or fourth brightest galaxy in a cluster, which may correlate well with hierarchical growth of the BCG (Dariush et al., 2010; Golden-Marx et al., 2024).

In Sections 3.5 and 4.1, we compute magnitude gaps for galaxy clusters in various photometric bands. The galaxy magnitudes provided by IllustrisTNG's catalogue are computed by summing the luminosities of all of the stellar particles in a given subhalo. As explained in Section 2.1, the particles associated with the primary subhalos in a cluster represent both the most massive galaxy and much of the diffuse mass in the cluster. For stellar particles, the primary subhalo includes the BCG and the diffuse stars that contribute to intracluster light. This is illustrated in Figure 2.7, where the top left panel shows the stellar mass distribution of the full halo, and the top right panel shows the most massive subhalo. We see that the primary subhalo is comprised of stars well outside of the central galaxy. The bottom two panels show the next most massive subhalos, which contain only the stellar mass associated with their respective galaxies. In order to produce consistent measurements, we compute magnitudes of galaxies using 30 kpc radius apertures around the centres of subhalos. This radial aperture size was found to be appropriate for comparing simulated galaxies to observations, as it provides mass estimates comparable to observational measurements within the Petrosian radius (Schaye et al., 2015; Pillepich et al., 2018b; Engler et al., 2021). In order to compute the magnitude of a given galaxy within some radius of the galaxy's centre, we must sum the magnitudes of the stellar particles within the desired radius. The definition of magnitude in terms of luminosity is:

$$M = M_0 - 2.5 \log_{10} \left(\frac{L}{L_0} \right) , \tag{2.10}$$

where M_0 and L_0 are reference magnitudes and luminosities (Hubble, 1936; Mo et al., 2010). Given the logarithmic definition of magnitude in terms of luminosity, the magnitudes of stellar particles cannot be added linearly to compute the magnitude of the host galaxy. Rather, we first convert the stellar magnitudes M_i to luminosities $L_i = 10^{-0.4 M_i}$, then sum the luminosities, and finally convert back a magnitude for the galaxy. This process takes the mathematical form shown in, e.g., Piskunov et al. (2008); Kharchenko et al. (2016):

$$M_{\text{gal}} = -2.5 \log_{10} \left(\sum_{i}^{N} 10^{-0.4 M_i} \right) , \tag{2.11}$$

where M_{gal} is the magnitude of the galaxy and M_i are the magnitudes of its N stellar particles. In addition to the traditional magnitude gap, we also define the mass gap as the difference between the logarithm of the stellar masses of the two most massive subhalos.

Since the stellar mass-to-light ratios of galaxies vary, the mass gap between galaxies is in general different from their magnitude gap. We compute the difference of the logarithm of the stellar masses rather than the linear mass difference because the magnitude M of a system is defined in terms of the logarithm of its luminosity L, as shown in Equation 2.10. Stellar mass can be related to luminosity, so the difference in the logarithm of stellar mass is analogous to the difference in magnitude.

2.4 Velocity-Depth Cluster Identification

In order to compute structural parameters of clusters based on their galaxy distribution, we must identify all galaxies and satellites that are a part of that cluster. While this can be done reliably in simulations by identifying the subhalos in a parent halo in three dimensions, observations of real clusters must rely often on redshift measurements for line of sight distances in order to identify cluster members. Redshifts indicate the line of sight velocities of subhalos, so a cut in relative line of sight velocities for galaxy cluster members is equivalent to a cut in spectroscopic redshift. To ensure that our galaxy-based measurements in Chapter 3 are maximally observable quantities, we may select member galaxies for each cluster based on their velocity along the z-axis relative to that of the BCG. To measure the velocity differences between subhalos and BCGs in IllustrisTNG, we must consider both their peculiar velocities and their Hubble flow velocities. The peculiar velocity of a subhalo is simply the component of its motions not due to the expansion of the universe. Peculiar velocities are provided by the IllustrisTNG data as the mass-weighted sums of the velocities of all of the particles in a subhalo. The Hubble flow velocity of a subhalo is the component of its velocity that is due to the expansion of the universe. To compute the relative Hubble flow velocities of subhalos, we first compute the distance d along the line of sight between subhalos. Then, we use the standard equation:

$$v_H = d \cdot H(z)\,, \tag{2.12}$$

to compute the Hubble velocity v_H, where:

$$H(z) = H_0\sqrt{\Omega_r\,(z+1)^4 + \Omega_m\,(z+1)^3 + \Omega_k\,(z+1)^2 + \Omega_\Lambda} \tag{2.13}$$

is the Hubble parameter as given in Ryden (2016). The cosmological parameters H_0, Ω_r, Ω_m, Ω_m and Ω_Λ in Equation 2.13 are consistent with those from the Planck Collaboration et al. (2016) results. With the peculiar velocities and Hubble flow velocities along the line of sight, we then take their sum to get the total velocity difference between the BCG and

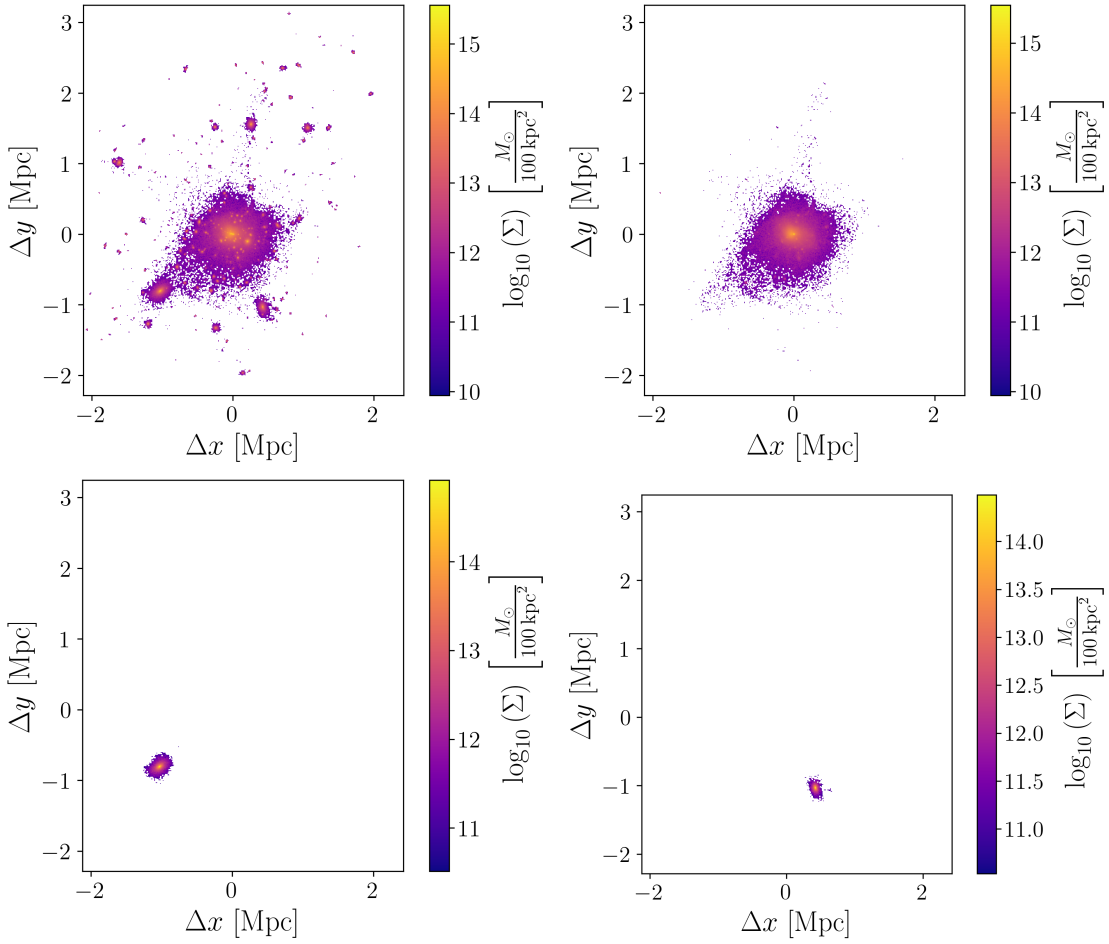


Figure 2.7: The stellar surface mass density Σ of a massive halo and its most massive subhalos at redshift $z = 0$ in the TNG300-1 simulation. The stellar mass is projected along the z-axis, with the surface mass density in colour scale. The top left panel shows all of the stellar mass associated with the halo, as defined by IllustrisTNG's FoF algorithm. The top right panel shows the stellar mass associated with the most massive subhalo, as defined by IllustrisTNG's SUBFIND algorithm. The bottom two panels show the stellar mass associated with the next two most massive subhalos.

the other subhalos in the simulation. For a given cluster, we include all subhalos within some radius tangent to the z-axis and some total velocity along the z-axis as part of the cluster. Using this method, we produce distributions of galaxies in clusters as shown in Figure 2.8. In the top two panels, we see the spatial distribution of subhalos in a massive cluster within ±1,000 km/s along the line of sight. We see that in these panels, most of the selected subhalos are within the parent halo. Some nearby galaxies are projected into the cluster due to their peculiar velocities relative to the BCG being small. While velocity cuts of less than ±1,000 km/s do cut out these projected systems, they also cut out many of the galaxies that are genuine members of the cluster. In the bottom two panels of Figure 2.8, we see the spatial distribution of subhalos around the same cluster within ±10,000 km/s along the line of sight. In these panels, we see that many galaxies are projected into the cluster as a consequence of the large line of sight velocity threshold. Due to the large velocity dispersions in massive clusters, no velocity depth threshold can include all of the member galaxies in a cluster while also excluding all projected galaxies. As a result, some velocity cut must be selected to compromise between completeness and contamination of cluster members. All measurements that use velocity depths presented in this work use velocity cuts along the line of sight of ±1,000 km/s relative to the BCG.

2.5 Mass Accretion History

In order to describe the mass accretion histories of halos in the IllustrisTNG simulations, we made use of the merger trees provided in the IllustrisTNG data. Due to hierarchical structure formation, any given subhalo has many progenitors that gradually merge together. These progenitors form a given halo's "merger tree". These merger trees in IllustrisTNG track groups of gravitationally bound particles through snapshots of the simulation as it evolves. IllustrisTNG provides a main branch progenitor for each subhalo, which tracks its most massive progenitors through the simulation snapshots. These trees exist only for subhalos and not for full FoF halos. As explained in Section 2.1 and illustrated in Figure 2.1, the most massive subhalo identified by the SUBFIND algorithm contains the vast majority of the FoF halo's mass. Given this, it is assumed in this work that the main progenitor of the primary subhalo reflects the main progenitor of its parent halo. To determine the mass accretion history of a given halo, we first extracted the main progenitor branch from the merger tree of the most massive subhalo. From these main progenitor subhalos, we then determine the masses of their parent halos.

Previous work by Amoura (2023) defined the mass of a halo as the mass contained within R_{200c}, the radius whose average internal density is 200 times the critical density of

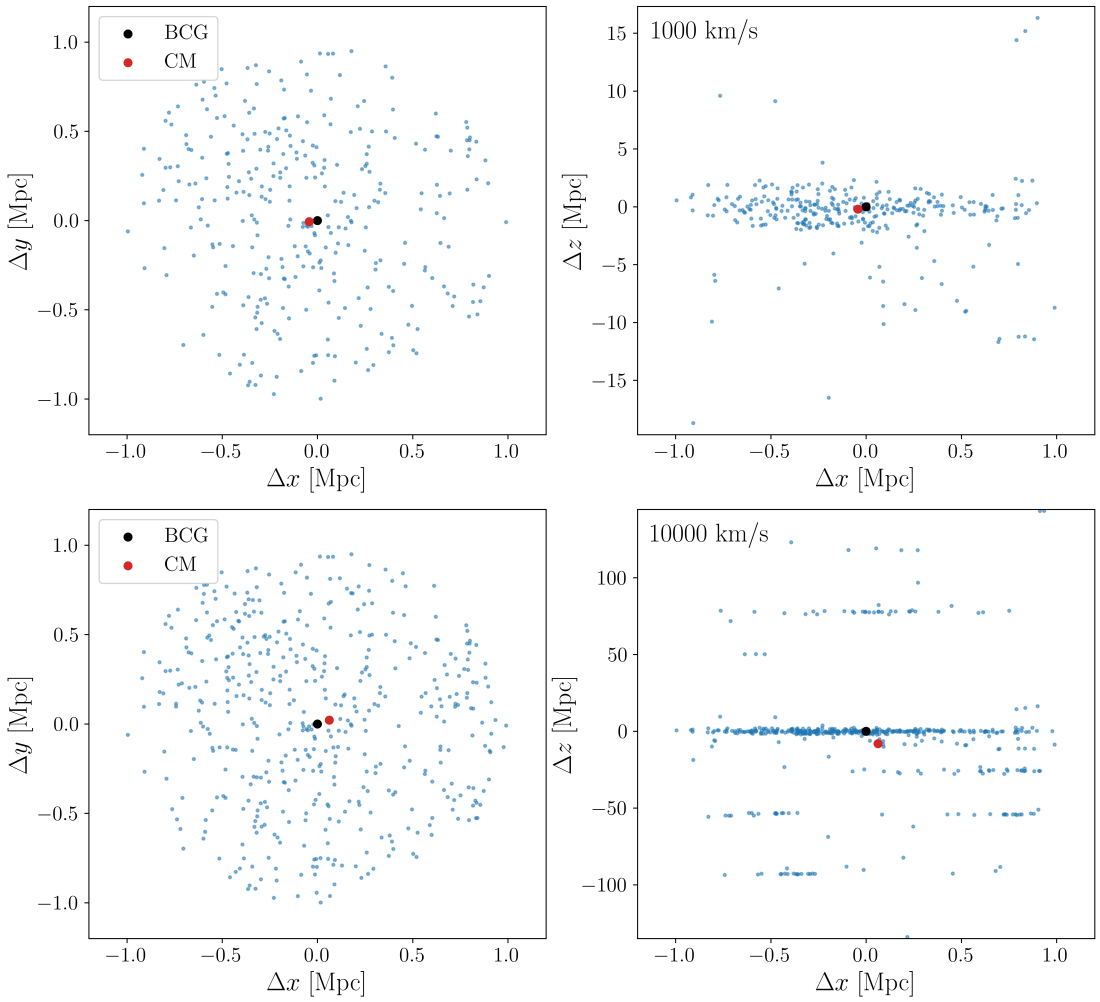


Figure 2.8: The spatial distribution of subhalos with non-zero stellar mass around the brightest galaxy of the 100th most massive cluster at redshift $z = 0$ in the TNG300-1 simulation. The blue dots represent the subhalos, the black dot represents the BCG, and the red dot represents the centre of mass of the stellar mass of the subhalos. Subhalos within 1 Mpc tangent to the z-axis are included. The top two panels include subhalos with a velocity within 1000 km/s of the BCG, while the bottom two panels include subhalos within 10000 km/s of the BCG.

the universe. We represent this definition of the halo mass as $M_{\rm halo} = M_{200c}$. To maintain consistency with Amoura's method, this work uses the same definition of the halo mass for all presented mass accretion histories and mass history parameters. The choice to include only the particles within R_{200c} provides a more stable definition of halo mass over simulation snapshots than the mass of the full FoF halo, which is in general larger. The full halo mass $M_{\rm FoF}$ is an unstable mass measurement because it is subject to the sudden mass increases and decreases during halo mergers as two systems suddenly come within the grouping algorithm's linking length, as described in Section 2.1. In contrast, M_{200c} increases more gradually as an infalling cluster merges into the inner regions of a more massive cluster.

In the context of mass accretion histories in IllustrisTNG, the redshift of a simulation snapshot refers to the age of the universe at the time of the snapshot. Redshift z can be related to the age of the universe t via:

$$t(z) = \frac{1}{H_0} \int_z^\infty dz \left[\Omega_{\Lambda,0} \left(1+z\right)^2 + \left(1-\Omega_0\right)\left(1+z\right)^2 + \Omega_{m,0}\left(1+z\right)^2 + \Omega_{r,0}\left(1+z\right)^2\right]^{-1/2} , \tag{2.14}$$

where H_0 is the Hubble constant, and where $\Omega_{\Lambda,0}$, $\Omega_{m,0}$ and $\Omega_{r,0}$ are the energy densities of dark energy Λ, matter m and radiation r at redshift $z = 0$ (Ryden, 2016). For the flat cosmology of IllustrisTNG, the total energy density is $\Omega_0 = \Omega_{\Lambda,0} + \Omega_{m,0} + \Omega_{r,0} = 1$. Values for each of these energy density parameters and the Hubble constant are consistent with those from the Planck Collaboration et al. (2016) results.

The mass history parameters that are used to describe the accretion histories of halos in this work are z_{50}, z_{75} and z_{90}. These parameters represent the redshifts z_x at which each halo crossed the threshold of $x\%$ of its final mass. More precisely, the redshift z_x is taken to be the redshift of the simulation snapshot after which a halo crossed the mass threshold x. In the case of non-monotonic mass accretion histories, z_x is the lowest-redshift crossing of the mass threshold x. Among the mass history parameters z_{50}, z_{75} and z_{90}, we find that z_{75} consistently presents the best correlations with most structural parameters described in Section 2.3. As a result, most mass histories in this work are parametrised using z_{75}.

2.6 Lensing Profiles

Gravitational lensing is the attraction or bending of light by matter (Wambsganss, 1998). The angle over which light bends around a gravitational lens is proportional to the mass along its trajectory to the observer. As a result, the distortion of light from distant sources

can be used to determine the mass of foreground objects. In particular, we focus on how weak gravitational lensing is used to map the mass distribution of galaxy clusters. Weak gravitational lensing is the distortion of the shapes of background galaxies around foreground galaxies and clusters that cannot be measured from individual objects, but must rather be detected statistically (Wambsganss, 1998). By averaging the shapes of many background galaxies around a massive lens, or around stacked images of lenses, we can detect the coherent distortion of the shapes of the background galaxies due to the gravitational influence of the lens. This map of shape distortions, which depends on the mass distribution of the lens, allows us to map the mass and density profiles of clusters.

The lensing signal determined from weak gravitational lensing as a function of radius around the centre of a cluster $\Delta\Sigma(R)$ is defined as:

$$\Delta\Sigma(R) = \overline{\Sigma}(R) - \Sigma(R) \tag{2.15}$$

where $\Sigma(R)$ is the surface mass density at some radius R, and $\overline{\Sigma}(R)$ is the radially weighted average surface mass density within radius R (Renneby et al., 2020; Mpetha et al., 2025). From cosmological simulation data, we can compute $\Sigma(R)$ for a given cluster by summing the masses of particles projected along the line of sight within an annulus around R and dividing by the area of the annulus. This is represented mathematically by:

$$\Sigma(R) = \frac{\sum_i^N m_i}{\pi\left(r_{\rm max}^2 - r_{\rm min}^2\right)}\,, \tag{2.16}$$

where m_i are the masses of the N particles within $r_{\rm max}$ and $r_{\rm min}$. The radii $r_{\rm max} = R + \frac{1}{2}\Delta r$ and $r_{\rm min} = R - \frac{1}{2}\Delta r$ are the boundaries of the annulus with radius Δr. As given in Mpetha et al. (2025), the weighted average surface mass density $\overline{\Sigma}(R)$ within radius R can then be computed by radially integrating the surface mass densities $\Sigma(R)$ as follows:

$$\overline{\Sigma}(R) = \frac{2}{R^2}\int_0^R R'\Sigma(R')\,dR'\,. \tag{2.17}$$

When computed numerically from the simulation data in this work, the radial annuli for $\Sigma(R)$ as described in Equation 2.16 are logarithmically spaced. As such, the bins cannot be consistently spaced down to $R = 0$. The surface mass density within a circle inside the innermost annulus is used to ensure that all of the cluster's mass is included in the calculation. Since the expression for $\overline{\Sigma}(R)$ given in Equation 2.17 is integrated numerically, it is sensitive to the choice of the innermost annulus' radius. This effect is illustrated in Figure 2.9. Each curve in Figure 2.9 represents the mean gravitational

lensing profile around the same sample of massive clusters in the TNG300-1 simulation, each with a different innermost annulus radius used for its computation. We see that the inner portions of the $\Delta\Sigma(R)$ profile change as we adjust the innermost radius, but that the lensing profiles converge at higher radii. The bumps in the inner profiles in Figure 2.9 reflect the baryonic matter in the BCG. In order to accurately and consistently characterise the lensing around clusters, all results in this work compute the lensing profiles from an innermost radius around the most bound particle of $R = 1\,\mathrm{ckpc}$, and the profiles are then truncated at $R = 50\,\mathrm{ckpc}$.

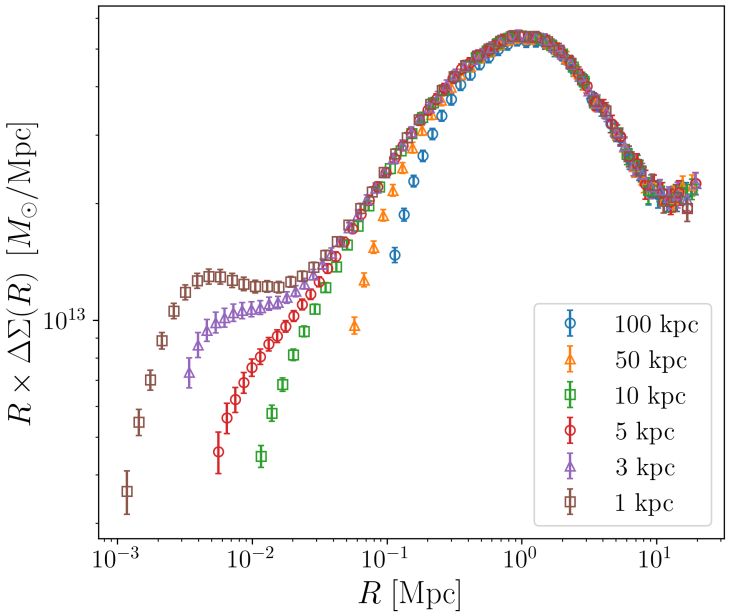


Figure 2.9: The gravitational lensing profiles $\Delta\Sigma$ computed with different innermost radial bins for clusters with mass $M_{500c} \geq 1 \times 10^{14}\,M_\odot$ at redshift $z = 0$ in the TNG300-1 simulation. The labels for each data set indicate the radius around the most bound particle of the innermost bin edge used to compute the lensing profiles. The data points are the mean lensing signal for the clusters, and the error bars are the uncertainty on the mean.

While $\Delta\Sigma(R)$ lensing signals are usually detected gravitationally via weak lensing, we use Equations 2.15, 2.16 and 2.17 in this work to numerically compute them directly from the simulated mass distributions of halos in the TNG300-1 simulation. Given the full-volume particle data for the TNG300-1 simulation described in Section 2.2, we compute the $\Delta\Sigma(R)$ lensing profiles around the most bound particle of each massive halo in the simulation box. Lensing profiles are computed from a cylinder of particles with a 20 cMpc

radius tangent to the z-axis and ± 20 cMpc along the z-axis around the most bound particle. We found that the lensing profiles were not significantly altered with greater line of sight depths along the z-axis. Given the individual profiles around halos, we can compute the mean lensing profiles of any defined group of clusters. This is done in Chapter 4 to compare the structure of different cluster samples.

Chapter 3

Structure and Growth History

In this chapter, we examine the correlations of structural measurements defined in Section 2.3 with the mass histories of halos as described in Section 2.5. This enables us to determine what observable properties of halos are effective indicators of the age and dynamical state of galaxy clusters, thus addressing our motivation to probe the formation histories of large structures in the universe.

3.1 Centre of Mass Offset

The centre of mass offset of a galaxy cluster is the distance between the centre of mass of the halo and the most bound particle, which generally resides at the point of greatest density in the BCG. We expect centre of mass offset to be correlated with recent mass accretion through major mergers because material falling into a halo should pull the centre of mass away from the most bound particle and toward the infalling mass. Systems with large centre of mass offsets should thus be young and dynamically unrelaxed. Conversely, systems with small centre of mass offsets should have a deficit of infalling material and symmetric mass distributions, which enables the centre of mass to settle toward the most bound particle in the centre of the halo. Systems with small centre of mass offsets are thus expected to be old and dynamically relaxed systems.

As an initial indication of how well 3D centre of mass offset correlates with recent mass accretion history, we compare it to the mass history parameter z_{75} for halos at redshift $z = 0$ in Figure 3.1. It is clear from the distribution of offsets and z_{75} that the two parameters are well correlated. We also see that systems with large offsets are almost exclusively

systems with low z_{75}, indicating that they have experienced recent mergers. However, it is notable that not all systems with low z_{75} have large offsets. This is likely due to the oscillation of the centre of mass offset during mergers. An infalling group repeatedly crosses through the centre of a halo and out the other side as the system gradually relaxes. This causes the centre of mass offset to oscillate with the phase of the infall. As a result, while systems with large offsets are generally experiencing mergers, systems experiencing mergers do not necessarily have large offsets. As reflected in the distribution in Figure 3.1, this suggests that splitting a halo sample based on 3D centre of mass offset would produce a sample of young, dynamically unrelaxed clusters with low contamination but also with low completeness.

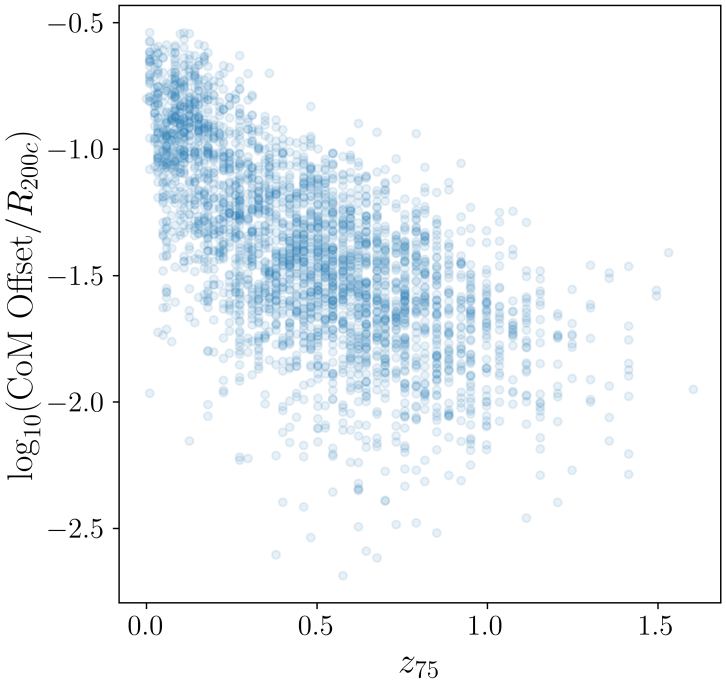


Figure 3.1: The 3D centre of mass offsets plotted against the z_{75} mass history for halos with masses $1\times10^{13} < M_{200c}/M_{\odot} < 5\times10^{13}$ at redshift $z = 0$ in the TNG300-1 simulation. Centre of mass offsets are computed from particles with R_{200c} in 3D around the most bound particle. The z_{75} parameter is computed from M_{200c} of the main progenitor.

To better understand the distribution of 3D centre of mass offsets against z_{75} mass accretion history, we plot a heat map of the values in the left panel of Figure 3.2. The heat map was constructed by applying a Gaussian smoothing kernel to the distribution in

Figure 3.1. We see from the heat map that there are two distinct peaks in the distribution representing two populations of halos. There is a population of halos with recent mass accretion and large centre of mass offsets, as well as a population without recent mass accretion and with small offsets. There is a fainter peak between these two distributions as well, though it is less pronounced than the other two. The relative deficit of intermediate-age halos could be an artefact of our definition of z_{75}, or it could reflect different physical formation channels for halos. In either case, characterizing the two prominent populations of halos in Figure 3.2 can grant insight into the properties and mass accretion histories of halos with different physical structures.

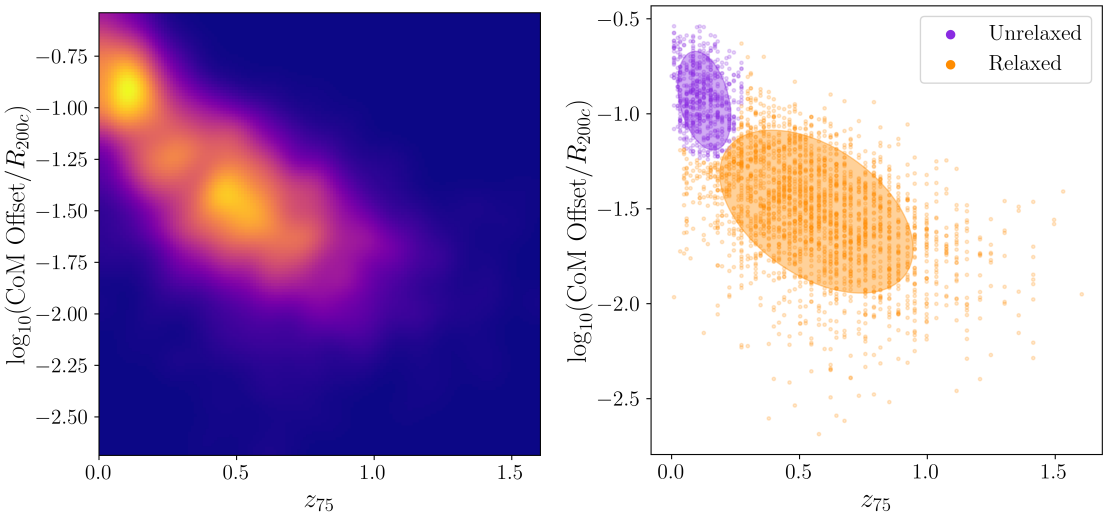


Figure 3.2: The 3D centre of mass offsets plotted against the z_{75} mass history for halos with masses $1 \times 10^{13} < M_{200c}/M_{\odot} < 5 \times 10^{13}$ at redshift $z = 0$ in the TNG300-1 simulation. The left panel is a heat map of the distribution with a Gaussian smoothing applied. The right panel splits the distribution into groups using a 2-component Gaussian mixture model. The shaded regions in the right panel are the 1σ boundaries for the Gaussian fit components, and the colours of the dots represent the group membership of the halos. Centre of mass offsets are computed from particles with R_{200c} in 3D around the most bound particle. The z_{75} parameter is computed from M_{200c} of the main progenitor.

To characterise the two populations of halos identifiable by eye in the left panel of Figure 3.2, we applied a Gaussian mixture model to the distribution. In this context, a Gaussian mixture model is a fit of several Gaussian distributions to some data set where we assume that each point is randomly drawn from the mixture of those Gaussians. By fitting a two-component Gaussian mixture model to the distribution of 3D halo centre of

mass offsets and z_{75}, we can split the halos into two groups – relaxed and unrelaxed – based on their structure and mass accretion history. We used the Gaussian mixture model algorithm from the "scikit-learn" Python package[1]. This algorithm is stochastic, so we used many iterations and initialisations in order to get reliable results and verify that they are robust. In the right panel of Figure 3.2, a Gaussian mixture model is applied to the offset and z_{75} distribution. We see that the model does indeed pick out the two groups that were identified by eye. There is a group of halos with large centre of mass offsets and very recent mass accretion, and there is a distribution of halos with a broader range of small offsets and gradual mass accretion.

To more comprehensively compare the mass accretion histories of the halos split into groups based on 3D centre of mass offset and z_{75}, we plot the median normalised mass accretion histories of the two groups as a function of redshift in Figure 3.3. We see that the median mass accretion histories of the relaxed and unrelaxed groups as defined by the Gaussian mixture model differ significantly at low redshift. The thin shaded regions that represent the uncertainty on the median accretion history are extremely well separated. The large shaded regions representing the 1σ scatter in the mass accretion histories are also well separated at low redshift, indicating a statistically significant difference in the mass accretion histories. The relaxed sample experiences gradual mass increase with very little recent accretion, whereas the unrelaxed group experiences slow mass accretion at higher redshift, followed by sudden accretion at low redshift. This behaviour for the disturbed systems is consistent with recent major mergers.

Given that a two-component Gaussian mixture model fit to the centre of mass offset and z_{75} mass histories of halos produced groups with very different mass histories, we investigate whether the distribution is better fit by more Gaussian components. Given the peak in the heat map in the left panel of Figure 3.2 that is not captured in the two-component mixture model in the right panel, there may be justification for a third population of halos between the relaxed and unrelaxed groups. In Figure 3.4, we use the same Gaussian mixture model fitting procedure to define more groups of halos. We see in the left panel of Figure 3.4 that using a three-component mixture model does not capture the three peaks in the distribution identified by eye. Rather, it splits the previously defined relaxed group into two different populations. In the right panel, a four-component mixture model splits the distribution of halos into unintuitive groups along the axis of the correlation between centre of mass offset and z_{75}. There is also significant overlap in some of the 1σ contours in the three- and four-component models, suggesting that they do not split the population as distinctly as a two-component model.

[1]https://scikit-learn.org/stable/

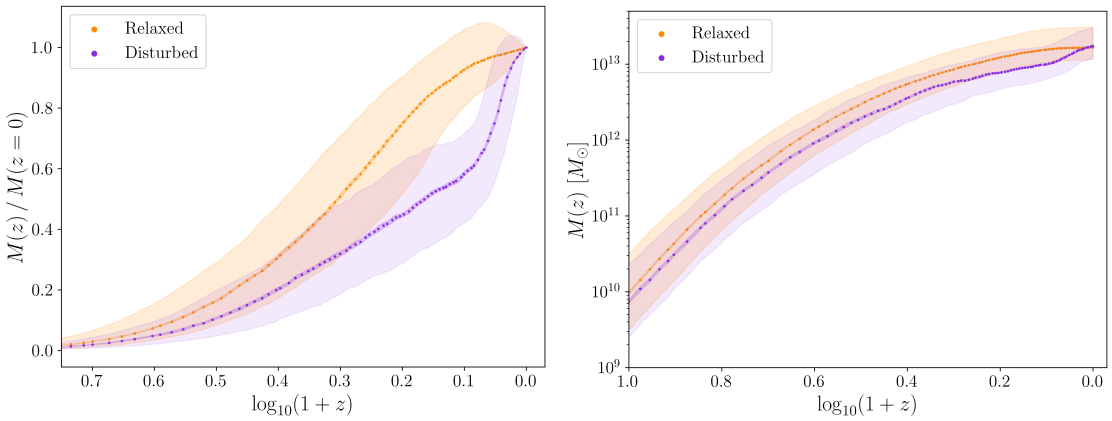


Figure 3.3: The median mass evolution histories within R_{200c} of relaxed and unrelaxed $1 \times 10^{13} < M_{200c}/M_\odot < 5 \times 10^{13}$ halos at redshift $z = 0$ in the TNG300-1 simulation. The relaxed and unrelaxed groups were selected using the Gaussian mixture model in Figure 3.2. The mass accretion histories for each halo in the left panel are normalised to their masses at $z = 0$, while those in the right panel are not. The points represent the median masses of halos in each group at the available snapshots. The thin shaded regions around the points are the errors on the medians computed via bootstrap. The large shaded regions around the points are the 1σ variations around the medians.

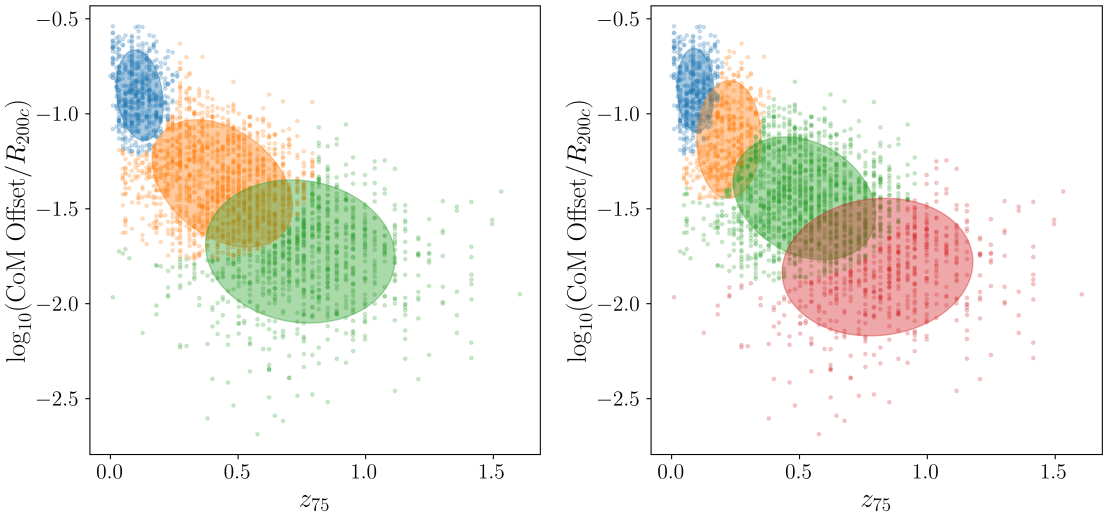


Figure 3.4: Halos with masses $1 \times 10^{13} < M_{200c}/M_{\odot} < 5 \times 10^{13}$ at redshift $z = 0$ in the TNG300-1 simulation are split into groups using Gaussian mixture models with varying numbers of components. The shaded regions in the right panel are the 1σ boundaries for the Gaussian fit components, and the colours of the dots represent the group membership of the halos. The models are fit to the 3D centre of mass offsets and z_{75} mass histories of the halos. The left panel shows the groups for a 3-component mixture model, while the right panel shows the same for a 4-component mixture model.

To quantify how well these multi-component Gaussian mixture models fit the data without over-fitting, we employ the Akaike information criterion (AIC) and the Bayesian information criterion (BIC). Each of these criteria is a numerical value that represents the goodness of fit of a model to a data set, while preferring models with fewer free parameters. The formula for the AIC A given in Akaike (1974) and that for the BIC B given in Schwarz (1978) are:

$$A = 2k - 2\ln(\hat{L}) \quad ; \quad B = k\ln(n) - 2\ln(\hat{L})\,, \tag{3.1}$$

where k is the number of free parameters in the model, n is the number of samples in the data set, and $\hat{L}$ is the likelihood function. The minimum value of these functions is meant to indicate the best fit for the data, weighted by the number of free parameters. We see that both criteria seek to maximise the likelihood of the fit $\hat{L}$ while punishing a greater number of free parameters k. The primary difference between the two criteria is that the BIC more heavily punishes a greater number of free parameters for data sets with more samples n. The values for both the AIC and BIC are output directly from the Gaussian mixture model fit by the "scikit-learn" package.

Figure 3.5 shows the values of both information criteria for our sample from Figure 3.1 as a function of the number of Gaussian mixture model components. We see in Figure 3.5 that the AIC decreases consistently as a function of the number of Gaussian components. Meanwhile, the BIC has a minimum at 4 components. If we compute the same information criteria for randomly selected halves of our data set, the AIC shows the same behaviour, while the minimum for the BIC changes between 3–5 components, depending on the sample. Both the continued decrease of the AIC and the minimum of the BIC suggest that the distribution of 3D halo centre of mass offsets and z_{75} mass histories is best fit by more than two Gaussian components. However, while both information criteria decrease dramatically from one to two Gaussian components, they only decrease marginally for greater numbers of components. This suggests that there is strong motivation for two groups of halos in the distribution and weak evidence for the inclusion of more components. The facts that no minimum in the AIC is reached for a reasonable number of Gaussian components and that the minimum in the BIC is unstable based on sample selection suggest that the slight preference for more components is due to the sample not being consistent with populations randomly drawn from Gaussian distributions. As such, we conclude that it is appropriate to split our halo sample into only two groups – relaxed and unrelaxed – but that Gaussian mixture models are not ideal for grouping in this distribution.

We have found that halos categorised as relaxed or unrelaxed based on 3D centre of mass offsets and z_{75} mass histories produce notably different samples, and that there is evidence for two classes of halos based on these two parameters. However, this halo categorisation requires a measurement of z_{75}, which is not observationally attainable for real systems.

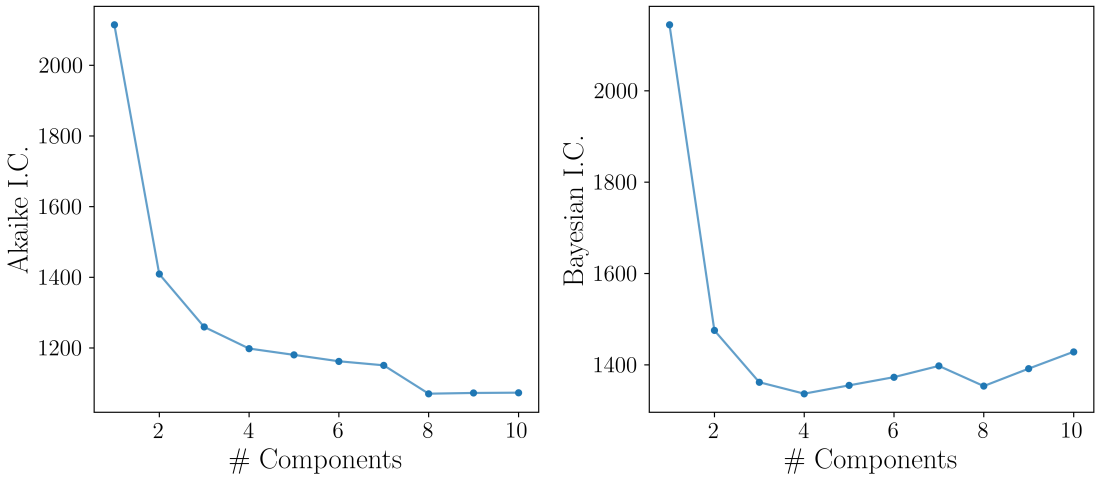


Figure 3.5: The BIC and AIC for Gaussian mixture models fit to the 3D centre of mass offset and z_{75} mass history distribution, plotted against the number of model components. The models were fit to halos with masses $1 \times 10^{13} < M_{200c}/M_{\odot} < 5 \times 10^{13}$ at redshift $z = 0$ in the TNG300-1 simulation.

In Figure 3.6, we use a one-dimensional Gaussian mixture model to categorise halos as relaxed and unrelaxed based only on 3D centre of mass offset with no explicit mass history information. We see in the left panel of Figure 3.6 that the Gaussian mixture model picks out a broad population of halos with small offsets as the relaxed group and a smaller population of halos with large offsets as the unrelaxed group. Though the sum of the two Gaussian distributions fits the centre of mass distributions of the halos quite well, we see significant overlap between the two Gaussian groups fit by the model. This suggests that any cut in centre of mass offsets that separates relaxed and unrelaxed halos is likely to have significant contamination between the groups. We choose to split the halos based on the probability of membership to each group as determined by the Gaussian mixture model. The transition point between the groups is reflected in the left panel of Figure 3.6 as the intersection of the two Gaussian curves. In the right panel of Figure 3.6, we plot the median mass accretion histories of these two groups. While the difference between the median mass accretion histories is not as large as in Figure 3.3 where we fit the Gaussian mixture model to z_{75}, we still see a significant difference between the histories of the two groups. The dynamically relaxed halos accrete their mass gradually with less accretion at low redshift, while the unrelaxed halos have sudden low-redshift accretion consistent with recent mergers. The median mass histories are very different at low redshift compared to their uncertainties, and the 1σ scatter in the accretion histories of each group do not quite

overlap at the point of maximum separation.

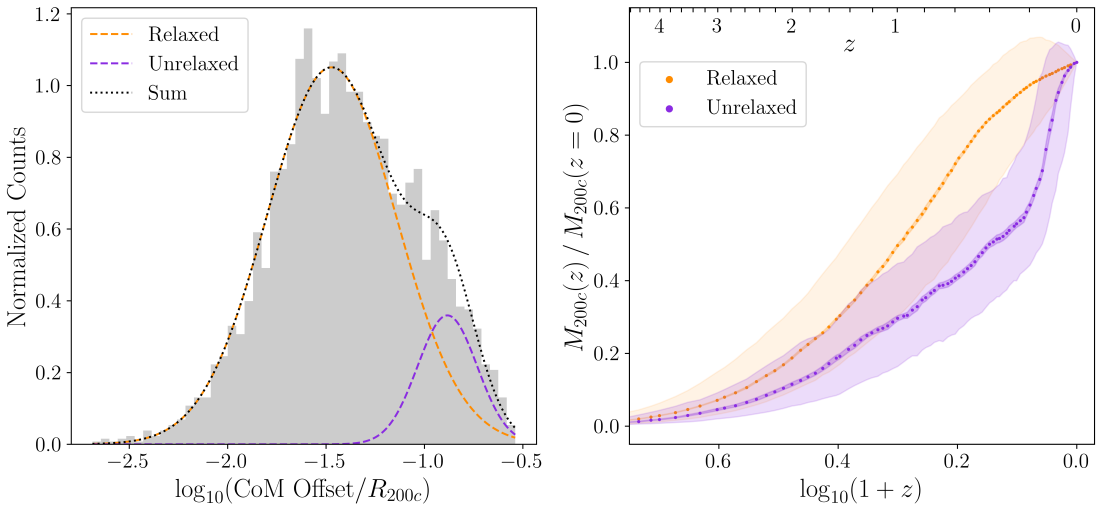


Figure 3.6: The 3D centre of mass offsets and median mass accretion histories for halos with masses $1\times10^{13} < M_{200c}/M_{\odot} < 5\times10^{13}$ at redshift $z = 0$ in the TNG300-1 simulation. The left panel is the distribution of offsets fit with a 2-component, 1D Gaussian mixture model splitting the sample into relaxed and unrelaxed groups. In the right panel, the points represent the median masses of halos in each group at the available snapshots. The thin shaded regions around the points are the errors on the medians computed via bootstrap. The large shaded regions around the points are the 1σ variations around the medians.

Given our success in identifying systems with different recent mass accretion histories based solely on 3D centre of mass offset, we now investigate how well the method performs when using projected offsets. While we have access to three-dimensional information in simulations, precise line of sight distances within clusters are generally not available in real observed systems. Centre of mass offsets computed from the projected surface mass distribution of a cluster are thus more applicable to real clusters. In Figure 3.7, we apply the same Gaussian mixture model procedure as was applied to the 3D offsets to the distribution of projected centre of mass offsets. We see in the left panel of Figure 3.7 that the distribution of projected offsets is nearly Gaussian. This causes the mixture model to fit nearly all of the halos with a single Gaussian component, while the second component only describes few very low-offset halos. As a result, the mass accretion history of the relaxed group in the right panel of Figure 3.7 does not carry meaningful information, while the history of the unrelaxed group is the median for nearly all of the halos in the target mass range.

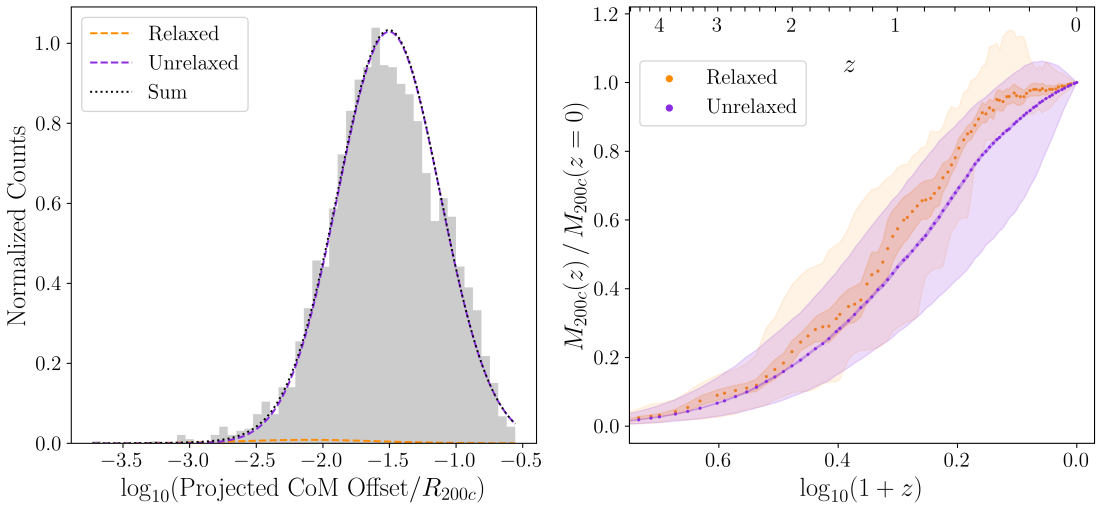


Figure 3.7: The z-axis projected 2D centre of mass offsets and median mass accretion histories for halos with masses $1 \times 10^{13} < M_{200c}/M_{\odot} < 5 \times 10^{13}$ at redshift $z = 0$ in the TNG300-1 simulation. The left panel is the distribution of offsets fit with a 2-component, 1D Gaussian mixture model splitting the sample into relaxed and unrelaxed groups. In the right panel, the points represent the median masses of halos in each group at the available snapshots. The thin shaded regions around the points are the errors on the medians computed via bootstrap. The large shaded regions around the points are the 1σ variations around the medians.

Given the failure of the Gaussian mixture model to split a halo sample into two groups based solely on projected centre of mass offset, we look to other methods of determining an optimal split in projected offset in order to distinguish relaxed and unrelaxed groups of halos. Since we are motivated to maximise the difference in the recent mass accretion histories of groups of halos, we can use the difference in median mass accretion histories to measure the effectiveness of a split in projected centre of mass offset. To achieve this, we split halos into groups over a range of projected centre of mass offsets and evaluate the differences between the median mass accretion histories of the groups as a function of offset split. The differences between mass histories are quantified using a χ^2 statistic whose form is given in, e.g., Hristova & Wimley (2023) as:

$$\chi^2 = \sum_i^N \frac{(m_{r,i} - m_{d,i})^2}{\sigma_{r,i}^2 + \sigma_{d,i}^2}, \tag{3.2}$$

where, for our application, $m_{r,i}$ and $m_{d,i}$ are the median normalised masses of the dynamically relaxed and disturbed populations at redshift i, and where $\sigma_{r,i}$ and $\sigma_{d,i}$ are the uncertainties on the median normalised mass histories of the relaxed and disturbed populations at redshift i. The split in the projected centre of mass offset that maximises this χ^2 statistic maximises the difference in mass accretion histories of the subsamples. In the left panel of Figure 3.8, we see that the projected centre of mass offset that produces the maximal difference in mass accretion histories is $\log_{10}(\text{Offset Split}/R_{200c}) = -1.07$. In the right panel of Figure 3.8, we present the median normalised mass accretion histories of the two groups split at this offset. The relaxed halos are those with smaller projected offsets, and the unrelaxed halos are those with greater projected offsets. The difference between the mass accretion histories of the two groups is slightly less statistically significant than in the case of the 3D offsets presented in Figure 3.6. However, we've clearly separated halos based on whether they experienced recent major mergers from this split in projected centre of mass offset. Despite the overlap in 1σ scatter about the median for the two groups, the median mass histories are very distinctly different relative to their uncertainties.

The centre of mass offsets investigated thus far have been based on the total mass distribution of halos. Due to the mass of any cluster being dominated by dark matter, which is not directly observable, the mass distributions for individual real clusters are difficult to map accurately. As a result, we need an observationally accessible proxy for the centre of mass offset in order to leverage the mass history information that it carries. We propose a new structural measurement called the galaxy offset, which is the distance between the centre of the BCG and the centre of stellar mass of the galaxies in a cluster. The BCG of a halo is defined here as the subhalo with the greatest stellar mass. The centre of stellar mass was computed using Equation 2.1, where m_i is the stellar mass of subhalo

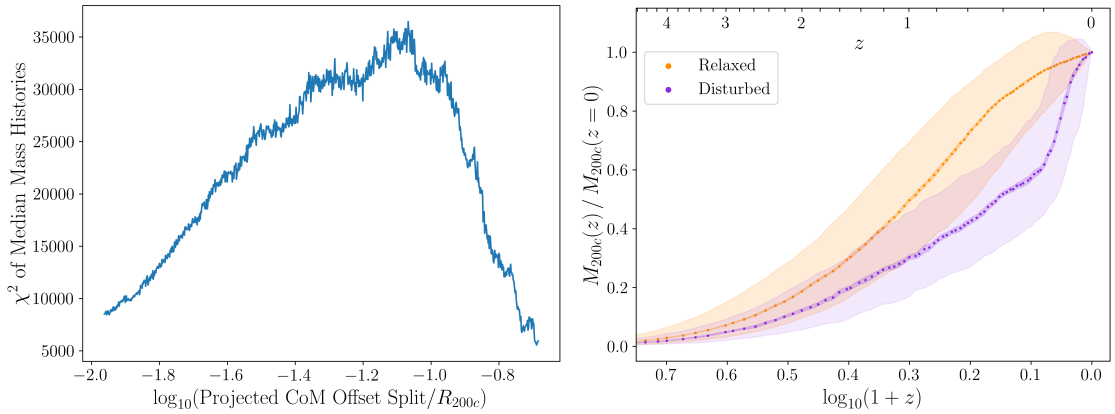


Figure 3.8: The left panel shows the χ^2 difference between the median mass accretion histories of the relaxed and unrelaxed groups as a function of the split in z-axis projected centre of mass offsets for halos with masses $1 \times 10^{13} < M_{200c}/M_{\odot} < 5 \times 10^{13}$ at redshift $z = 0$ in the TNG300-1 simulation. The right panel shows the median mass accretion histories at the optimal split of $\log_{10}(\text{Offset Split}/R_{200c}) = -1.07$, which maximises χ^2. In the right panel, the points represent the median masses of halos in each group at the available snapshots. The thin shaded regions around the points are the errors on the medians computed via bootstrap. The large shaded regions around the points are the 1σ variations around the medians.

i and x_i is the position of its most bound particle relative to that of the BCG. In order to ensure that galaxy offsets are a maximally observable quantity, we select member galaxies for each cluster based on their velocity along the z-axis relative to that of the BCG, as described in Section 2.4.

Having defined galaxy offsets as observationally practical proxies for true projected centre of mass offset, we investigate the correlation between galaxy offset and mass accretion history. In Figure 3.9, we plot the distribution of galaxy offsets and the z_{75} mass history parameter for group mass halos at redshift $z = 0$. The galaxy offsets were computed from galaxies within a radius of 0.5 Mpc tangent to the z-axis. This threshold was chosen since offsets within larger radii produced poorer correlations with mass accretion history, and since offsets within smaller radii saw little improvement in the correlations with mass history. Though Figure 3.9 does present a correlation between galaxy offset and z_{75}, it is not as strong as that between 3D centre of mass offset and z_{75} as seen in Figure 3.1. There is also a lot of scatter in the distribution, which would likely reduce the effectiveness of splits in galaxy offset to produce different median mass accretion histories.

In Figure 3.10, we apply a two-component Gaussian mixture model to the distribution of galaxy offsets and z_{75} to characterise relaxed and unrelaxed halos. We see in the left panel that the mixture model picks out the dense collection of halos with high galaxy offsets and low z_{75} as the unrelaxed group and the broad diffuse part of the distribution as the relaxed halos. In the right panel of Figure 3.10, we see that the median mass accretion histories of these two groups are distinctly different, with the unrelaxed population's median mass accretion histories again being consistent with recent mergers. We note that the difference between the median mass accretion histories for the projected galaxy offsets is approximately as statistically significant as for the 3D centre of mass offsets in Figure 3.3.

In order to determine whether galaxy offsets can be used to identify systems with different recent mass accretion histories without the inclusion of unobservable parameters like z_{75}, we apply similar techniques to the galaxy offset distribution as we applied to the centre of mass offsets of halos. In Figure 3.11, we apply both a one-dimensional Gaussian mixture model and a χ^2 statistic to split the halo sample based on galaxy offset. In the top left panel of Figure 3.11, we see that the galaxy offset distribution is different from those that we've seen for centre of mass offsets. Rather than being nearly Gaussian and having a small bump at high offsets, the galaxy offset distribution has a large tail at low offset. The Gaussian mixture model thus takes the low-offset tail of the distribution to be relaxed halos and the majority of the distribution to be unrelaxed. The resulting mass accretion histories of the groups in the top right panel of Figure 3.11 are not well separated. Though the unrelaxed population of halos did accumulate its mass more recently than the relaxed population, we do not see the jump in median mass at low redshift that is characteristic

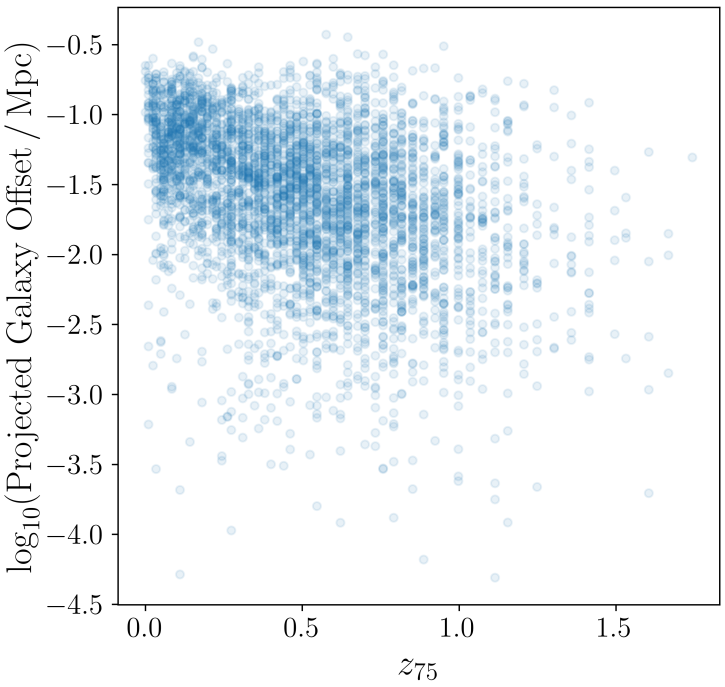


Figure 3.9: The z-axis projected galaxy offsets plotted against the z_{75} mass history for halos with masses $1 \times 10^{13} < M_{200c}/M_{\odot} < 5 \times 10^{13}$ at redshift $z = 0$ in the TNG300-1 simulation. Galaxy offsets are computed from stellar particles in galaxies within a 0.5 Mpc radius tangent to the z-axis and $\pm$1000 km/s along the z-axis around the most bound particle. The z_{75} parameter is computed from M_{200c} of the main halo progenitor.

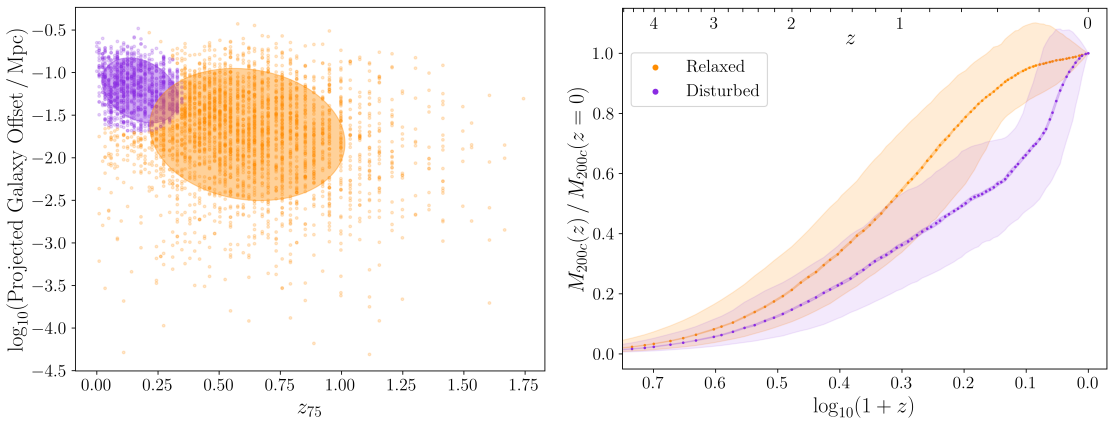


Figure 3.10: The z-axis projected galaxy offsets and median mass accretion histories for halos with masses $1 \times 10^{13} < M_{200c}/M_{\odot} < 5 \times 10^{13}$ at redshift $z = 0$ in the TNG300-1 simulation. The left panel splits the distribution into groups using a 2-component, 2D Gaussian mixture model with the z_{75} mass history. The shaded regions in the right panel are the 1σ boundaries for the Gaussian fit components, and the colours of the dots represent the group membership of the halos. In the right panel, the points represent the median masses of halos in each group at the available snapshots. The thin shaded regions around the points are the errors on the medians computed via bootstrap. The large shaded regions around the points are the 1σ variations around the medians.

of recent major mergers. In addition, the median mass accretion histories of each group are well within the 1σ scatter of the other group. In the bottom left panel of Figure 3.11, we plot the χ^2 difference between the mass accretion histories of the groups as a function of galaxy offset. In contrast to Figure 3.8, these χ^2 values were computed based on the median z_{75} statistic rather than over the entire mass accretion histories. This was done to reduce computational time since computing the uncertainty on the median mass accretion histories via bootstrap is very slow. While this statistic carries less information than the entire mass accretion histories of the halos, it was only found to be slightly less effective at determining the optimal split based on offsets. From the bottom right panel of Figure 3.8, we see that the optimal split in galaxy offset based on the χ^2 difference in mass accretion histories does not produce median mass histories with the desired characteristics. The difference between groups is not as statistically significant as in the projected centre of mass offset case, and systems with recent major mergers are not properly identified.

As a final attempt to use the observationally accessible galaxy offsets in order to distinguish dynamically relaxed and unrelaxed clusters, we compare the median mass accretion histories of halos with the largest and smallest galaxy offsets, while omitting the majority of systems with moderate offsets. In the top panels of Figure 3.12, we group the 20% of halos with the smallest galaxy offsets and the 20% of halos with the greatest galaxy offsets into relaxed and unrelaxed groups. In the bottom panel, we compare the median mass accretion histories of those two samples. We see that the mass accretion histories are extremely similar for the two groups and are in fact less well separated than by the one-dimensional Gaussian mixture model or optimal χ^2 split in Figure 3.11. This poor separation of the median mass accretion histories despite taking the most extreme systems may be due to the largest galaxy offsets being the result of projection effects from galaxies outside of the cluster rather than being the result of recent mergers.

Given our inability to reliably identify halos that have experienced recent growth from galaxy offsets, we conclude that this observationally accessible structural measurement is not an effective indicator of halo mass history. Though centre of mass offsets offer better discrimination between dynamically relaxed and unrelaxed systems, the detailed mass distributions of individual galaxy clusters are not easily observable. As a result, projected centre of mass offset is not an ideal indicator of halo mass history either.

3.2 Axis Ratio

The axis ratio of a halo describes the asymmetrical elongation of the mass distribution of the halo. See Section 2.3.2 for a more detailed description of the measurement. We

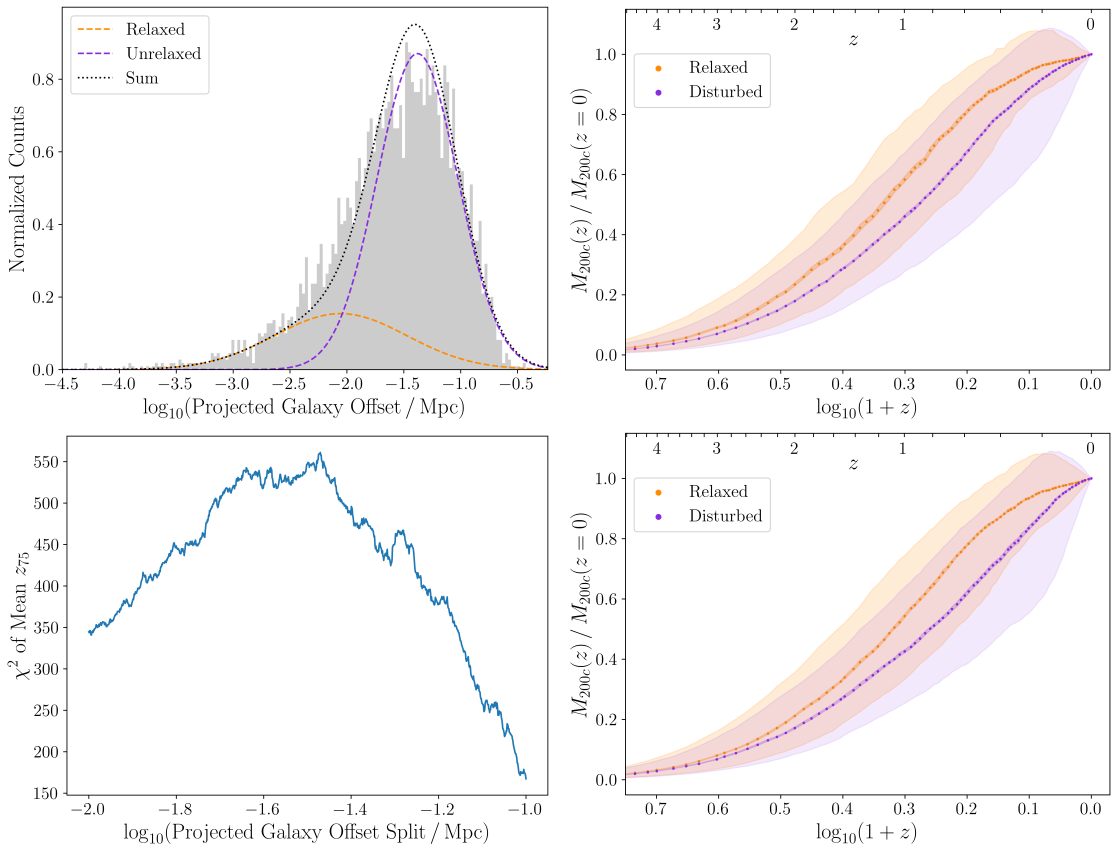


Figure 3.11: The z-axis projected galaxy offsets and median mass accretion histories for halos with masses $1 \times 10^{13} < M_{200c}/M_{\odot} < 5 \times 10^{13}$ at redshift $z = 0$ in the TNG300-1 simulation. The top left panel is the distribution of offsets fit with a 2-component, 1D Gaussian mixture model. The bottom left panel shows the χ^2 difference between the median z_{75} of the relaxed and unrelaxed groups as a function of the split in galaxy offset. The peak of this curve is taken to be the optimal split. The right panels show the mass accretion histories for the groups defined on their left. The points represent the median masses of halos in each group at the available snapshots. The thin shaded regions around the points are the errors on the medians computed via bootstrap. The large shaded regions around the points are the 1σ variations around the medians.

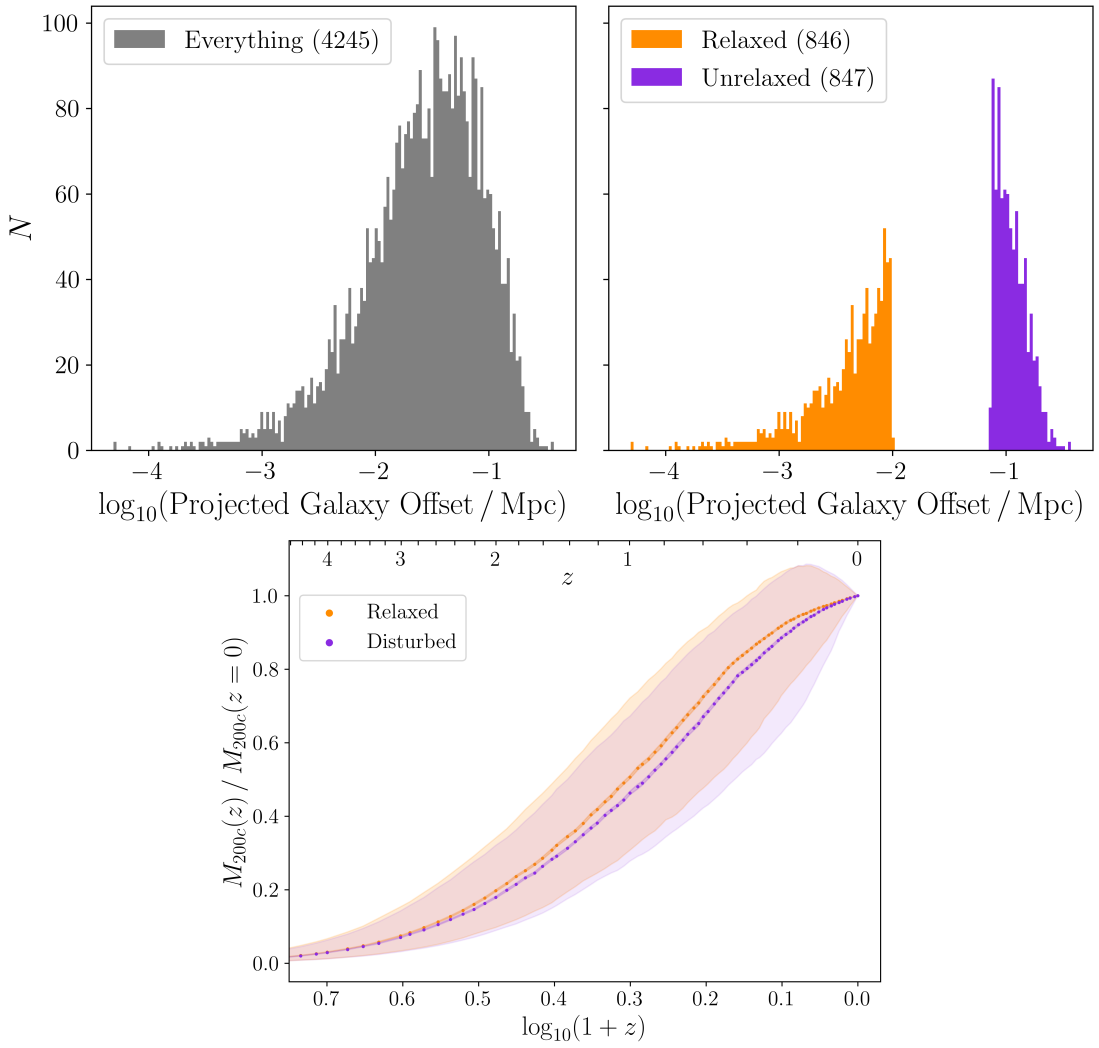


Figure 3.12: The z-axis projected galaxy offsets and median mass accretion histories for halos with masses $1 \times 10^{13} < M_{200c}/M_{\odot} < 5 \times 10^{13}$ at redshift $z = 0$ in the TNG300-1 simulation. The top left panel is the full distribution of projected galaxy offsets, and the top right panel splits the top and bottom 20% of halos into relaxed and unrelaxed groups based on this distribution. In the bottom panel, the points represent the median masses of halos in each group at the available snapshots. The thin shaded regions around the points are the errors on the medians computed via bootstrap. The large shaded regions around the points are the 1σ variations around the medians.

expect the axis ratio to be correlated with recent mass accretion through mergers since the infalling material would distort the shape of the halo. As a result, systems with axis ratios much smaller than unity should be young and dynamically unrelaxed. Conversely, systems with axis ratios near unity are more spherical, indicating that they have a deficit of infalling material. Such halos are thus expected to be old and dynamically relaxed systems.

As an initial indication of how well axis ratio correlates with recent mass accretion history, we compare it to the mass history parameter z_{75} for halos at redshift $z = 0$ in Figure 3.13. We see from the figure that axis ratio and z_{75} are generally not very well correlated. There is a slight trend that systems with larger axis ratios have less recent mass accretion, but there is a great amount of scatter in the relationship. However, in the bottom left of Figure 3.13, there is a notable population of halos with very small axis ratios that are almost uniquely young systems with low z_{75}. This suggests that axis ratio could be used to select a small sample of young halos with little contamination but also with low completeness, given that most young halos have indistinguishable axis ratios from the rest of the distribution.

To determine how well axis ratios could be used to distinguish between halos with different mass accretion histories, we compare it to centre of mass offset in terms of how well it traces z_{75}. In Figure 3.14, we present the three-dimensional distribution of axis ratios, centre of mass offsets, and z_{75} for group-mass halos. We see in the left panel of Figure 3.14 that while axis ratio is weakly correlated with z_{75}, there is a clear colour gradient along the z_{75} axis, which represents how well centre of mass offset traces recent mass history. This finding is consistent with a comparison of Figures 3.1 and 3.13, where we see that centre of mass offset is more clearly correlated with z_{75} than axis ratio is. In the right panel of Figure 3.14, we fit a three-dimensional Gaussian mixture model to the distribution of axis ratios, centre of mass offsets and z_{75}. We see from the 1σ contours of the model and the grouping of the points that very little of the information governing the halo split is carried by the axis ratios. Rather, the split between relaxed and unrelaxed halos is nearly perpendicular to the $s = c/a$ axis. This suggests that splits based on axis ratio are far less effective at predicting recent mass accretion histories than splits in centre of mass offset.

Since precise line of sight information is not generally available in real observed systems, especially for the dark matter mass distributions used to compute axis ratios, we investigate how robust axis ratio measurements are to projection. Note that projected axis ratios are not computed from the projection of the 3D axes but rather from the axes of the projected mass distribution as described in Section 2.3.2. In Figure 3.15, we compare the three-dimensional and projected distributions of axis ratios and centre of mass offsets. In the left panel of the figure, we fit a Gaussian mixture model to the distribution of 3D centre

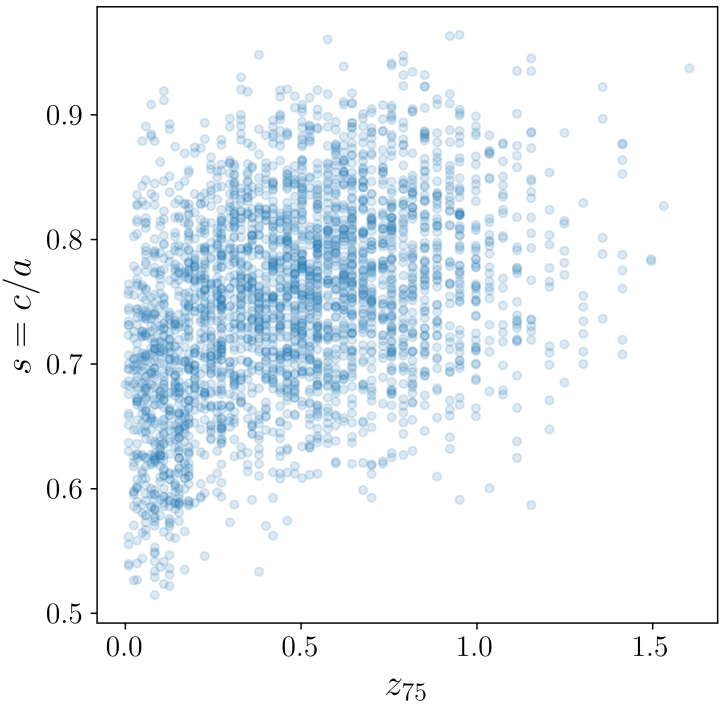


Figure 3.13: The major-to-minor axis ratios $s = c/a$ plotted against the z_{75} mass history for halos with masses $1 \times 10^{13} < M_{200c}/M_{\odot} < 5 \times 10^{13}$ at redshift $z = 0$ in the TNG300-1 simulation. Axis ratios are computed from particles with R_{200c} in 3D around the most bound particle in each halo. The z_{75} parameter is computed from M_{200c} of the main progenitor.

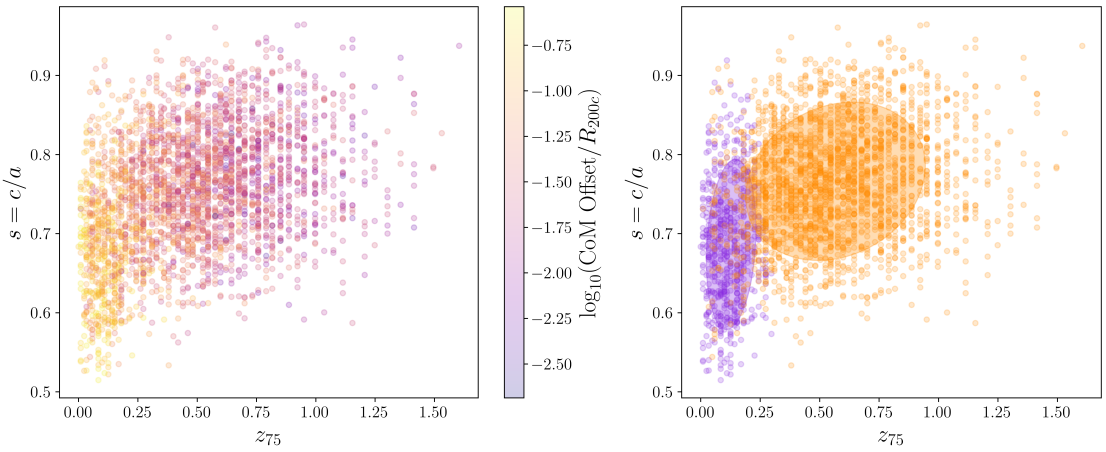


Figure 3.14: The distribution of major-to-minor axis ratios $s = c/a$, z_{75} mass histories, and centre of mass offsets for halos with masses $1 \times 10^{13} < M_{200c}/M_{\odot} < 5 \times 10^{13}$ at redshift $z = 0$ in the TNG300-1 simulation. The centre of mass offsets are shown in colour scale in the left panel and omitted from the right panel. The right panel splits the distribution into groups using a 2-component Gaussian mixture model on the three parameters. The shaded regions in the right panel are the 1σ boundaries for the Gaussian fit components in the dimensions of the two axes, and the colours of the dots represent the group membership of the halos. Axis ratios and centre of mass offsets are computed from particles with R_{200c} in 3D around the most bound particle in each halo. The z_{75} parameter is computed from M_{200c} of the main progenitor.

of mass offsets and minor-to-major axis ratios in order to define relaxed and unrelaxed groups of halos without explicit mass history information. We see that the halos with the greatest centre of mass offsets and smallest axis ratios, which we expect to be dynamically unrelaxed, are grouped together. The halos with larger smaller offsets and axis ratios nearer to unity, which we expect to be relaxed, form the other group. The 1σ contours of our two-component mixture model overlap slightly, indicating that the bimodality in the centre of mass offset and axis ratio distribution is not very pronounced. In the right panel of Figure 3.15, we plot the distribution of projected centre of mass offsets and projected axis ratios along the z-axis, with points coloured based on how the halos were categorised in 3D. We see that the purple unrelaxed points generally maintain their high offsets under projection, but their axis ratios get washed out over a large range. This suggests that axis ratio measurements are less robust to projection than centre of mass offset measurements. This is likely due to the fact that the projected centre of mass offset is simply the projection of the 3D quantity. In contrast, the projected axis ratio is computed from the projected mass distribution, which is significantly different from the projection of the 3D axes, as seen in Figure 2.5.

The axis ratios investigated thus far have been computed from the total mass distributions of halos within R_{200c}. The majority of mass in a cluster is comprised of dark matter, which is not directly observable and is difficult to map accurately for individual systems. We must establish an observationally accessible proxy for the projected axis ratio in order to leverage any mass history information that it may carry. We propose a new structural measurement called the galaxy axis ratio, which is the axis ratio computed from the stellar mass of the galaxies in a cluster around the BCG. The BCG of a halo is defined as the subhalo with the greatest stellar mass. The axis ratio is computed using Equations 2.6 and 2.5, where m_k is the stellar mass of subhalo k and $x_{k,i}$ is the position of its most bound particle relative to that of the BCG. In order to make galaxy axis ratios a maximally observable quantity, we select member galaxies for each cluster based on their velocity along the z-axis relative to that of the BCG, as described in Section 2.4.

In Figure 3.16, we investigate how well the galaxy axis ratio is correlated with the recent mass accretion history z_{75}. As with projected galaxy offsets in Section 3.1, we compute galaxy axis ratios from all subhalos within a 0.5 Mpc radius tangent to the z-axis from the BCG and within $\pm$1000 km/s along the z-axis from the BCG. We see in Figure 3.16 that there is no clear correlation between the two parameters. Additionally, the small population of halos with small axis ratios and low z_{75} seen in Figure 3.13 is not present for galaxy axis ratios in Figure 3.16. We also see that the galaxy axis ratios span nearly the entire possible range from zero to unity, which was not the case for total mass axis ratios. This is due to how galaxies are distributed in halos relative to the total mass

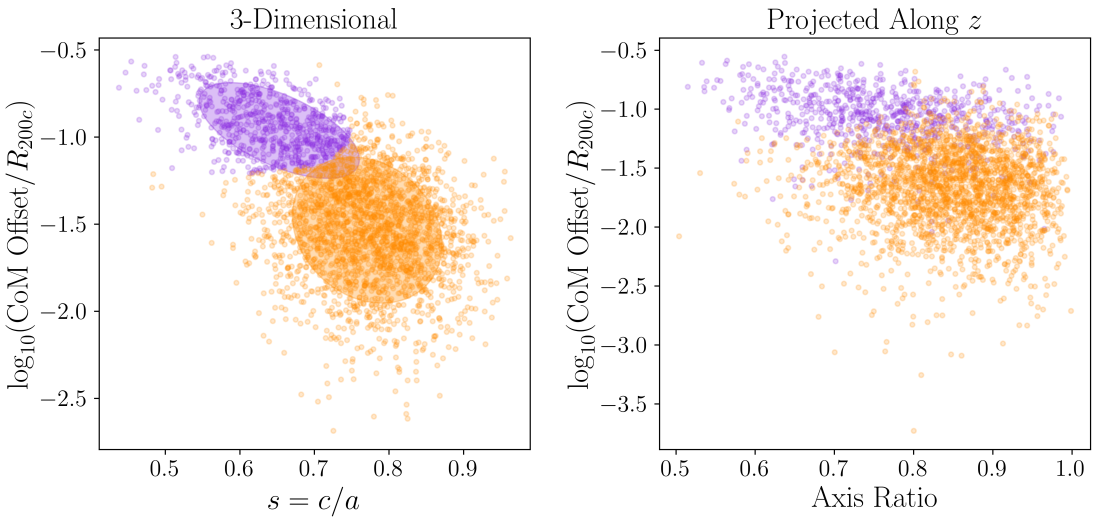


Figure 3.15: The distribution of centre of mass offsets and axis ratios within R_{200c}, both in 3D and projected along the z-axis, for halos with masses $1 \times 10^{13} < M_{200c}/M_{\odot} < 5 \times 10^{13}$ at redshift $z = 0$ in the TNG300-1 simulation. The left panel shows the centre of mass offset and major-to-minor axis ratio $s = c/a$ computed in 3D for each halo, sorted into two groups using a 2-component Gaussian mixture model on the two structural parameters. The shaded regions are the 1σ boundaries for the Gaussian fit components, and the colours of the dots represent the group membership of the halos. The right panel shows the centre of mass offset and axis ratio computed from the projected mass distributions. The colours in the right panel indicate the same group memberships of the halos as fit in the left panel.

distribution. If a halo features two dominant galaxies with high stellar mass, the preferred axes of rotation inferred from that mass distribution will have one very dominant axis, resulting in an extreme galaxy axis ratio near zero.

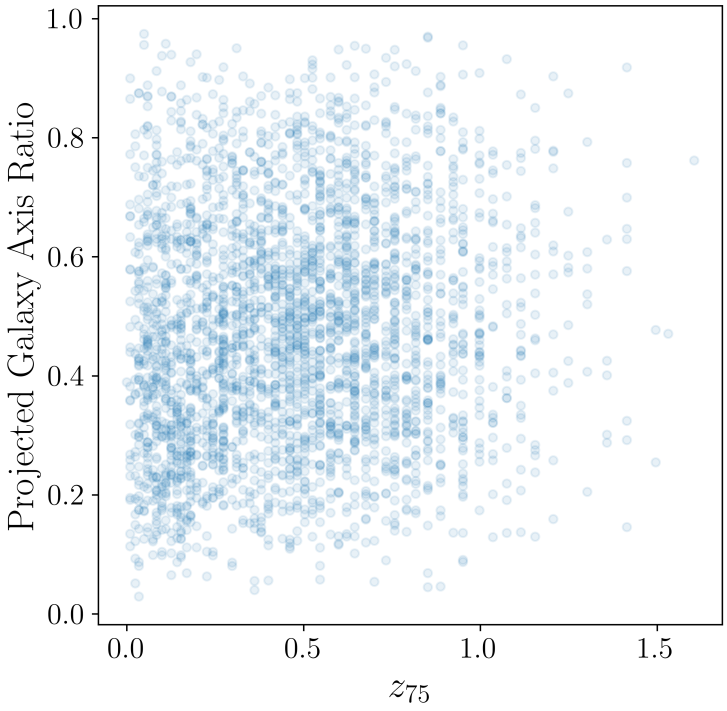


Figure 3.16: The projected galaxy axis ratio plotted against the z_{75} mass history for halos with masses $1 \times 10^{13} < M_{200c}/M_{\odot} < 5 \times 10^{13}$ at redshift $z = 0$ in the TNG300-1 simulation. Galaxy axis ratios are computed from stellar masses of galaxies within a 0.5 Mpc radius tangent to the z-axis and ± 1000 km/s along the z-axis around the BCG. The z_{75} parameter is computed from M_{200c} of the main halo progenitor.

We have found that axis ratios carry much less information about the mass accretion history of halos than centre of mass offsets, that much of the signal from axis ratios is washed out when measured in projection, and that galaxy axis ratios computed from readily observable features of clusters offer no useful mass history information. As a result, we conclude that axis ratios are not an effective indicator of the recent mass accretion history of galaxy clusters.

3.3 Concentration

The concentration of a halo is a measurement of its density profile, as described in Sections 1.3.2 and 2.3.3. We make use of the concentrations for IllustrisTNG halos provided in a supplementary data catalogue by Anbajagane et al. (2022). These concentrations are defined as $c_{200c} = R_{200c}/r_s$, where r_s is the scale radius of the NFW profile of a cluster. We expect the concentration of a halo to be correlated with its mass accretion history since concentration is primarily determined by the mean density of the universe when the halo formed (Navarro et al., 1997; Paranjape et al., 2015). As the universe expands and its mean density decreases, we expect more recently formed halos to be less concentrated. As a result, halos with high concentrations are expected to be older and dynamically relaxed systems, whereas halos with low concentrations are expected to be younger and dynamically disturbed systems.

As an initial indication of how well concentration correlates with recent mass accretion history, we compare it to the mass history parameter z_{75} for halos at redshift $z = 0$ in Figure 3.17. We see from this figure that concentration is correlated with z_{75}, though there is significant scatter in the relationship. Additionally, while halos with higher concentrations tend to have higher z_{75}, there is also a population of young halos with very low z_{75} that also have high concentrations. This highly concentrated but very young population of halos likely represents systems undergoing mergers. Concentration has been shown to oscillate during mergers due to the infall and splashback of merging material, as seen in Ludlow et al. (2012); Lee et al. (2018); Wang et al. (2020). As a result, it is reflected in Figure 3.17 that halos which have experienced mergers at $z_{75} \simeq 0.1$ often have high concentrations at $z = 0$ due to the infalling group, while halos that have experienced mergers at $z_{75} \simeq 0.2$ have passed through each other and developed lower concentrations at $z = 0$. The distribution in Figure 3.17 suggests that a sample of clusters with very low concentrations would represent young systems, but that sample of young systems would not be a representative sample of systems with recent mergers. Additionally, systems with high concentrations do not consistently represent older, relaxed systems, as they also include young and very unrelaxed systems.

In Figure 3.18, we compare concentration and centre of mass offset in terms of how well they trace z_{75} mass history. In the left panel of the figure, we see from the colour scale that the centre of mass offset effectively picks out all of the systems with low z_{75}, regardless of whether they have high or low concentration. In the right panel of Figure 3.18, we fit a three-dimensional Gaussian mixture model to the distribution of concentrations, centre of mass offsets and z_{75}. We see from the 1σ contours of the model and the grouping of the points that the unrelaxed halos are identified across a wide range of concentrations.

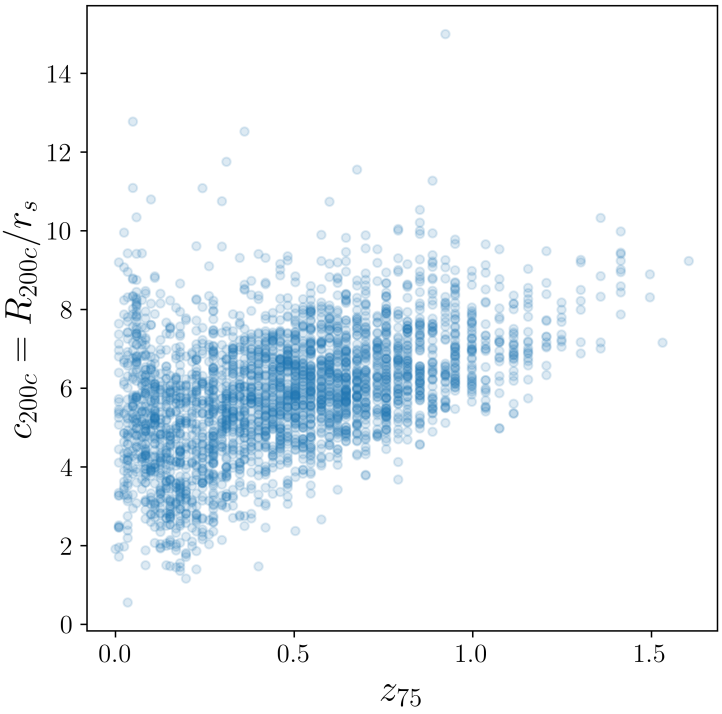


Figure 3.17: The NFW concentration plotted against the z_{75} mass history for halos with masses $1 \times 10^{13} < M_{200c}/M_\odot < 5 \times 10^{13}$ at redshift $z = 0$ in the TNG300-1 simulation. The concentration taken as recorded in IllustrisTNG's halo catalogue. The z_{75} parameter is computed from M_{200c} of the main halo progenitor.

This indicates that most of the mass history information is carried by centre of mass offset rather than by concentration. This result suggests that if sufficiently precise information about the mass distribution of a halo is available to compute its concentration, computing the centre of mass offset would yield a much better estimate of the recent mass accretion history of the cluster.

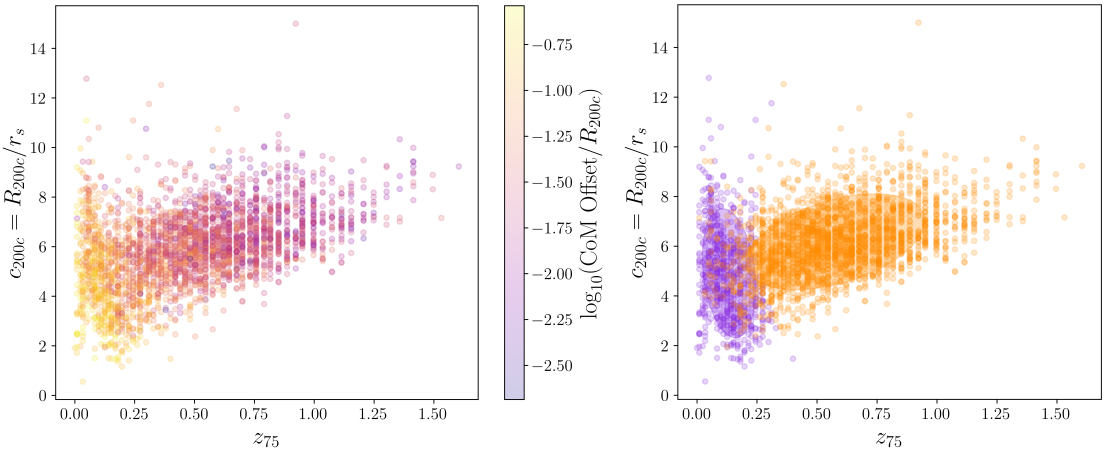


Figure 3.18: The distribution of NFW concentrations, z_{75} mass histories, and centre of mass offsets for halos with masses $1 \times 10^{13} < M_{200c}/M_\odot < 5 \times 10^{13}$ at redshift $z = 0$ in the TNG300-1 simulation. The centre of mass offsets are shown in colour scale in the left panel and omitted from the right panel. The right panel splits the distribution into groups using a 2-component Gaussian mixture model on the three parameters. The shaded regions in the right panel are the 1σ boundaries for the Gaussian fit components in the dimensions of the two axes, and the colours of the dots represent the group membership of the halos. Centre of mass offsets are computed from particles with R_{200c} in 3D around the most bound particle in each halo. Concentrations are taken as recorded in IllustrisTNG's halo catalogue. The z_{75} parameter is computed from M_{200c} of the main halo progenitor.

We have found that for older systems, concentration is correlated with mass accretion history. However, young systems have a broad range of concentrations that complicate the relationship between concentration and mass accretion history. Halos with low-concentrations could form a low contamination but incomplete sample of young systems. Other structural measurements, such as centre of mass offset, pick out halos that have experienced recent major mergers more reliably than concentration does.

3.4 Asymmetry

The asymmetry of a cluster is the amount of mass fluctuation in a cluster that is not symmetric under rotation around the BCG, as described in Section 2.3.4. Halos with massive galaxies that are not symmetrically distributed around the centre of the cluster will have high asymmetry numbers A. We expect asymmetry to be correlated with recent mass accretion through major mergers since infalling material to a halo should produce a large mass component that is offset to one side of the BCG and not equally represented on the other side of the halo. Systems with large asymmetries should thus be young and dynamically unrelaxed. Conversely, systems with small asymmetries should have a little of infalling material, which enables the mass distribution to settle symmetrically about the halo centre. Systems with small asymmetries are thus expected to be old and dynamically relaxed systems.

As an initial indication of how well asymmetry correlates with recent mass accretion history, we compare it to the mass history parameter z_{75} for halos at redshift $z = 0$ in Figure 3.19. The asymmetry around halos was computed using the full-volume particle distribution described in Section 2.2. For each halo, we considered particles within a radius R_{200c} tangent to the z-axis and a depth of ± 2 Mpc/h along the z-axis around the BCG. We see in Figure 3.19 that asymmetry is strongly correlated with z_{75}. There is a clear dense population of points with high asymmetries and low z_{75}, and a linear relationship between $\log_{10}(A)$ and z_{75}. There is considerable scatter in the relationship, particularly at lower asymmetries. However, a sample of halos with high asymmetries should be dominated by young systems, while a sample with low asymmetries should have very few young systems.

In Figure 3.20, we compare asymmetry to projected centre of mass offset and investigate how well they each trace z_{75} mass history. We see in the figure that asymmetry and projected centre of mass offset are quite correlated. This indicates that dynamically relaxed systems tend to have lower projected offsets and lower asymmetries, while dynamically unrelaxed systems have reliably high offsets and asymmetries. The colour scale of Figure 3.20 reflects how these structural parameters correlate with z_{75} mass history. We see that the z_{75} colour contours trace both projected offset and asymmetry. This distribution suggests that with knowledge of the projected mass distribution of a halo, using cuts in both asymmetry and projected centre of mass offset could yield reliable groups of young and old halos.

Given the strong correlation between the asymmetry and mass accretion history parameter z_{75} of halos seen in Figures 3.19 and 3.20, we investigate how effectively asymmetry can differentiate the full mass accretion histories of halos. In Figure 3.21, we split a sample

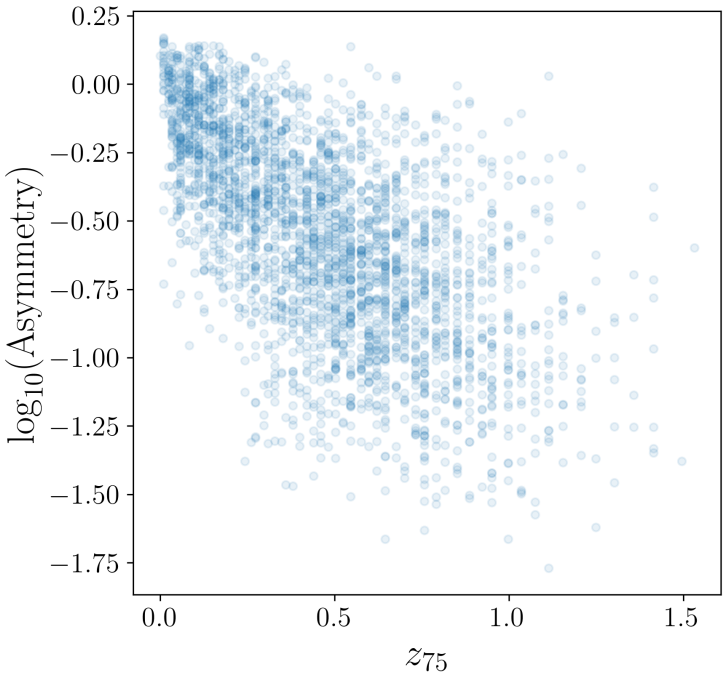


Figure 3.19: Halo asymmetry plotted against the z_{75} mass history for halos with masses $1\times 10^{13} < M_{200c}/M_{\odot} < 5\times 10^{13}$ at redshift $z = 0$ in the TNG300-1 simulation. The asymmetry was computed from the particles within R_{200c} tangent to the z-axis and ± 2 Mpc/h along the z-axis around the BCG. The particles were projected into the xy-plane and divided into 20 radial bins and 50 angular bins. The z_{75} parameter is computed from M_{200c} of the main halo progenitor.

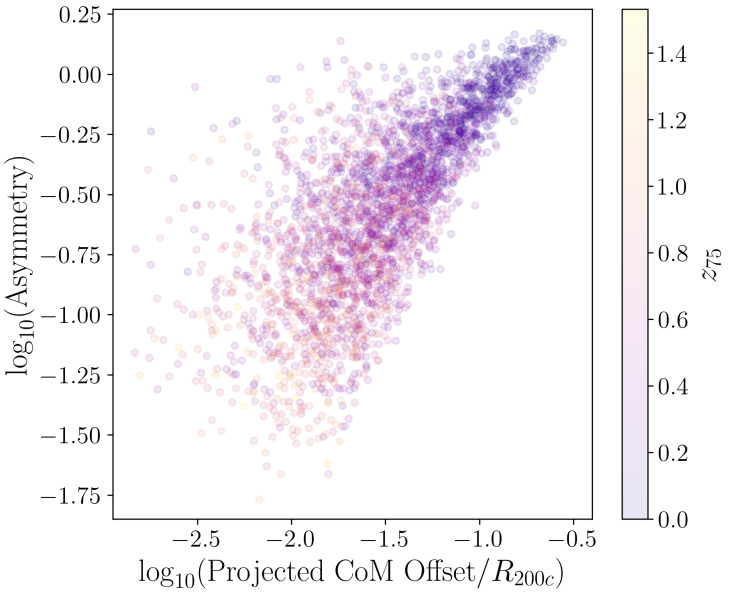


Figure 3.20: The asymmetry, projected centre of mass offset, and z_{75} mass history for halos with masses $1 \times 10^{13} < M_{200c}/M_{\odot} < 5 \times 10^{13}$ at redshift $z = 0$ in the TNG300-1 simulation. The asymmetry was computed from the particles within R_{200c} tangent to the z-axis and ± 2 Mpc/h along the z-axis around the BCG. The particles were projected into the xy-plane and divided into 20 radial bins and 50 angular bins. The centre of mass offsets were computed from particles of the FoF halo within R_{200c}, projected along the z-axis. The z_{75} parameter is computed from M_{200c} of the main halo progenitor and shown in colour scale.

of massive halos in the TNG300-1 simulation based on asymmetry and compare the median mass accretion histories of the groups. The top left panel of the figure shows the full distribution of asymmetries, while the top right panel divides the sample into the 20% of halos with the lowest asymmetries and the 20% of halos with the greatest asymmetries. In the bottom two panels of Figure 3.21, we compare the median mass accretion histories of these two groups. In the bottom left panel, we see that the dynamically relaxed halos accumulate their mass gradually with little mass accretion at low redshift. The dynamically unrelaxed group experiences a jump in mass at low redshift consistent with recent major mergers. The two median normalised accretion history curves are well separated given their uncertainties, and the 1σ scatter around the means do not overlap. The bottom right panel of the figure shows the non-normalised mass accretion histories. We see that the two groups had similar rates of mass accretion until low redshift, at which point the unrelaxed group accreted mass more slowly, then rapidly increased to the same final mass as the relaxed group at very low redshift.

The asymmetry of halos traces their recent mass accretion history well, but it is a difficult quantity to measure observationally. Asymmetry as defined in this work is based on the total mass distribution of a halo, which is dominated by dark matter and thus difficult to map accurately for individual systems. To account for this, we must establish an observationally accessible proxy for total mass asymmetry to more easily capture mass history information in real galaxy clusters. We propose the stellar mass asymmetry as such a measurement. Stellar mass asymmetry is analogous to total mass asymmetry, except that it is computed from Equation 2.9 using only the stellar mass in and around a halo. This measurement is much easier to obtain observationally, especially since diffuse stellar mass that is difficult to detect in observation does not greatly affect the mass-weighted asymmetry calculation.

In Figure 3.22, we split our sample of massive halos in the TNG300-1 simulation based on stellar mass asymmetry and compare their median mass accretion histories. In the top left panel of the figure, we see the full distribution of stellar mass asymmetries for our sample. In order to be observationally realistic, the asymmetries were computed from the stellar mass within a fixed 0.5 Mpc/h radius tangent to the z-axis and within $\pm$10 Mpc/h along the z-axis around the BCG to account for projection effects. We note that the stellar asymmetry distribution is significantly different from the distribution of total mass asymmetries seen in the top left panel of Figure 3.21. Rather than peaking in the middle of the distribution, the stellar mass asymmetries peak toward high values. The distribution also has a tail toward low asymmetries. These differences in the shapes of the distributions of stellar and total mass asymmetries for halos are due to the difference in the spatial distributions of stars and total mass in halos. The total mass of a cluster is dominated

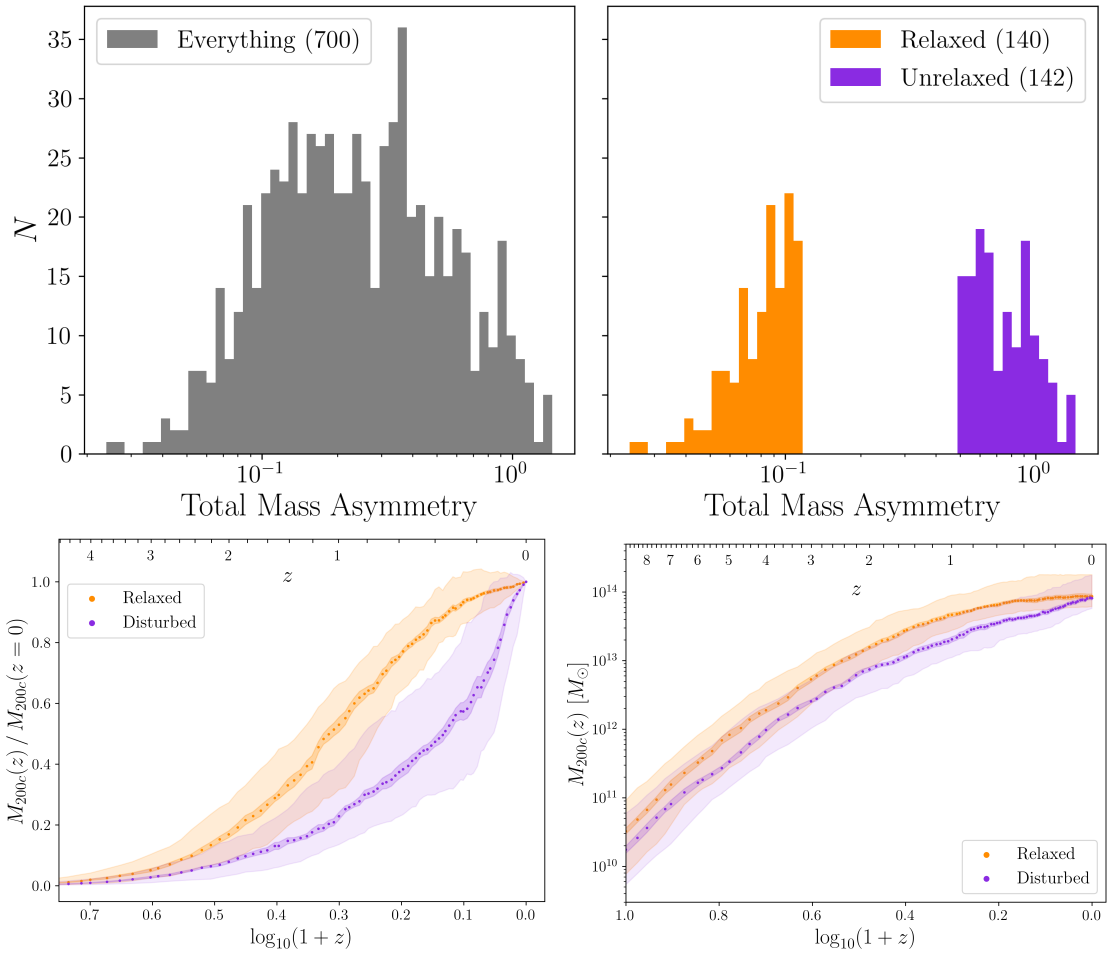


Figure 3.21: The asymmetry and median mass accretion histories for halos with masses $M_{200c} > 5 \times 10^{13}\, M_\odot$ at redshift $z = 0$ in the TNG300-1 simulation. The top left panel is the full distribution of total mass asymmetries projected along the z-axis, and the top right panel splits the top and bottom 20% of halos into relaxed and unrelaxed groups based on this distribution. Asymmetries were computed from the total mass within R_{200c} tangent to the z-axis and ± 2 Mpc/h along the z-axis around the BCG. In the bottom left panels, the points represent the median masses of halos in each group at the available snapshots. The thin shaded regions around the points are the errors on the medians computed via bootstrap. The large shaded regions around the points are the 1σ variations around the medians. The bottom left panel normalises each halo's mass history to its mass at redshift $z = 0$. The bottom right panel shows the masses in log scale.

by dark matter, which is distributed smoothly throughout the halo according to an NFW profile, as described in Section 1.3.2. The stellar mass, by contrast, is concentrated in galaxies and around the BCG and is thus not distributed smoothly through the halo. The difference between the surface mass densities of total mass and stellar mass for a massive halo are illustrated in the top left panels of Figures 2.1 and 2.7. Due to the more uneven distribution of stellar mass in halos, the stellar mass asymmetry is generally greater than the total mass asymmetry since most galaxies do not have a well-matched counterpart symmetric around the BCG. Given the stellar mass asymmetry distribution in Figure 3.22, we split the 20% of halos with the lowest asymmetries into a relaxed group and the 20% with the greatest asymmetries into an unrelaxed group in the top right panel of the figure. In the bottom panels of Figure 3.22, we compare the median mass accretion histories of the two groups. Similarly to the total mass asymmetry case, we see that the dynamically relaxed halos accumulate their mass gradually with little mass accretion at low redshift, while the dynamically unrelaxed group experiences mass accretion at low redshift consistent with recent major mergers. The two median normalised accretion history curves are similarly well separated to the total mass asymmetry case, suggesting that stellar mass asymmetry is similarly effective as an indicator of recent mass accretion history.

We have found that the mass asymmetry of halos is well correlated to their recent mass accretion history. Asymmetry carries a similar amount of information as projected centre of mass offset and is also computed from the mass distribution of a halo projected along the line of sight. Given good measurements of the total mass distribution of halos, asymmetry could be used in combination with centre of mass offset to effectively identify relaxed and unrelaxed halos. Halos with the greatest and lowest asymmetries have very different median mass accretion histories, with the unrelaxed systems having experienced recent major mergers. Additionally, asymmetry measured from only the stellar mass distribution within a large line of sight volume around halos produces groups with similarly distinct mass accretion histories. This shows that, unlike galaxy offset, stellar mass asymmetry is a readily observable quantity that can effectively identify samples of old and young clusters.

3.5 Magnitude Gap

The magnitude gap of a cluster is the difference between the magnitudes of the brightest galaxies in the cluster in some photometric band. A similar quantity that we will call the mass gap is the difference in $\log_{10}$(stellar mass) of the most massive galaxies in a cluster. Both of these measurements are described in more detail in Section 2.3.5. We expect the magnitude gap of a cluster to be correlated with its recent mass accretion history

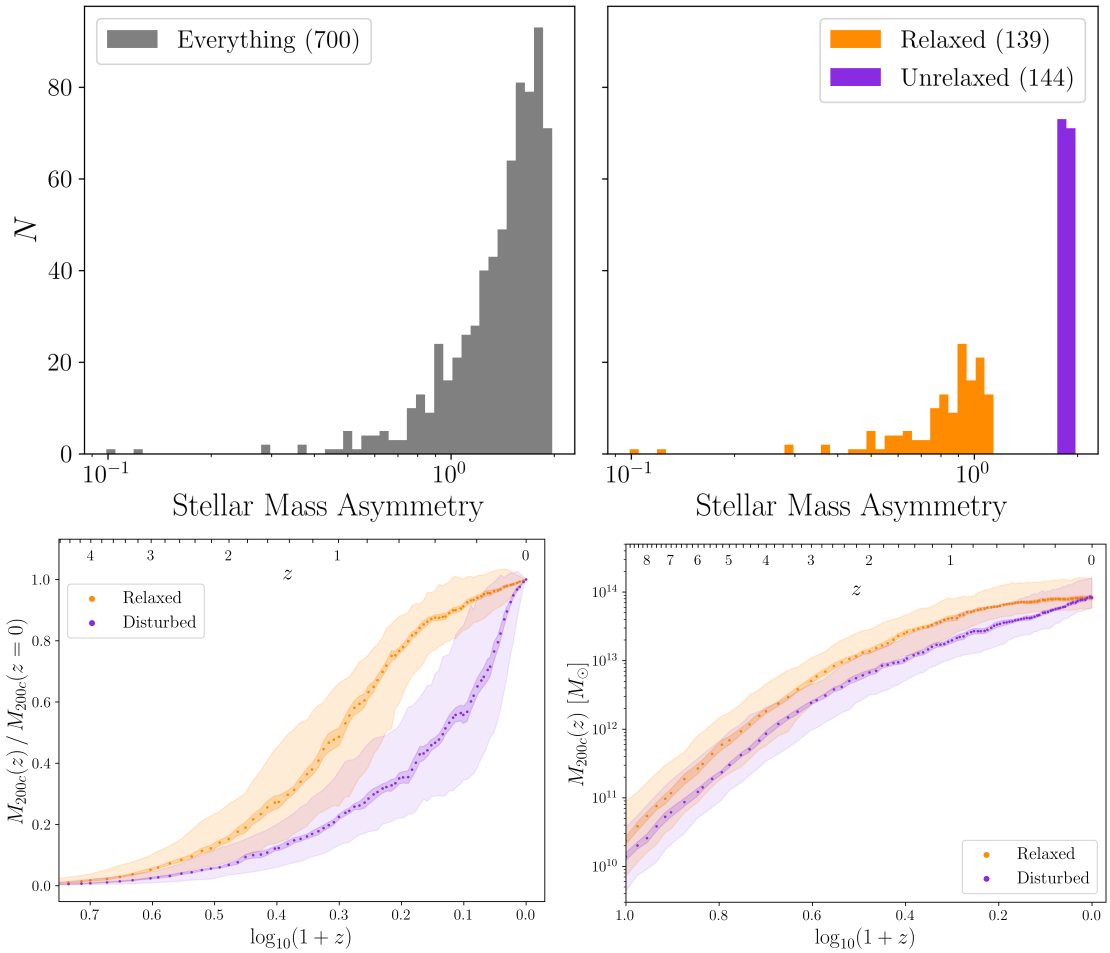


Figure 3.22: The stellar mass asymmetry and median mass accretion histories for halos with masses $M_{200c} > 5 \times 10^{13}\, M_\odot$ at redshift $z = 0$ in the TNG300-1 simulation. Asymmetries were computed from the stellar mass within a 0.5 Mpc/h radius tangent to the z-axis and ± 10 Mpc/h along the z-axis around the BCG. The top left panel is the full distribution of stellar mass asymmetries projected along the z-axis, and the top right panel splits the top and bottom 20% of halos into relaxed and unrelaxed groups based on this distribution. In the bottom left panels, the points represent the median masses of halos in each group at the available snapshots. The thin shaded regions around the points are the errors on the medians computed via bootstrap. The large shaded regions around the points are the 1σ variations around the medians. The bottom left panel normalises each halo's mass history to its mass at redshift $z = 0$. The bottom right panel shows the masses in log scale.

since major mergers insert massive galaxies into the cluster, thus decreasing its magnitude gap. As a result, clusters with small magnitude gaps should be young and dynamically unrelaxed systems. Conversely, the central galaxy of a cluster that formed earlier will have cannibalised other massive galaxies, reducing the magnitude gap (Farahi et al., 2020). Consequently, systems with large magnitude gaps should be old and dynamically relaxed.

In contrast to other structural measurements in this section, we make use of multi-dimensional information to correlate magnitude gaps to the dynamical states and mass accretion histories of clusters. In particular, we consider the magnitude gap between the two brightest galaxies in both the r and g bands, as well as the mass gap between the most and fourth most massive galaxies in each cluster. For each cluster, we only consider galaxies within R_{500c}. In the left panels of Figure 3.23, we plot the distributions of these magnitude and mass gaps for massive halos in the TNG300-1 simulation. The bottom left panel of the figure shows the distribution of r-band magnitude gaps and first-to-fourth stellar mass gaps, which has some significant scatter. In contrast, the top right panel of Figure 3.23 shows a strong degeneracy between the r-band and g-band magnitude gaps in clusters. This is because nearly all galaxies in massive clusters in the IllustrisTNG MHD simulations have very similar colours.

In Figure 3.24, we plot the g − r colours of all galaxies with stellar masses $M^* > 1 \times 10^{10}\, M_\odot$ in the TNG300-1 simulation against their r-band magnitudes. We see that while there is a broad distribution of colours for general galaxies, nearly all of the galaxies that are within the inner regions of massive clusters are very red in colour. These galaxies are part of the red sequence, which is a population of galaxies with little star formation that are known to dominate clusters (Gladders & Yee, 2000; Valentinuzzi et al., 2011). We see also in Figure 3.24 that galaxies which would be projected into the inner regions of clusters are also dominantly red sequence. This indicates that projection effects cannot significantly break the degeneracy between r- and g-band magnitude gaps.

In the right panels of Figure 3.23, we split the sample of massive clusters into dynamically relaxed and unrelaxed groups based on the three magnitude and mass gaps displayed on the axes. The relaxed group comprises the 20% of clusters with the largest gaps, while the unrelaxed group comprises the 20% of clusters with the smallest gaps. Given these splits, we examine the median mass accretion histories of the dynamically relaxed and unrelaxed groups in Figure 3.25. We see in the left panel that the relaxed group experiences gradual mass accretion with little growth at low redshift, while the unrelaxed group experiences rapid mass accretion at low redshift, consistent with recent major mergers. The median mass histories of the two groups are well separated within their small uncertainties, and there is a separation between the 1σ scatters about the median at the region of greatest separation. In the right panel of Figure 3.25, we see that the two groups have

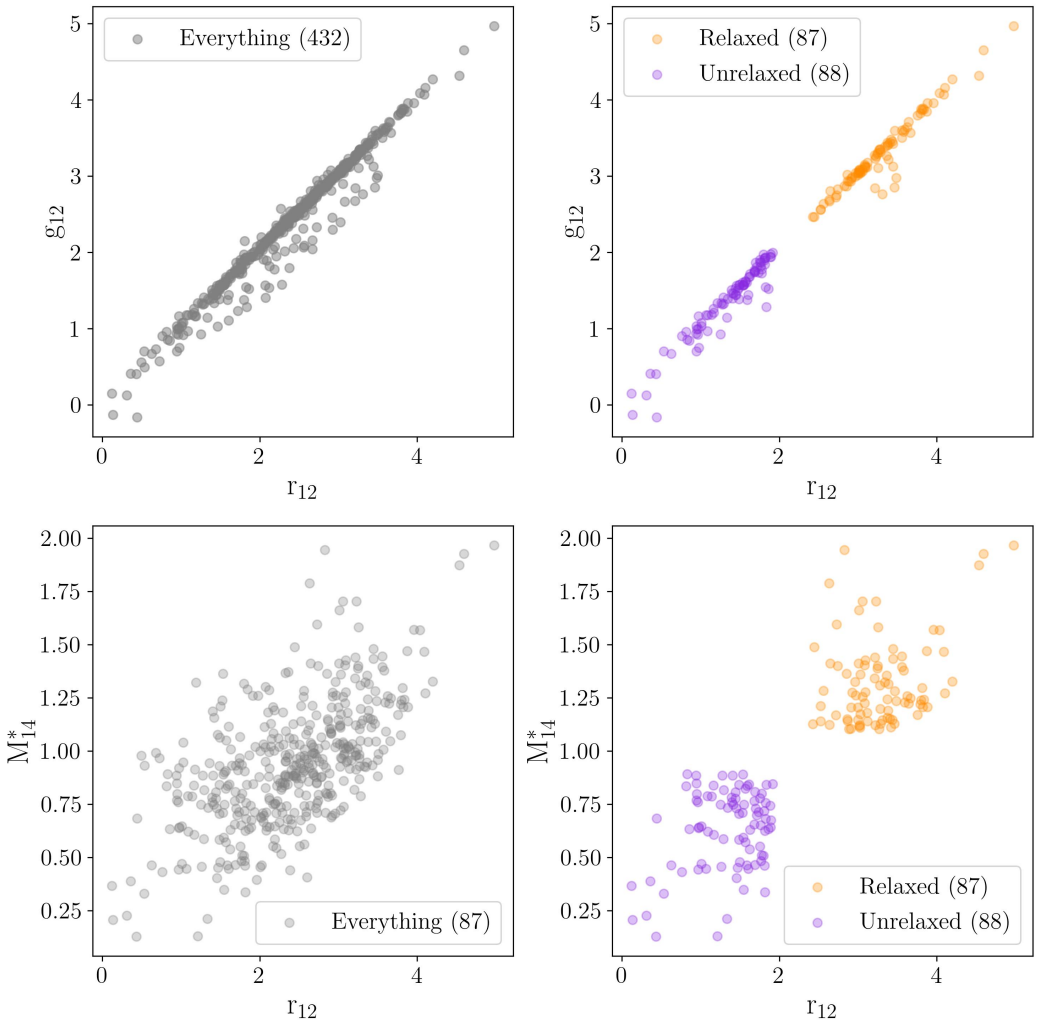


Figure 3.23: The magnitude and mass gaps of galaxies within R_{500c} for halos with masses $M_{500c} \geq 5 \times 10^{13}\, M_{\odot}$ at redshift $z = 0$ in the TNG300-1 simulation. The left panels show the full distribution of magnitude and mass gaps, and the right panels split the top and bottom 20% of halos into relaxed and unrelaxed groups based on this distribution. The "r_{12}" axis represents the magnitude gap between the two brightest galaxies in the r-band. The "g_{12}" axis represents the g-band magnitude gap between those same two galaxies. The "M^*_{14}" axis represents the difference in $\log_{10}$(Stellar Mass) of the first and fourth most massive subhalos. Magnitudes and stellar masses were computed from stellar particles within 30 kpc of the most bound particle in each subhalo.

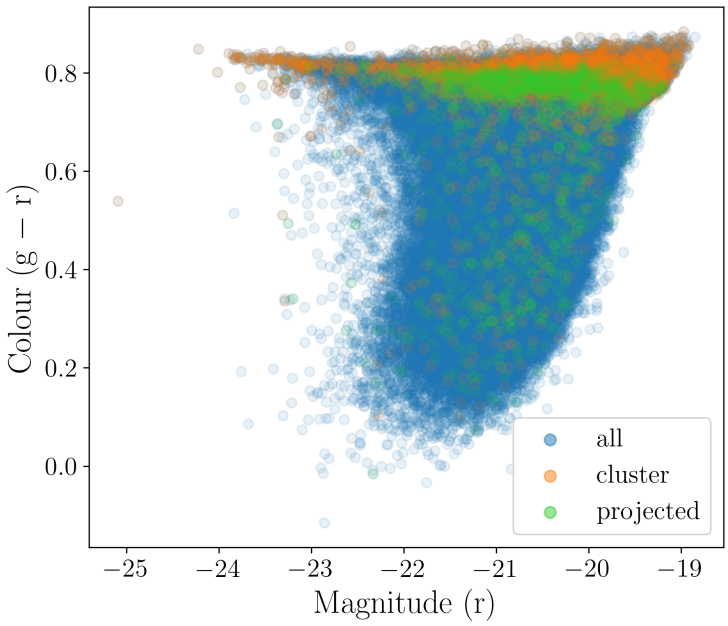


Figure 3.24: A colour-magnitude diagram for galaxies with stellar masses $M^* \geq 1 \times 10^{10}\, M_\odot$ at redshift $z = 0$ in the TNG300-1 simulation. The independent axis has the intrinsic r-band magnitude of the galaxies, while the dependent axis has the colour in g-band minus r-band magnitude. The orange points represent galaxies that are within R_{500c} of clusters with masses $M_{500c} \geq 1 \times 10^{14}\, M_\odot$. The green points represent galaxies which would be projected into R_{500c} of clusters across the full simulation box. The blue points represent all other galaxies above the mass cut in the simulation. Magnitudes were computed from stellar particles within 30 kpc of the most bound particle in each subhalo.

similar relative rates of mass accretion for most of their histories until very low redshift, at which point the unrelaxed group experiences rapid accretion and surpasses the median mass of the relaxed group. Unlike when we split based on halo asymmetry in Section 3.4, the two groups have slightly different final masses when split based on magnitude gaps.

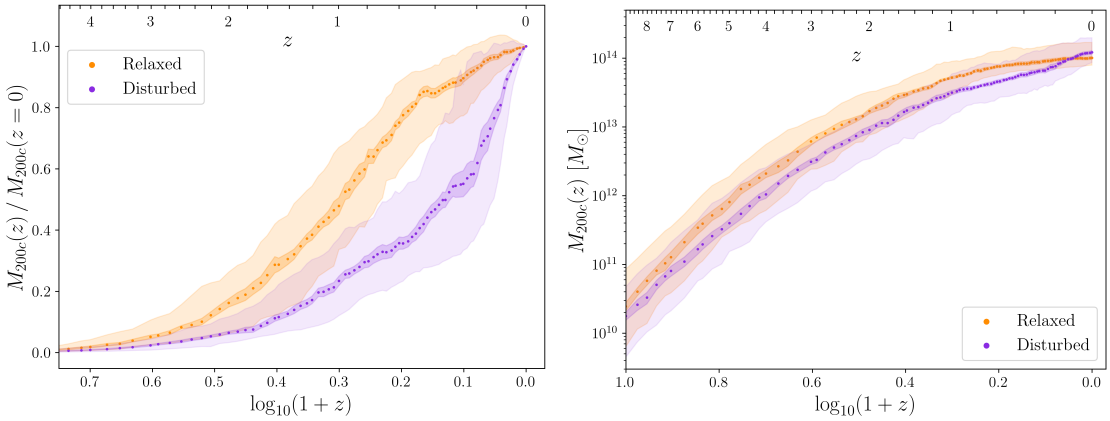


Figure 3.25: The median mass accretion histories for the relaxed and unrelaxed halos split by magnitude gaps in Figure 3.23. The points represent the median masses of halos in each group at the available snapshots. The thin shaded regions around the points are the errors on the medians computed via bootstrap. The large shaded regions around the points are the 1σ variations around the medians. The bottom left panel normalises each halo's mass history to its mass at redshift $z = 0$. The bottom right panel shows the masses in logarithmic scale.

We have found that magnitude gaps in clusters can be used to effectively distinguish between dynamically relaxed halos with little recent mass accretion and dynamically unrelaxed halos with recent major mergers. Given that magnitude gaps are readily observable in real clusters and that these splits require observations in few spectral bands, they are a valuable tool for distinguishing old and young clusters. Additionally, given that the measurement is dependent only on the magnitudes of the brightest galaxies, and given the easy discrimination of galaxies outside of the red sequence, magnitude gap measurements do not require precise line of sight information and are thus robust to projection effects.

Chapter 4

Radial Structure and Optical Selection

In this chapter, we explore how the optical properties that we use to classify galaxy clusters as dynamically relaxed and unrelaxed correlate with the clusters' projected radial mass profiles. We also compare three-dimensional halo identification to optical cluster selection, and we investigate how our measurements may be affected by projection effects. Lastly, we compare the structure of our simulated clusters to that of real observational clusters from the DESI Legacy Imaging Survey (DLIS) (Dey et al., 2019) and the Ultraviolet Near Infrared Optical Northern Survey (UNIONS) (Gwyn et al., 2025) surveys.

4.1 Dynamical Splits

In this section, we explore how the structural and optical properties of galaxy clusters correlate with their projected radial mass profiles. In particular, we consider the structural parameters defined in Section 2.3 and their optical proxies explored in Chapter 3. We use these parameters to classify halos as dynamically relaxed and unrelaxed, and we compare the average weak gravitational lensing profiles $\Delta\Sigma(R)$ of the relaxed and unrelaxed groups. Our calculations of gravitational lensing profiles around halos are described in Section 2.6.

4.1.1 Centre of Mass Offset & Galaxy Offset

We first explore how well the projected centre of mass offset as defined in Section 2.3.1 is correlated to the lensing profiles of massive clusters in the TNG300-1 simulation at redshift $z = 0$. As is shown in Section 3.1, halos with a large projected offset are dynamically unrelaxed, while halos with small offsets tend to be relaxed. In the top left panel of Figure 4.1, we plot the distribution of projected centre of mass offsets within R_{200c} for massive clusters. In the top right panel of the figure, we split the sample into two groups. The 20% of halos with the smallest offsets are grouped as dynamically relaxed, while the 20% with the greatest offsets are grouped as dynamically unrelaxed. In the bottom panel of Figure 4.1, we plot the mean gravitational lensing profiles of the two groups. We see that the relaxed halos have a stronger $\Delta\Sigma$ lensing signal within a 1 Mpc radius of the centre of the BCG. The difference between the two lensing profiles is most significant at a radius of $\sim 0.3\,\mathrm{Mpc}$. The greater lensing signal for relaxed halos at low radii suggests that halos with small centre of mass offsets have more steeply declining density profiles in their cores. This is reflected in the definition of the lensing profile given in Equation 2.15. We see in this equation that a high value of $\Delta\Sigma$ indicates that the average surface mass density within the given radius R is greater than the surface mass density at R. Consequently, the greater the value of the lensing profile at some radius, the more significantly the surface mass density of the halo has decreased. This enables us to understand the difference in lensing signals between relaxed and unrelaxed halos selected based on projected centre of mass offsets. A large offset indicates that there is significant mass outside the centre of the halo that pulls the centre of mass away from the BCG. Such a mass distribution in unrelaxed systems would decrease the contrast in surface mass density between the centre of the halo and the surrounding regions, resulting in a lower lensing signal. In contrast, halos with small centre of mass offsets tend to be more concentrated with more dominant central galaxies. This results in a large surface mass density decrease with radius and a stronger lensing signal.

We have established that the projected centre of mass offset, which traces the mass distribution of a halo, can be used to select galaxy cluster halos with notably different gravitational lensing profiles. In order to test a more readily observable structural parameter, we now consider how well an optical proxy for the centre of mass offset is able to distinguish between halos with different lensing profiles. The galaxy offset is defined in Section 3.1 as an observationally accessible proxy for the centre of mass offset. In Figure 4.2, we compare the structure of halos with different galaxy offsets. In the top left panel of the figure, we see the full distribution of galaxy offsets for massive halos. In the top right panel, we split the halo into relaxed and unrelaxed groups based on the galaxy

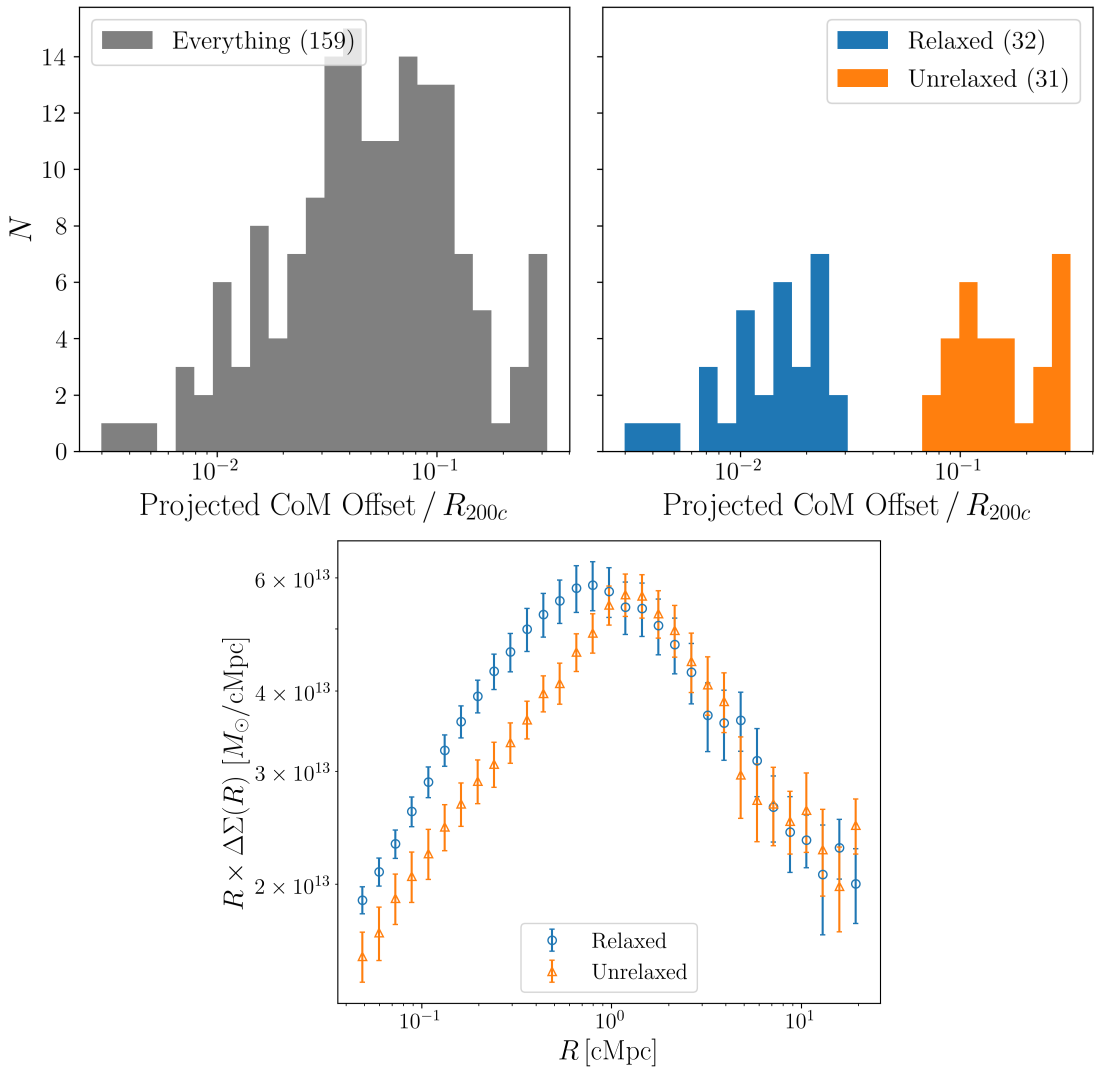


Figure 4.1: The z-axis projected centre of mass offsets and mean lensing profiles for halos with masses $M_{500c} \geq 1 \times 10^{14}\, M_\odot$ at redshift $z = 0$ in the TNG300-1 simulation. The top left panel is the full distribution of projected centre of mass offsets computed from the total mass within R_{200c}. The top right panel splits the top and bottom 20% of halos into relaxed and unrelaxed groups based on this distribution. In the bottom panel, the points represent the mean lensing signal for the clusters in each group, and the error bars are the uncertainty on the mean.

offsets. In the bottom panel, we compare the lensing profiles of the two groups. Similarly to the split based on projected centre of mass offsets, we see that the relaxed halos in Figure 4.2 have a stronger mean lensing signal in the inner regions than the unrelaxed halos. However, we also see that the relaxed halos also have a stronger lensing signal at higher radii $2\,\mathrm{Mpc} < R < 10\,\mathrm{Mpc}$. Given that these radii are well beyond the virial radius of halos in this mass range and that the shapes of the lensing profiles are similar, we recognise that the relaxed halos have a greater average mass than the unrelaxed halos. When verified directly, we find that the unrelaxed halos have a mean mass of $\sim 70\%$ that of the relaxed halos. This implies that a dynamical split based on galaxy offset introduces a bias in halo mass. As a result, galaxy offset is less effective than projected centre of mass offset at distinguishing between halos with different inner density profiles.

It is shown in Section 3.1 that projected centre of mass offset is a fair predictor of recent halo mass accretion history, while galaxy offset is a very poor predictor of mass accretion history. Given that these two structural parameters correlate quite differently with halo mass history, it is interesting that they can both identify systems with different inner density profiles as traced by $\Delta\Sigma$. However, the projected centre of mass offset identifies systems with similar total mass and different mass distributions, while the galaxy offset identifies systems with different total masses.

4.1.2 Total Mass Asymmetry & Stellar Mass Asymmetry

We now investigate how effectively halo asymmetry can select systems with different projected radial mass profiles. Asymmetry is a measurement of the mass fluctuations in a halo, as defined in Section 2.3.4. In the top left panel of Figure 4.3, we plot the distributions of asymmetries of massive halos in TNG300-1. In the top right panel, we classify the 20% of halos with the lowest asymmetries as relaxed and the 20% with the greatest asymmetries as unrelaxed. In the bottom panel of Figure 4.3, we plot the mean lensing profiles of the two groups. We see that the lensing profiles within 1 Mpc are very different. As with the projected centre of mass offset split in Figure 4.1, the relaxed halos have steeper density profiles than unrelaxed halos in the inner regions. A large asymmetry number A indicates that a halo has significant mass outside of the BCG which is not symmetrically distributed around the BCG. Such a significant mass distribution outside of the BCG decreases the contrast in surface mass density between the centre of the halo and the surrounding regions, resulting in a lower lensing signal. Halos with small asymmetries tend to be more concentrated with less mass outside the BCG, resulting in a steep surface mass density drop and a stronger lensing signal. Thus, the difference in gravitational lensing profiles in Figure 4.3 is reasonable for systems selected based on asymmetry.

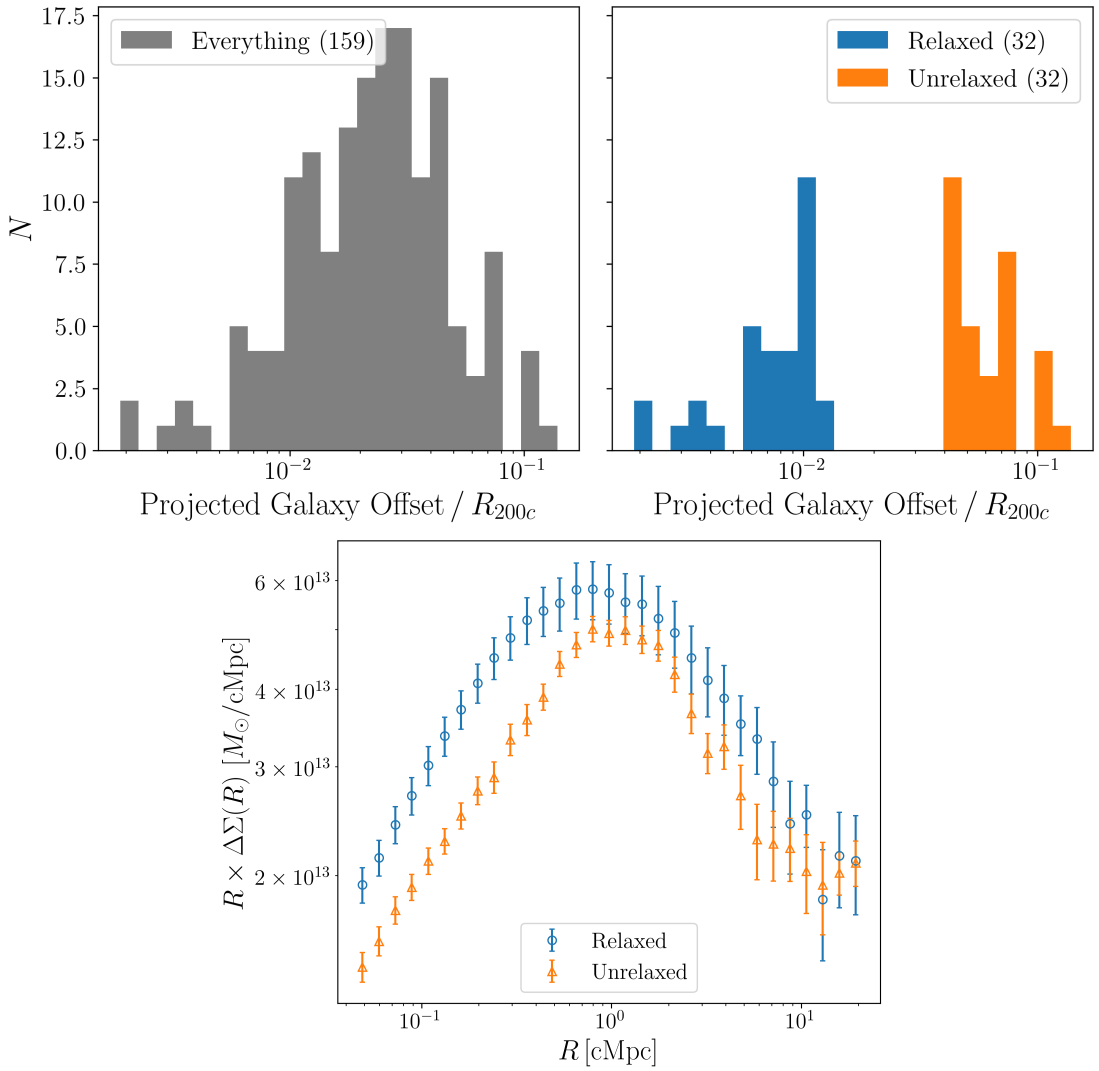


Figure 4.2: The z-axis projected galaxy offsets and mean lensing profiles for halos with masses $M_{500c} \geq 1 \times 10^{14}\, M_\odot$ at redshift $z = 0$ in the TNG300-1 simulation. The top left panel is the full distribution of projected galaxy offsets computed from the stellar masses of galaxies within a 0.5 Mpc radius tangent to the z-axis and $\pm$1000 km/s along the z-axis from the BCG. The top right panel splits the top and bottom 20% of halos into relaxed and unrelaxed groups based on the total distribution. In the bottom panel, the points represent the mean lensing signal for the clusters in each group, and the error bars are the uncertainty on the mean.

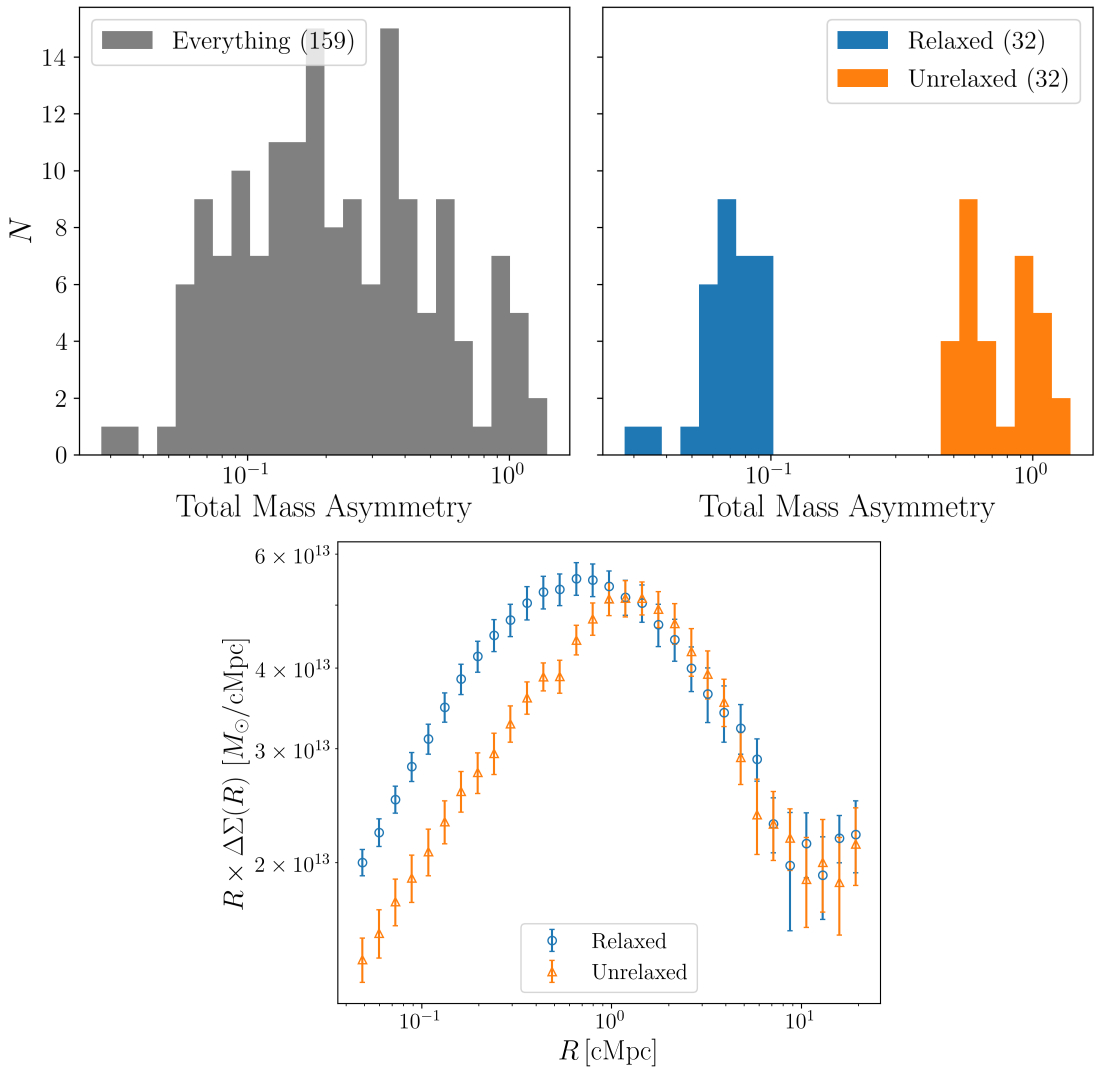


Figure 4.3: The asymmetries and mean lensing profiles of halos with masses $M_{500c} \geq 1 \times 10^{14}\, M_\odot$ at redshift $z = 0$ in the TNG300-1 simulation. The top left panel is the full distribution of total mass asymmetries projected along the z-axis. The top right panel splits the top and bottom 20% of the distribution into relaxed and unrelaxed groups. In the bottom panel, the points represent the mean lensing signal for the clusters in each group, and the error bars are the uncertainty on the mean.

The asymmetries of halos, which are based on their total mass distributions, can be used to select groups of clusters with different mean lensing profiles. We now explore how well the stellar mass asymmetry, which is an optical proxy defined in Section 3.4, can identify systems with different density profiles. In the top left panel of Figure 4.4, we plot the distribution of stellar mass asymmetries of massive halos. Unlike the distributions of other structural parameters explored in this section, this histogram is notably skewed. The skewness is due to the different mass distributions of dark matter and stars around the BCG, as is further explained in Section 3.4. In the top right panel of Figure 4.4, we categorise the 20% of halos with the smallest stellar asymmetries as relaxed and the 20% with the greatest stellar asymmetries as unrelaxed. In the bottom panel of the figure, we compare the mean lensing profiles of the two groups. We see that the lensing profiles of the relaxed and unrelaxed halos are quite different. The relaxed group again has a stronger signal within a 1 Mpc radius. The lensing profiles converge above 1 Mpc, indicating that the relaxed and unrelaxed halos are of the same mass and exist in environments with similar densities. In contrast to galaxy offset, stellar mass asymmetry is a structural parameter based on the distribution of stars that does not introduce a bias in halo mass.

The difference in the lensing profiles of relaxed and unrelaxed halos is greater for halos classified based on stellar mass asymmetry than for halos classified based on total mass asymmetry. This is particularly clear in the inner regions of the halos. Lensing profiles are a reflection of the total mass distribution. It is thus surprising that the total mass asymmetry splits halos less effectively than the stellar mass asymmetry, which does not necessarily trace the total mass distribution. However, it is observationally convenient that the more easily measurable asymmetry based on stellar mass most effectively predicts differences in the lensing profiles of clusters.

4.1.3 Magnitude Gap

The last optical structural parameters that we consider in this section are the magnitude gaps and the mass gaps of clusters. The magnitude and mass gaps are the differences in brightness or stellar mass of the largest galaxies in a cluster, as defined in Section 2.3.5. Unlike with the other structural parameters in this section, we use a multi-dimensional split between relaxed and unrelaxed halos by simultaneously using the mass gap and the magnitude gaps in two photometric bands. The left panels of Figure 4.5 show the full distribution of magnitude gaps in the r- and g-bands, as well as the distribution of stellar mass gaps between the first and fourth most massive galaxies in each cluster at redshift $z = 0$. The degeneracy between the magnitude gaps in the r- and g-bands is further explored in Section 3.5. In the right panels of Figure 4.5, we split the 20% of halos with

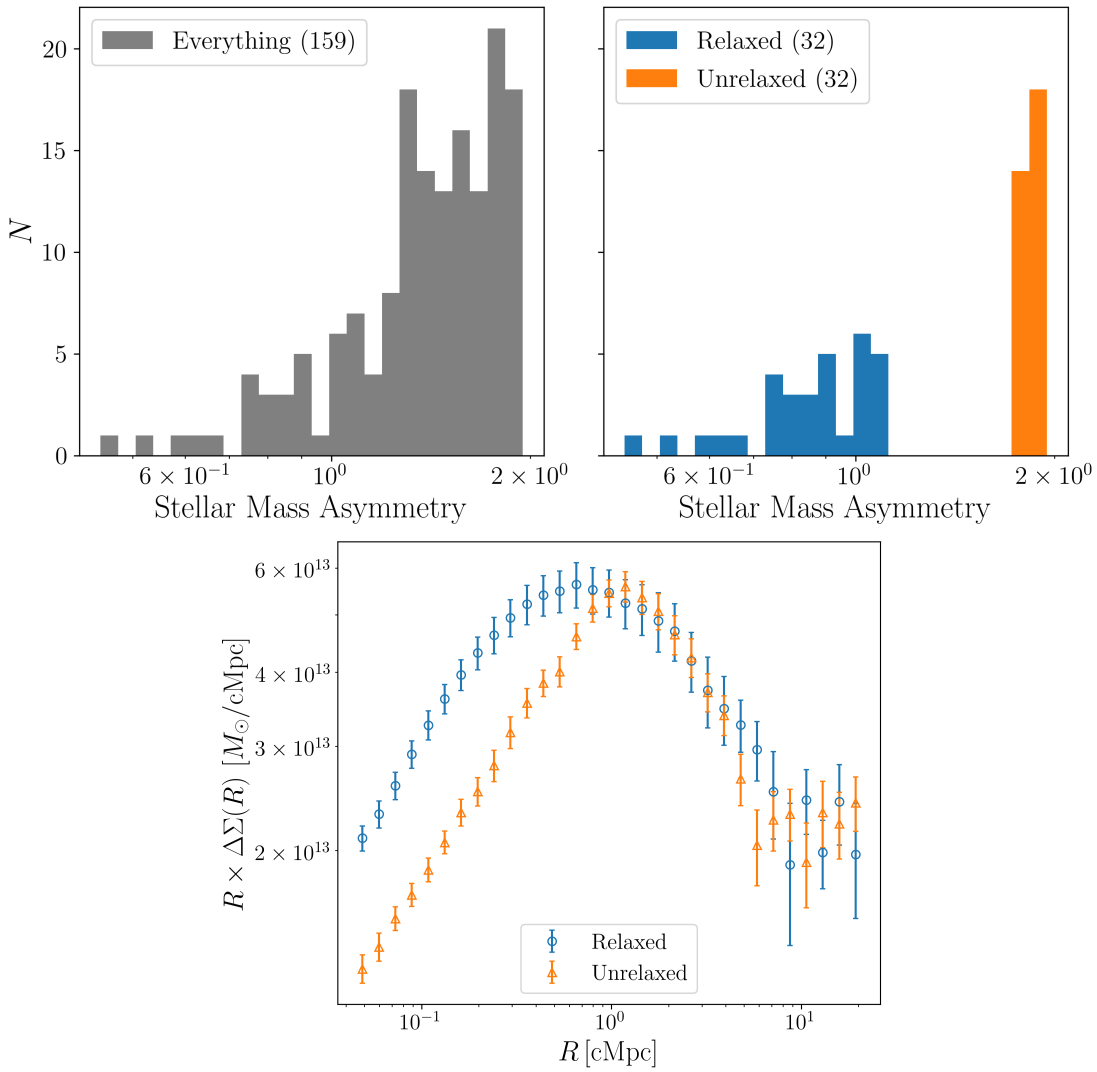


Figure 4.4: The stellar mass asymmetry and mean lensing profiles for halos with masses $M_{500c} \geq 1 \times 10^{14}\, M_\odot$ at redshift $z = 0$ in the TNG300-1 simulation. The top left panel is the full distribution of stellar mass asymmetries projected along the z-axis, and the top right panel splits the top and bottom 20% of halos into relaxed and unrelaxed groups based on this distribution. In the bottom panel, the points represent the mean lensing signal for the clusters in each group, and the error bars are the uncertainty on the mean.

the greatest magnitude and mass gaps into a dynamically relaxed group and the 20% with the greatest magnitude and mass gaps into a dynamically unrelaxed group.

In Figure 4.6, we examine the mean lensing profiles of the dynamically relaxed and unrelaxed groups at two different redshifts and minimum halo masses. The classification of halos with masses $M_{500c} \geq 1 \times 10^{14}\, M_{\odot}$ at redshift $z = 0$ is shown in Figure 4.5. The shapes of the distributions and the dynamical classifications for halos with masses $M_{500c} \geq 5 \times 10^{13}\, M_{\odot}$ at redshift $z = 0.4$ are similar and are thus omitted for brevity. In the left panel of Figure 4.6, we plot the difference in the mean lensing profiles of the relaxed and unrelaxed groups at $z = 0$. We see similar differences between lensing profiles as when we classified halos based on the projected centre of mass offsets and asymmetries. The relaxed group has a stronger lensing signal than the unrelaxed group within 1 Mpc, and the two mean lensing signals converge above 1 Mpc. A large magnitude gap indicates that the central galaxy in a cluster is very dominant, which leads to less mass outside of the BCG and thus a steeper density gradient for relaxed halos. A small magnitude gap implies that there is another massive galaxy outside of the BCG, which decreases the density gradient and leads to a more shallow density gradient for unrelaxed halos. Thus, the difference in gravitational lensing profiles in the left panel of Figure 4.6 is reasonable for systems selected based on magnitude and mass gaps.

In the right panel of Figure 4.5, we plot the difference in the lensing profiles for halos at redshift $z = 0.4$. We see a similar difference between the relaxed and unrelaxed profiles at low radii. However, the unrelaxed group has a large peak in the density profile at ~ 2 Mpc, and it has a greater lensing signal than the relaxed group at radii beyond this peak. These features suggest that the unrelaxed clusters are of greater average mass than the relaxed clusters, despite the weaker lensing signal in the centre. In Table 4.1, we list the mean masses of the relaxed and unrelaxed halos used to produce the lensing profiles in Figure 4.6. We see in the table that at redshift $z = 0$, the mean masses of the groups are consistent to within the uncertainties on the means. However, the relaxed and unrelaxed groups at redshift $z = 0.4$ have very different mean masses. This accounts for the greater amplitude of the unrelaxed lensing profile in Figure 4.6. We note that this bias in mean mass between the relaxed and unrelaxed groups classified based on magnitude gaps only occurs at the higher redshift. A range of mass thresholds were tested at both $z = 0.0$ and $z = 0.4$, and the difference in the mean masses is consistent across mass ranges at each redshift.

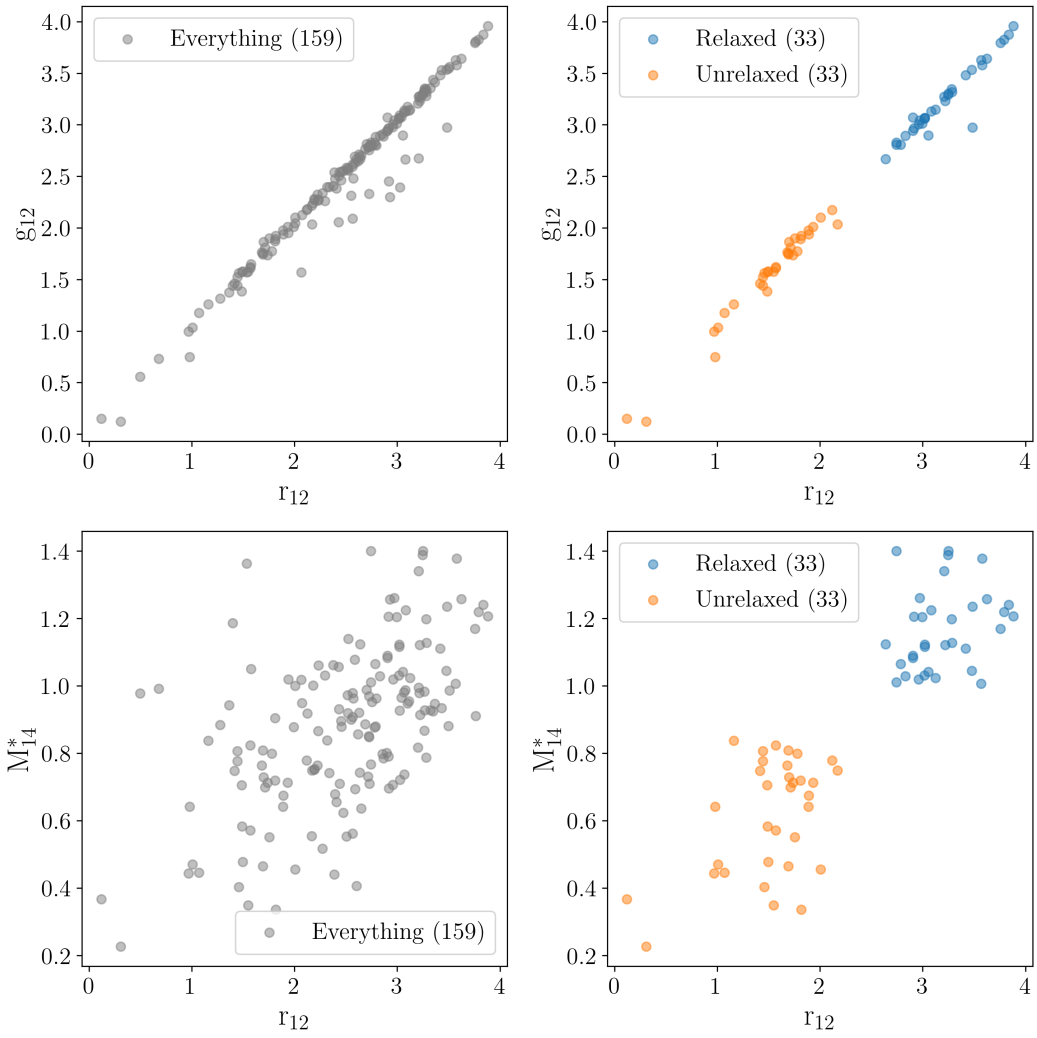


Figure 4.5: The magnitude and mass gaps of galaxies within R_{500c} for halos with masses $M_{500c} \geq 1 \times 10^{14}\, M_\odot$ at redshift $z = 0$ in the TNG300-1 simulation. The left panels show the full distribution of magnitude and mass gaps. The right panels split the top and bottom 20% of halos into relaxed and unrelaxed groups based on this distribution. The "r_{12}" axis represents the magnitude gap between the two brightest galaxies in the r-band. The "g_{12}" axis represents the g-band magnitude gap between those same two galaxies. The "M^*_{14}" axis represents the difference in $\log_{10}$(Stellar Mass) of the first and fourth most massive subhalos. Magnitudes and stellar masses were computed from stellar particles within 30 kpc of the most bound particle in each subhalo.

Redshift z	Relaxed $M_{500c}/(10^{14} M_\odot)$	Unrelaxed $M_{500c}/(10^{14} M_\odot)$
0.0	1.76 ± 0.20	1.89 ± 0.19
0.4	0.88 ± 0.06	1.39 ± 0.21

Table 4.1: The mean masses and uncertainties of relaxed and unrelaxed halo samples are classified based on magnitude and mass gaps. The halos at redshift $z = 0.0$ have a mass threshold $M_{500c} \geq 1 \times 10^{14}\, M_\odot$. The halos at redshift $z = 0.4$ have a mass threshold $M_{500c} \geq 5 \times 10^{13}\, M_\odot$. The halos at $z = 0.0$ were classified as relaxed or unrelaxed as in Figure 4.5, and the halos at $z = 0.4$ were classified analogously.

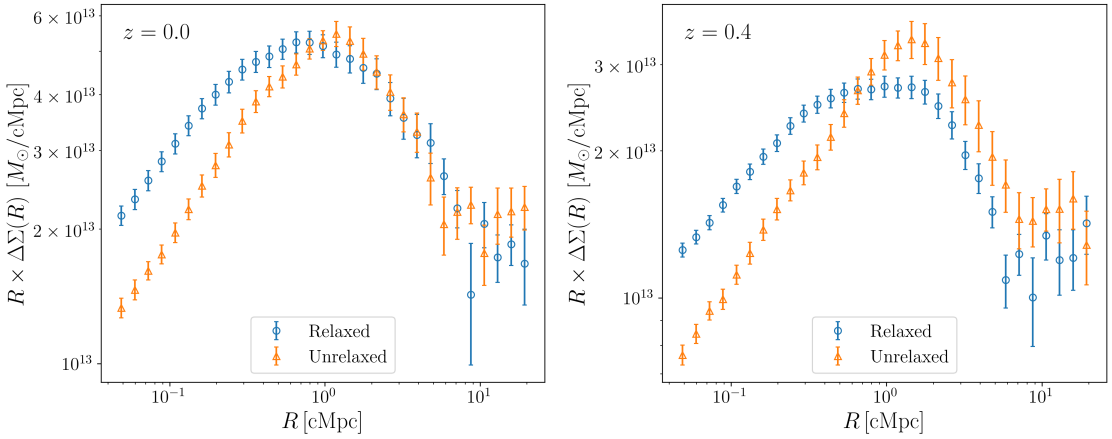


Figure 4.6: The mean lensing profiles $\Delta\Sigma$ for the relaxed and unrelaxed halos are classified based on magnitude and mass gaps in the TNG300-1 simulation. The left panel is computed for clusters at redshift $z = 0$ with masses $M_{500c} \geq 1 \times 10^{14}\, M_\odot$, and the sample is split as in Figure 4.5. The right panel is at redshift $z = 0.4$ for halos with masses $M_{500c} \geq 5 \times 10^{13}\, M_\odot$, and the sample is split analogously. The points represent the mean lensing signal for the clusters in each group, and the error bars are the uncertainty on the mean.

4.1.4 Comparison and Summary

It is important to establish whether the mean mass difference between relaxed and unrelaxed samples at redshift $z > 0$ is only present when the halos are classified based on magnitude gaps or whether it is consistent across structural parameter classifications. To determine this, we computed the total mass asymmetries and stellar mass asymmetries of halos at $z = 0.4$ in the TNG300-1 simulation. We then classified halos as relaxed or unrelaxed in each case and computed the mean lensing profiles of the groups, as was done in Figures 4.3 and 4.4. The resulting mean gravitational lensing profiles of the groups are shown in Figure 4.7. For both the total mass asymmetry classification in the left panel and the stellar mass asymmetry classification in the right panel, the peaks of the mean lensing profiles are at similar heights, and the outer regions of the lensing profiles converge. These features suggest that the relaxed and unrelaxed groups split based on asymmetry have similar mean masses at redshift $z = 0.4$. The mean masses of the groups are recorded in Table 4.2, where we see that they are all consistent to within their uncertainties. This confirms that while classifying clusters based on magnitude and mass gaps at redshift $z > 0$ introduces a bias in mass between the groups, this is not a generic feature of relaxed and unrelaxed halos classified using other structural parameters.

Asymmetry Type	Relaxed $M_{500c}/(10^{14}M_{\odot})$	Unrelaxed $M_{500c}/(10^{14}M_{\odot})$
Total Mass	1.07 ± 0.09	1.00 ± 0.10
Stellar Mass	1.02 ± 0.08	0.94 ± 0.10

Table 4.2: The mean masses and uncertainties of relaxed and unrelaxed halo samples classified based on asymmetry. The halos are at redshift $z = 0.4$ and have a mass threshold $M_{500c} \geq 5{\times}10^{13}\, M_{\odot}$. The halos that are split based on total mass asymmetry were classified as relaxed or unrelaxed analogously to in Figure 4.3. The halos that are split based on stellar mass asymmetry were classified analogously to in Figure 4.4.

We have found that the structural parameters explored in this section generally correlate with the steepness of the surface mass density profiles of clusters, as reflected in their $\Delta\Sigma$ lensing profiles. This is the case for measurements that directly trace the total mass distribution, such as projected centre of mass offset and asymmetry, as well as for optical measurements based on stellar mass and brightness, such as galaxy offset, stellar mass asymmetry and magnitude gap. The projected centre of mass offset and the galaxy offset primarily trace the difference in lensing profiles around 0.2 Mpc to 0.4 Mpc, which is within R_{500c} for clusters of this mass scale. Magnitude and mass gaps best trace the difference in lensing profiles in the innermost radii of clusters. Total mass asymmetry and stellar mass asymmetry evenly trace the difference in lensing profiles from the lowest radii to ~ 0.5 Mpc.

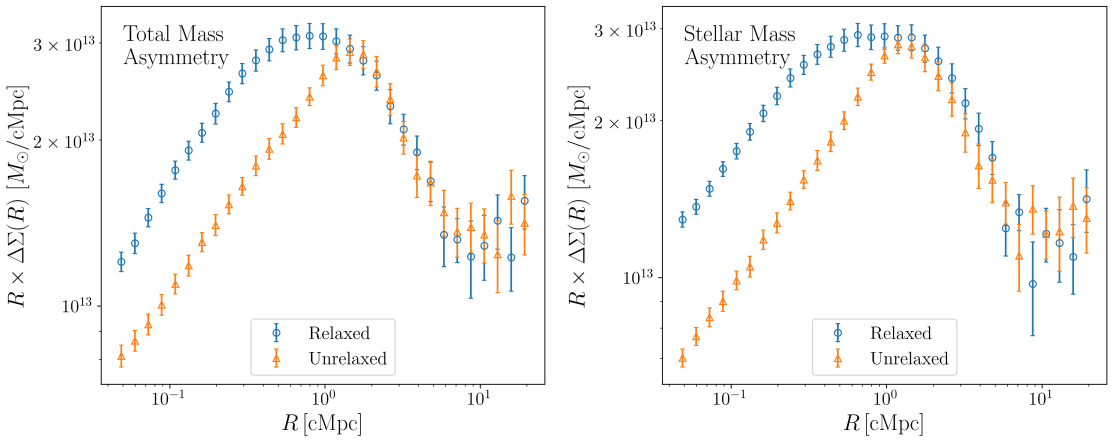


Figure 4.7: The mean lensing profiles $\Delta\Sigma$ for relaxed and unrelaxed halos with mass $M_{500c} \geq 5 \times 10^{13}\, M_\odot$ at redshift $z = 0.4$, classified based on asymmetry in the TNG300-1 simulation. The left panel shows lensing profiles for halos classified based on total mass asymmetry, analogous to the split in Figure 4.3. The right panel shows lensing profiles for halos classified based on stellar mass asymmetry, analogous to the split in Figure 4.4. The points represent the mean lensing signal for the clusters in each group, and the error bars are the uncertainty on the mean.

At redshift $z = 0$, all of the dynamical splits based on structural measurements in this section produced groups whose mean lensing signals converge at larger radii, with the exception of galaxy offset. We note that galaxy offset is the only one of these parameters that was not found to correlate strongly with halo mass accretion history in Chapter 3. We also found that dynamical splits based on magnitude and mass gaps produce a mean cluster mass difference between the relaxed and unrelaxed groups at redshift $z > 0$. This difference in mean mass is not reproduced when halos are instead classified according to total or stellar mass asymmetry. This indicates that magnitude and mass gaps introduce a redshift-dependent bias in cluster mass through their dynamical state classifications. This is explored further in Section 4.4.

4.2 Projection Effects

In this section, we examine the effects of line of sight projection on our simulated cluster sample. We focus particularly on how measurements of the magnitude and mass gaps are affected by galaxies projected into clusters and how that affects the mean structure of dynamically relaxed and unrelaxed systems. We expect that galaxies which appear to be cluster members due to projection along the line of sight may affect the classification of clusters as relaxed or unrelaxed. In particular, a bright galaxy projected into a cluster may decrease the magnitude or stellar mass gap of the cluster and thus make a dynamically relaxed system appear unrelaxed.

In IllustrisTNG simulations, galaxies are identified as part of a cluster when they are within the three-dimensional FoF halo that encompasses a galaxy cluster. Cluster halo and galaxy subhalo definitions are described in more detail in Section 2.1. To project galaxies into a cluster, we first identify the BCG of a real 3D cluster above some mass threshold. We then establish some boundary radius around the BCG for member galaxies. In this section, we take R_{500c} as the boundary radius. We then take all galaxies within R_{500c} tangent to the z-axis and within some projection distance along the z-axis as members of the cluster.

We first aim to understand the difference between the stellar mass functions of dynamically relaxed and unrelaxed clusters due to projection. Before exploring the effects of projection, we must understand the real stellar mass functions of relaxed and unrelaxed clusters, which we classify here based on magnitude gaps. In Figure 4.8, we plot the fraction of the stellar mass in clusters as a function of the stellar masses of their member galaxies for both relaxed and unrelaxed systems. The most notable differences between the relaxed and unrelaxed distributions are that relaxed clusters have a greater fraction of

their stellar mass in high-mass galaxies and that they have a deficit of mid-mass galaxies. Given that our relaxed and unrelaxed samples are selected based on magnitude gaps, these distributions are to be expected. Relaxed clusters are defined to have dominant BCGs, which suggests that they must each have one very bright central galaxy with no other galaxies of similar brightness. This explains why most of their stellar mass is in very high-mass galaxies, with little in mid-mass galaxies. In contrast, unrelaxed clusters are defined to have at least two dominant galaxies of similar brightness. This justifies most of their stellar mass being in galaxies in the intermediate- to high-mass range.

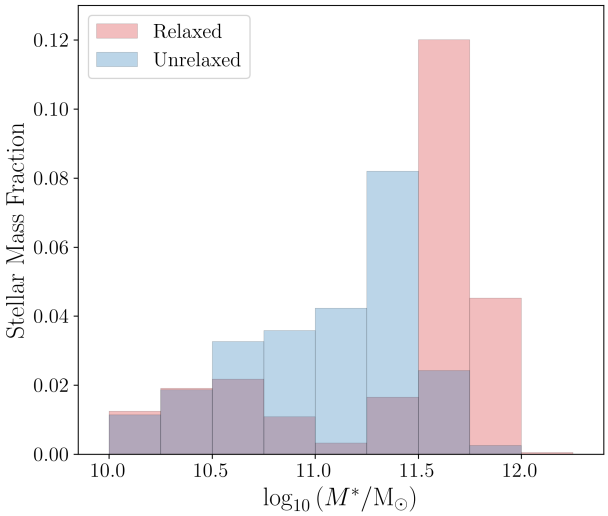


Figure 4.8: The mean fraction of the stellar mass in clusters as a function of member galaxy stellar mass M^* in the TNG300-1 simulation. The clusters have masses $M_{500c} \geq 5\times10^{13}\,M_\odot$ and are at redshift $z = 0$. Galaxy stellar mass is computed within 30 kpc of the most bound particle in each galaxy. The red histogram is data for relaxed clusters, and the blue histogram is for unrelaxed clusters, classified based on magnitude gap. As in Figure 3.23, the 20% of clusters with the greatest magnitude gaps are classified as relaxed and those with the 20% smallest magnitude gaps are classified as unrelaxed.

Having examined the stellar mass fraction distributions for relaxed and unrelaxed clusters, we explore how projected galaxies affect these distributions. In Figure 4.9, we plot the fraction of stellar mass in a cluster as a function of the galaxy stellar mass normalised by the stellar mass of the BCG. This results in the brightest galaxy in each cluster having a mass $M_*/M_{\mathrm{BCG}} = 1$. The blue histograms are the normalised mass fractions for cluster members, while the red histograms represent the added signal from galaxies that would be projected into the clusters across the entire 205 Mpc/h simulation box. In the left panel

of the figure, we plot the mass fractions for dynamically relaxed clusters. As in Figure 4.8, we see that relaxed clusters have a deficit of galaxies with stellar masses comparable to that of their BCGs. The added signal from projected galaxies does not wash out this trend but rather amplifies it. Few high-mass galaxies are projected into the cluster, while many galaxies with stellar masses in the same range as the bump in the distribution are added. In the right panel of Figure 4.9, we plot the mass fractions for dynamically unrelaxed systems. As in Figure 4.8, we see that unrelaxed clusters have many galaxies with stellar masses near those of their BCGs. Once again, the added signal from projected galaxies largely amplifies the existing distribution rather than washing out the trend.

Based on the colours of galaxies that are projected into clusters in Figure 3.24, we concluded in Section 3.5 that most of the galaxies that are projected into the inner regions of clusters are part of the outer regions of those same clusters. Compared to cluster members, relatively few field galaxies are projected within R_{500c} of any given system. This conclusion explains the contributions to the stellar mass distributions from the projected galaxies in Figure 4.9. The projected galaxies amplify the features of the distribution rather than washing them out because the galaxies are not drawn from a random distribution that we might expect in the field. Rather, they are part of the outer regions of the same dynamically relaxed or unrelaxed clusters. However, we note that the amplification to the stellar mass fraction in the highest mass bins in Figure 4.9 is not proportional to the signal in those bins for either relaxed or unrelaxed systems. This indicates that it is unlikely for any galaxy that is projected into the radius R_{500c} of a cluster to have a mass very similar to that of the BCG.

Observations of galaxy clusters are often affected by projection due to poor constraints on line of sight distances from redshift measurements. In order to properly compare our simulated clusters to real systems, we must determine how the results of our dynamical classifications based on magnitude and mass gaps in Section 4.1 are affected by projection. To do so, we first computed the magnitude and mass gaps of clusters at redshift $z = 0.4$ using only galaxies within a three-dimensional radius R_{500c}. We classified these clusters as relaxed or unrelaxed using splits analogous to those in Figure 4.5, and we computed the mean lensing profiles around the clusters in those groups. We then recomputed the magnitude gaps of clusters using all of the galaxies in the simulation that are projected into R_{500c} along the z-axis. We classified the clusters as relaxed or unrelaxed based on these projected magnitude gaps, and we computed the mean lensing profiles around clusters in those groups. The mean lensing profiles around relaxed and unrelaxed clusters classified in 3D and in projection are compared in Figure 4.10. We see in the figure that the mean lensing profiles for the clusters in each group are nearly unaffected by projection. There is very little deviation between the profiles in the inner regions of halos, at the peaks of the

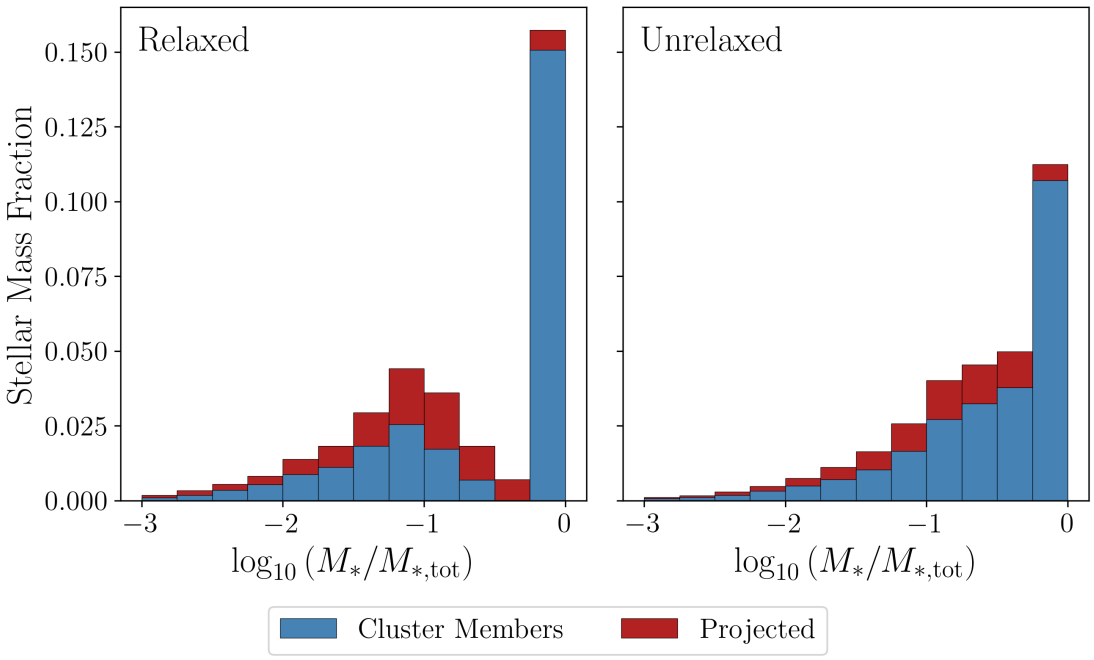


Figure 4.9: The mean fraction of the stellar mass in clusters as a function of galaxy stellar mass M_* relative to the total stellar mass of galaxies in the parent cluster $M_{*,\mathrm{tot}}$ in the TNG300-1 simulation. The clusters have masses $M_{500c} \geq 5 \times 10^{13}\, M_\odot$ and are at redshift $z = 0$. Galaxy stellar mass is computed within 30 kpc of the most bound particle in each galaxy. The blue histogram is normalised and computed from galaxies that are within R_{500c} of the halo in 3D. The red histogram is the added signal from galaxies that would be projected into R_{500c} for each cluster along the z-axis across the entire 205 Mpc/h length simulation box. The left panel is data for relaxed clusters, and the right panel is for unrelaxed clusters. As in Figure 3.23, the 20% of clusters with the greatest magnitude gaps are classified as relaxed and those with the 20% smallest magnitude gaps are classified as unrelaxed.

lensing signal, or even in the environments outside the halos at large radii.

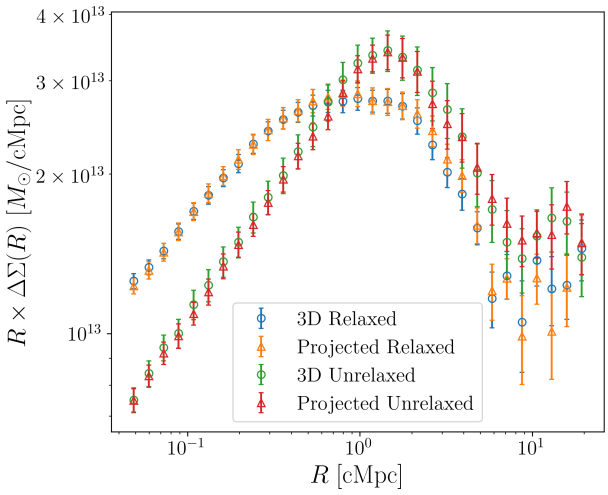


Figure 4.10: The mean lensing profiles $\Delta\Sigma$ for the relaxed and unrelaxed halos, classified based on the magnitude gaps of 3D and projected member galaxies in the TNG300-1 simulation. The profiles are computed for clusters at redshift $z = 0.4$ with masses $M_{500c} \geq 5 \times 10^{13}\, M_\odot$. The 3D sample is split based on magnitude gaps as in Figure 4.5. The projected sample is split analogously, with magnitude gaps computed from all galaxies across the simulation box that are projected into R_{500c} along the z-axis for each cluster. The points represent the mean lensing signal for the clusters in each group, and the error bars are the uncertainty on the mean.

We have found that the projection of galaxies into clusters along the line of sight does not significantly affect our classification of clusters as dynamically relaxed or unrelaxed. From the stellar mass fractions of clusters as a function of galaxy stellar mass in Figure 4.9, we see that the galaxies projected into clusters do not greatly alter the mass distributions of cluster members. Since the lensing profiles in Figure 4.10 are consistent whether the halos are classified based on 3D or projected magnitude gaps, we conclude that projected galaxies do not significantly affect our relaxed and unrelaxed categorisation of galaxy clusters based on magnitude gaps.

4.3 Cluster Selection

In Chapter 3, we show that one can use structural measurements of halos to predict the recent mass accretion histories of galaxy clusters. In Section 4.1, we showed that the same classifications of simulated clusters based on optical measurements can produce samples with different gravitational lensing profiles. In order to test the applicability of these techniques outside of the TNG300-1 simulation, we compare them to a cross-matched cluster sample from the DLIS (Dey et al., 2019) and the UNIONS (Gwyn et al., 2025) surveys in Section 4.4. In this section, we prepare for the comparison of IllustrisTNG results with DLIS x UNIONS results by selecting simulated clusters analogously to how they are selected from observational surveys. The DLIS cluster catalogue used in this work is developed by Wen & Han (2024). They outline their selection method for clusters based on the observed distribution of galaxies in Wen & Han (2024), which we replicate here in IllustrisTNG.

To build their cluster catalogue, Wen & Han (2024) first identified BCG candidates as any galaxies with stellar masses $M_* \geq 1 \times 10^{11}\, M_\odot$. They then used colour criteria to exclude massive galaxies that are not likely cluster BCGs. In particular, they compared the z- and W1-band magnitudes of their BCG candidates to those of known BCGs and excluded any galaxy with magnitudes inconsistent with those of the known BCGs. In IllustrisTNG, we do not have access to the W1-band magnitudes of stellar particles. The K-band is the longest available wavelength band in the simulation, and it is the most comparable to the W1-band. As a result, we make cuts to the BCG candidates in the TNG300-1 simulation that are similar to those by Wen & Han (2024) based on the z- and K-band magnitudes of galaxies. In Figure 4.11, we show the distributions of real BCG magnitudes in red and the BCG candidate magnitudes in black at two different redshifts. The green dashed lines represent the colour thresholds we put on the BCG candidates based on the colours of confirmed BCGs. We only accept BCG candidates with magnitudes below the green dashed lines, analogously to what was done by Wen & Han (2024).

Once the BCG candidates have been identified and selected based on their magnitudes, Wen & Han (2024) then estimate the radius R_{500c} around the BCGs. The radius R_{500c} is calculated based on the stellar mass enclosed within the following radius around the BCG:

$$r_1 = 1.0\, E(z)^{-2/3}\, \mathrm{Mpc}\,, \tag{4.1}$$

where $E(z) = \sqrt{\Omega_\Lambda + \Omega_m\,(1+z)^3}$ is the dimensionless Hubble parameter and z is the redshift of the BCG. Wen & Han (2024) only use galaxies with masses $M_* \geq 10^{10}\, M_\odot$ as cluster members since they have more precise redshift measurements. As a result, the

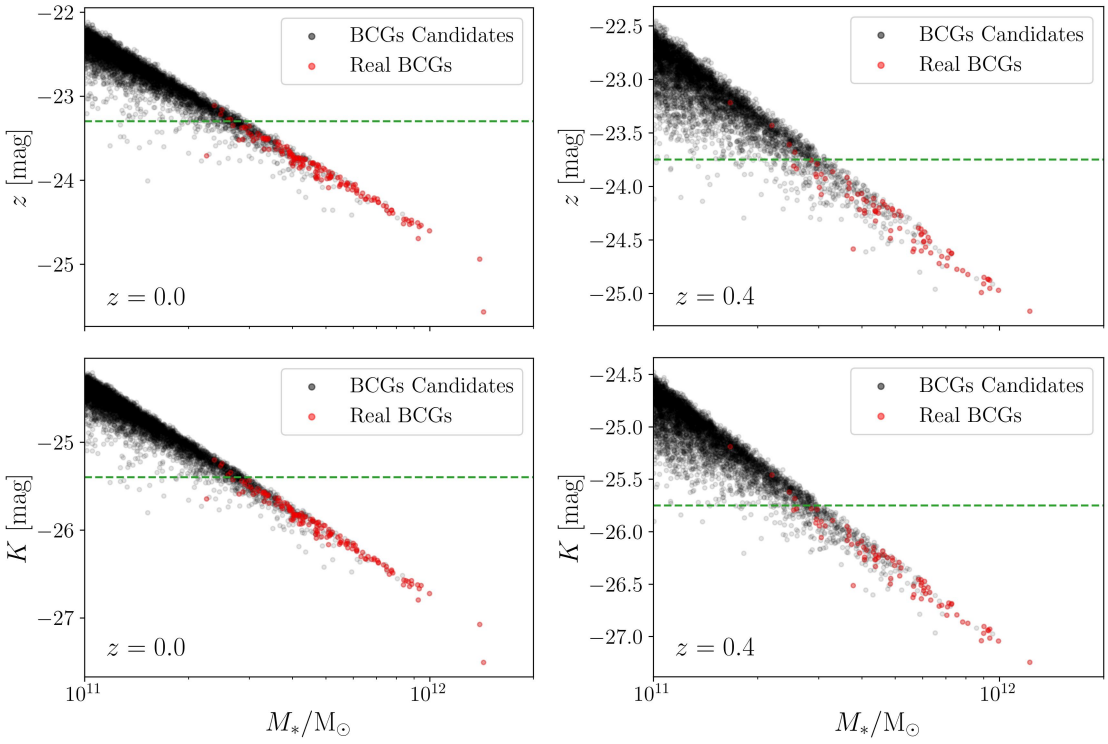


Figure 4.11: The z- and K-band magnitudes of galaxies as a function of stellar mass within a 30 kpc aperture in the TNG300-1 simulation. The left two panels are galaxies at redshift $z = 0$, while the right two are at redshift $z = 0.4$. The red points represent the brightest galaxies in clusters of mass $M_{500c} \geq 1 \times 10^{14}\, M_{\odot}$. The black points are all other galaxies above a $M_{*} \geq 1 \times 10^{11}\, M_{\odot}$ stellar mass threshold. The dashed green lines represent the magnitude thresholds applied to possible BCG candidates in the given photometric bands at the given redshifts.

stellar mass enclosed within r_1 is taken only from the masses of these galaxies. The radius R_{500c} is estimated from the stellar mass $M_{*,r1}$ within the radius r_1 using the scaling relation:

$$\log_{10}\left(R_{500c}\right) = 0.402\log_{10}\left(\frac{M_{*,r1}}{10^{10}\,M_{\odot}}\right) - 0.944 + 0.43\log_{10}(1+z)\,. \tag{4.2}$$

Using the computed radius R_{500c}, the stellar mass within that radius $M_{*,500c}$ is then computed by summing the stellar masses of all galaxies within that radius around the BCG. From the stellar mass, the total mass of the halo M_{500c} is estimated using the stellar-to-halo mass relation:

$$\log_{10}\left(M_{500c}\right) = 0.96\log_{10}\left(M_{*,500c}\right) - 1.86 + 0.2\log_{10}(1+z)\,, \tag{4.3}$$

as is given in Wen & Han (2021). Once the radii and masses of the clusters have been computed, the least massive of any two clusters within $1.5\,R_{500c}$ of each other is removed from the sample to prevent double counting. Finally, Wen & Han (2024) impose that each cluster must contain at least 6 member galaxies within R_{500c}. The analyses in this work impose the stricter criteria that each cluster must have at least 10 member galaxies and must have some minimum mass M_{500c} specified for each sample.

All of these procedures used to generate the DLIS catalogue by Wen & Han (2024) are replicated in this work for the TNG300-1 simulated clusters. We use the same restriction on galaxy stellar mass $M_* \geq 1 \times 10^{10}\,M_{\odot}$, and we compute our stellar masses from the stellar particles within 30 kpc of the galaxy centre. This choice of radius around galaxy centres is justified in Section 2.3.5. The spatial distribution of clusters selected from the projected galaxy distribution in the TNG300-1 simulation is shown in Figure 4.12. As expected, we see that clusters are concentrated in regions of dense structure.

There is a notable difference between the observational and simulation selection methods regarding line of sight distances. The cluster members around the BCG identified by Wen & Han (2024) are within photometric redshift slices $z \pm 0.04\,(1+z)$ for $z \leq 0.7$. Given that each simulation snapshot in IllustrisTNG is at one particular and well-known redshift, we take all galaxies within some distance along the line of sight from the BCG to approximate the projection effect of using photometric redshifts. Unless otherwise stated, all results in this work using optical cluster selection take all galaxies within ± 50 cMpc of the BCG along the line of sight to be members of the cluster. To determine how significantly projected galaxies affect our cluster sample, we use the 3D simulation information to compute what fraction of the stellar mass in an optically identified cluster is a part of the true underlying FoF halo. To do this in IllustrisTNG, we identify the parent halo of each galaxy in an optically identified cluster. From the resulting list of parent halos,

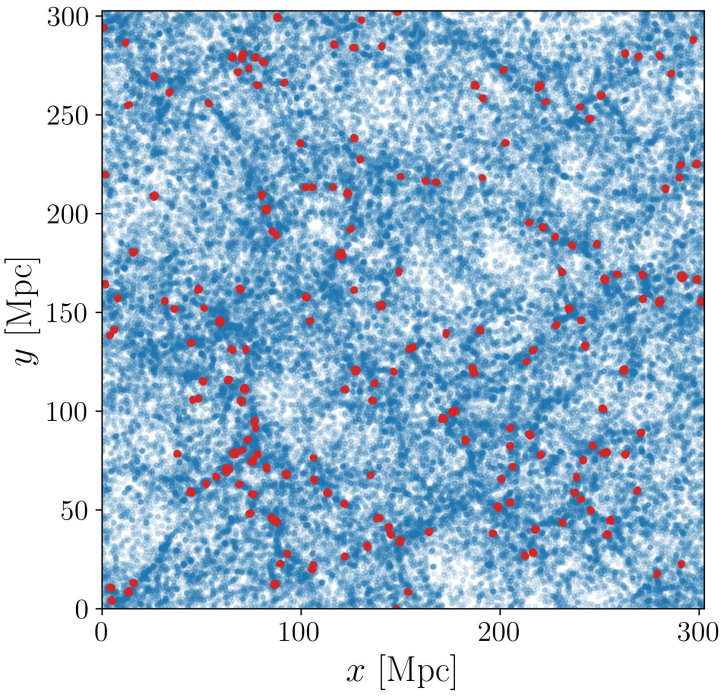


Figure 4.12: The projected spatial distribution of massive galaxies and optically identified clusters in the TNG300-1 simulation. The blue points represent galaxies with stellar masses $M^* \geq 1 \times 10^{10}\, M_\odot$ within a 30 kpc aperture around the most bound particle. The red points represent clusters with estimated masses $M_{500c} \geq 1 \times 10^{14}\, M_\odot$ that were optically identified from the galaxy distribution using the selection method adapted from Wen & Han (2024).

we identify which halo contains the majority of the stellar mass in the optically identified cluster, and we consider it the main halo. We can then take the ratio of the stellar mass in the main halo to the total stellar mass in the optically identified cluster. In Figure 4.13, we plot the cumulative distribution function of the fraction of stellar mass in the main halo for our optically selected sample. The left panel of the figure shows the results for the simulation snapshot at redshift $z = 0$, and the right panel shows the results for $z = 0.4$. We see that at both redshifts, approximately 90% of optically selected clusters have at least 80% of their identified stellar mass in the main 3D halo. This quantifies the significance of projection in these systems with 50 cMpc line of sight distances from the BCG.

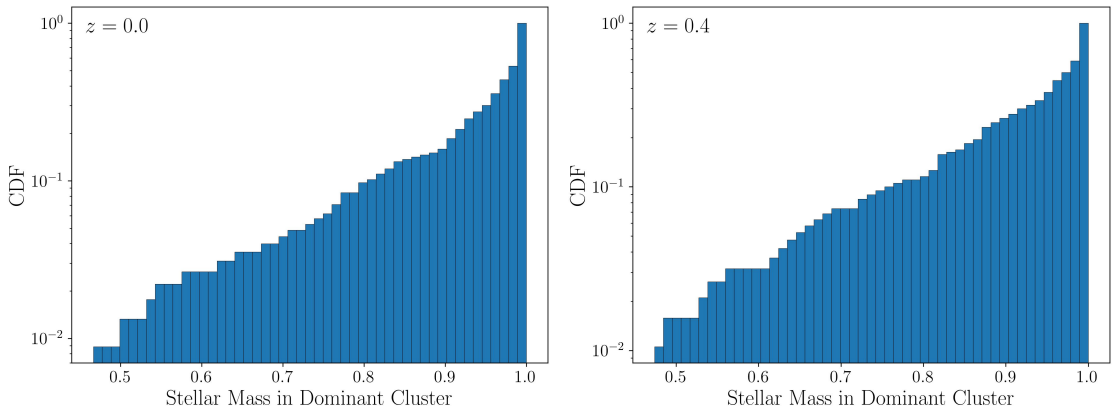


Figure 4.13: The cumulative distribution function of the fraction of stellar mass in optically selected clusters that is a part of the true 3D clusters to which they correspond in the TNG300-1 simulation. For a galaxy to be considered part of the true 3D cluster corresponding to an optically selected cluster, it has to be within the 3D friend-of-friends halo that contains the greatest fraction of the mass of the optically selected cluster members. The left panel shows the data at redshift $z = 0.0$, while the right panel is at redshift $z = 0.4$.

As a greater line of sight depth around the BCG is taken, a greater fraction of the stellar mass in the optical clusters is from projected galaxies rather than true halo members. In Figure 4.14, we plot the mean fraction of the stellar mass in the main halo as a function of the line of sight depth around the BCG. For each data point used to construct the curves in Figure 4.14, we developed a new optically selected cluster sample using the specified line of sight depth. We see that at a depth of 50 cMpc, the mean stellar mass in the dominant halo is $\sim 93\%$ at redshift $z = 0.4$. We see that even if we project all of the galaxies in the simulation box, which results in a line of sight depth of ~ 150 cMpc, the mean fraction of the stellar mass that is in the dominant halos is above 85%.

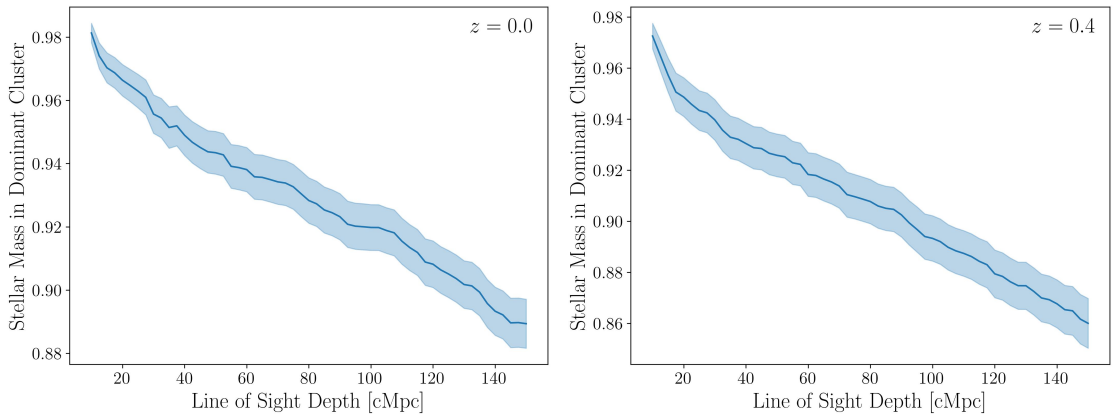


Figure 4.14: The mean fraction of stellar mass in optically selected clusters that is part of the true 3D clusters to which they correspond, as a function of line of sight depth around the BCG in the TNG300-1 simulation. Clusters are optically identified using the selection method adapted from Wen & Han (2024) with some maximum depth along the line of sight around the BCG within which galaxies are considered part of the cluster. For a galaxy to be considered part of the true 3D cluster corresponding to an optically selected cluster, it has to be within the 3D friend-of-friends halo that contains the greatest fraction of the mass of the optically selected cluster members. The thin blue line is the mean fraction of stellar mass within the true 3D cluster for the optically selected clusters with estimated masses $M_{500} \geq 1 \times 10^{14}\, M_{\odot}$. The pale blue region is the standard error on the mean. The left panel shows the data at redshift $z = 0.0$, while the right panel is at redshift $z = 0.4$.

A greater projected line of sight depth around the BCG of a cluster results in more galaxies being considered members of that cluster. Consequently, a greater line of sight depth results in more optically identified clusters exceeding the minimum threshold for the number of member galaxies. From Equation 4.3, we see that the estimated mass of a halo M_{500c} is based on the stellar mass of galaxies within the halo $M_{*,500c}$. As a result, a greater line of sight depth, which includes more member galaxies, will increase the estimated mass of the cluster. This causes more optically identified clusters to exceed the minimum mass threshold. These two factors cause greater line of sight depths around BCGs to produce larger catalogues of optically selected clusters. In Figure 4.15, we plot the number of identified clusters in the TNG300-1 simulation as a function of line of sight depth. We see that for both the $z = 0$ and $z = 0.4$ redshift snapshots, the number of identified clusters increases by ~ 0.25 clusters/cMpc of depth.

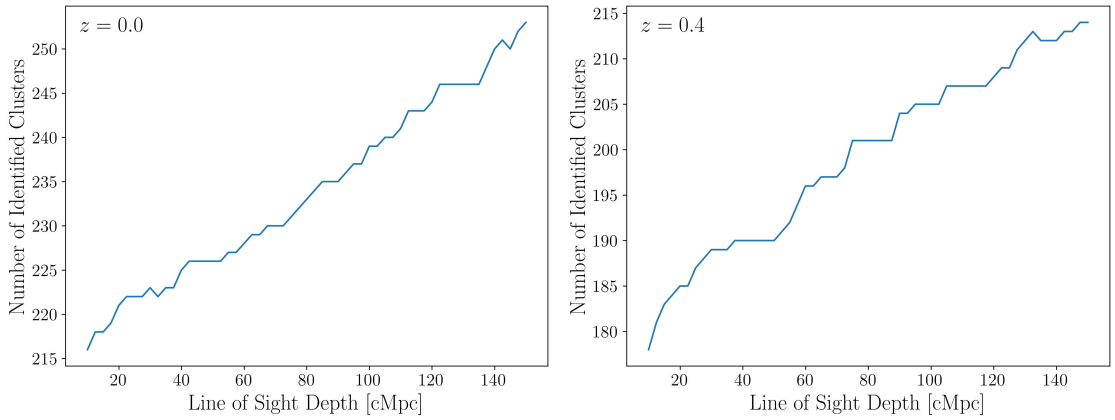


Figure 4.15: The number of optically selected clusters with estimated masses $M_{500} \geq 1{\times}10^{14}\, M_{\odot}$ as a function of line of sight depth around the BCG in the TNG300-1 simulation. Clusters were optically identified using the selection method adapted from Wen & Han (2024) with some maximum depth along the line of sight around the BCG within which galaxies are considered part of the cluster. The left panel shows the data at redshift $z = 0.0$, while the right panel is at redshift $z = 0.4$.

In order to compare the structure of the optically identified clusters to the FoF halos in the TNG300-1 simulation, we plot their respective mean gravitational lensing profiles in Figure 4.16. The clusters identified by IllustrisTNG in 3D using their FoF algorithm are labelled as "real clusters", and those identified optically using the adapted Wen & Han (2024) scheme are labelled "W&H Clusters". Both samples of clusters have a minimum cluster mass of $M_{500c} \geq 1 \times 10^{14}\, M_{\odot}$, as is indicated in the legend. We see in the left panel

that at redshift $z = 0$, the lensing signal around real clusters is greater than that around optical clusters. In the right panel of Figure 4.16, we see that the disparity is much greater at redshift $z = 0.4$, particularly at the peak of the lensing profiles.

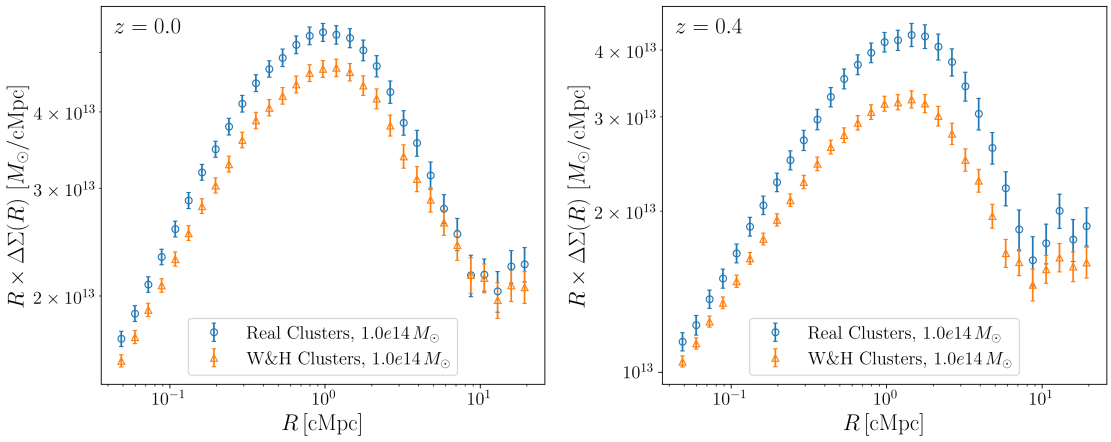


Figure 4.16: The mean gravitational lensing profiles $\Delta\Sigma$ for 3D identified clusters and optically identified clusters at redshifts $z = 0.0$ and $z = 0.4$ in the TNG300-1 simulation. The profiles labelled as real clusters are identified in 3D using IllustrisTNG's FoF algorithm. These clusters have masses $M_{500c} \geq 1 \times 10^{14}\, M_\odot$, computed from the 3D particle distribution. The profiles labelled as W&H clusters are optically identified from the projected galaxy distribution using the method adapted from Wen & Han (2024). These clusters have estimated masses $M_{500} \geq 1 \times 10^{14}\, M_\odot$ based on Wen & Han's method. The points represent the mean lensing signal for the clusters in each group, and the error bars are the uncertainty on the mean.

This difference in the amplitudes of the $\Delta\Sigma$ curves for real and optically selected clusters suggests that the samples contain halos with different mean masses. Both samples have a minimum mass threshold of $M_{500c} \geq 1 \times 10^{14}\, M_\odot$, but the ways in which their halo masses were computed are different. The masses of the real clusters are based on the M_{500c} masses reported in the TNG300-1 halo catalogue. Those masses are based on the FoF halo mass distribution in 3D. The masses of the optically selected clusters are estimated based on the stellar masses of galaxies projected around the BCG using Equations 4.1, 4.2 and 4.3 as described in Wen & Han (2024). As is illustrated in Figures 4.14 and 4.15, the optically selected clusters may overestimate the masses of halos from the stellar-to-halo mass relation due to the projection of galaxies into the cluster along the line of sight. The difference between these definitions of mass may account for the differences in the lensing profiles in Figure 4.16. To confirm whether a mass difference between the samples accounts for

the difference in the lensing profiles, we adjusted the minimum mass threshold of the real cluster sample until the lensing profiles at each redshift best fit the optically selected cluster profiles. The results of this process are shown in Figure 4.17. We see in the left panel that, at redshift $z = 0$, real clusters with a mass threshold $M_{500c} \geq 7.5 \times 10^{13}\, M_{\odot}$ have a mean lensing profile that matches that of the optically selected clusters with estimated masses $M_{500c} \geq 1 \times 10^{14}\, M_{\odot}$. The lensing profiles deviate slightly at radii above a few cMpc, which suggests that the optically selected clusters exist in slightly denser environments than the real clusters, on average. We see in the right panel of Figure 4.17 that at redshift $z = 0.4$, real clusters with a minimum mass $M_{500c} \geq 6 \times 10^{13}\, M_{\odot}$ have a mean lensing profile that matches that of the optically selected clusters. This is a notably lower mass threshold than is required at redshift $z = 0$. We saw in Figure 4.14 that the increase in apparent mass of an optically selected cluster due to projection is only slightly greater at redshift $z = 0.4$ compared to $z = 0$. This suggests that the difference in optically selected cluster mass between $z = 0.0$ and $z = 0.4$ is due to more than just projection. There is a correlation with redshift that is not fully captured in the R_{500c} or M_{500c} scaling relations from Equations 4.2 and 4.3.

We have established that the optically selected clusters have very similar mean lensing profiles to real clusters in IllustrisTNG, albeit with a lower mean mass than what is estimated based on scaling relations. Given the similar projected radial mass structure of the clusters, we determine whether classifying the optical clusters as dynamically relaxed or unrelaxed based on optical properties produces comparable lensing profiles to real clusters as well. We classified the optically selected sample into dynamically relaxed and unrelaxed groups using the magnitude and mass gaps of their projected member galaxies, analogously to how it is done in Figure 4.5. We then compared the mean lensing profiles of the two groups to those of the similarly classified relaxed and unrelaxed groups of the 3D halos. Once again, the minimum mass threshold of the real clusters was adjusted so as to best fit the peaks of the lensing profiles of the optically selected clusters. The resulting mean gravitational lensing profiles are shown for the redshift $z = 0.4$ snapshot in Figure 4.18. We note that the real clusters have masses $M_{500c} \geq 7 \times 10^{13}\, M_{\odot}$, which is greater than the best-fit mass threshold at the same redshift in Figure 4.17. This indicates that the scaling relations used to estimate the masses of the optically selected clusters do not produce consistent mass estimates for relaxed and unrelaxed compared to the rest of the sample. Despite the estimated mass difference, the mean lensing profiles of the optically selected clusters are very similar to those of the real clusters for both relaxed and unrelaxed systems. The optically selected unrelaxed clusters have a slightly stronger signal in the core compared to the real unrelaxed clusters, but the difference is within 1σ. This slight discrepancy may be due to greater projection effects in the optically selected sample,

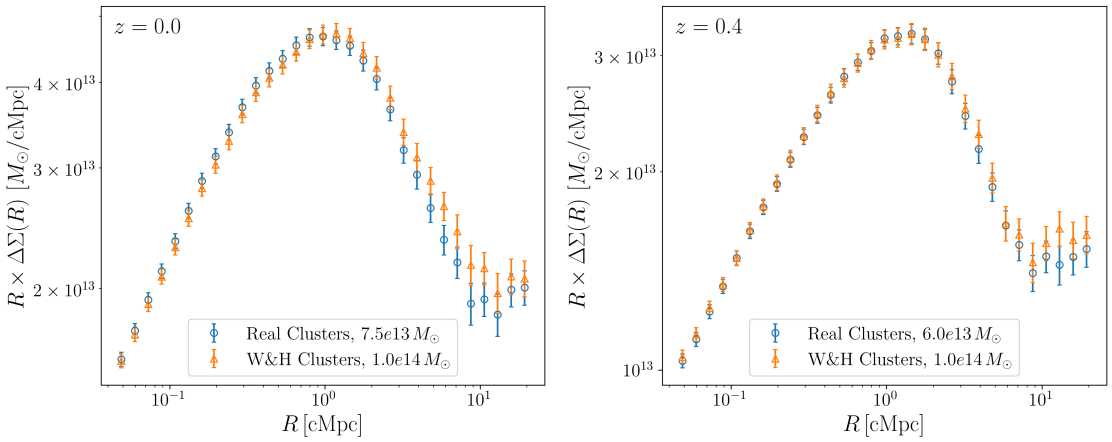


Figure 4.17: The mean lensing profiles $\Delta\Sigma$ for 3D identified clusters and optically identified clusters at redshifts $z = 0.0$ and $z = 0.4$ in the TNG300-1 simulation. The profiles labelled as W&H clusters are optically identified from the projected galaxy distribution using the method adapted from Wen & Han (2024). These clusters have estimated masses $M_{500} \geq 1 \times 10^{14}\,M_\odot$ based on Wen & Han's method. The profiles labelled as real clusters are identified in 3D using IllustrisTNG's FoF algorithm. The clusters have masses computed from the 3D particle distribution, and a minimum mass indicated by the axis labels. These minimum masses were chosen so as to fit the W&H lensing profiles. The points represent the mean lensing signal for the clusters in each group, and the error bars are the uncertainty on the mean.

resulting in some more relaxed systems being classified as unrelaxed due to the projected galaxies.

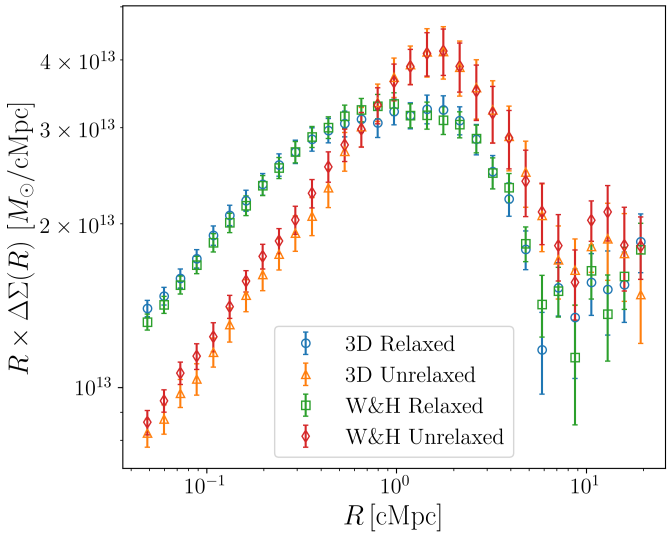


Figure 4.18: The mean lensing profiles $\Delta\Sigma$ for 3D identified clusters and optically identified clusters at redshift $z = 0.4$, split into dynamically relaxed and unrelaxed groups in the TNG300-1 simulation. The profiles labelled as W&H clusters are optically identified from the projected galaxy distribution using the method adapted from Wen & Han (2024). These clusters have estimated masses $M_{500} \geq 1 \times 10^{14}\, M_\odot$ based on Wen & Han's method. The profiles labelled as real clusters are identified in 3D using IllustrisTNG's FoF algorithm. The cluster masses $M_{500c} \geq 7 \times 10^{13}\, M_\odot$ are computed from the 3D particle distribution. This minimum mass was chosen so as to fit the W&H lensing profiles. The real and optically selected clusters were split into relaxed and unrelaxed groups based on magnitude gaps, analogously to Figure 4.5. The points represent the mean lensing signal for the clusters in each group, and the error bars are the uncertainty on the mean.

In this section, we established how to select cluster samples from an IllustrisTNG simulation based on the optical selection method used for an observational survey by Wen & Han (2024). These optically selected clusters provide a better analogue to the systems identified in observational data than the FoF halos often provided by simulations. We explored the effects of projection along the line of sight on the mass content of optically selected clusters. We found that a minority of systems have a significant amount of their stellar mass misattributed to the cluster due to projection. Additionally, we found that the scaling relations established by Wen & Han (2024) tend to overestimate the masses of

clusters in IllustrisTNG. These overestimations are a function of redshift that cannot be due only to the projection of galaxies. However, with corrected minimum mass thresholds of our samples, optically selected clusters produce gravitational lensing profiles that are consistent with those of clusters identified from the 3D particle distributions. Additionally, classifying optically selected clusters as dynamically relaxed and unrelaxed based on magnitude and mass gaps creates groups of systems with mean lensing profiles consistent with those of real clusters classified in the same way.

4.4 DLIS x UNIONS Collaboration

We established in Sections 4.1 that we can identify dynamically relaxed and unrelaxed halos in simulations based on their magnitude gaps. We showed that these different groups of halos have different mean mass structures reflected in their gravitational lensing profiles. In Section 4.3, we optically selected galaxy clusters from the IllustrisTNG simulation data analogously to how clusters are identified in observational surveys. With some mass corrections, the optically selected clusters have a similar structure to real halos, and they can be split dynamically to the same effect. In this section, we will compare these results from the TNG300-1 simulation to an observational catalogue from DLIS produced by Wen & Han (2024). All of the work done directly on DLIS and UNIONS data presented here was performed and compiled by my collaborators, Syeda Lammim Ahad and Charlie Mpetha, whose contributions are highlighted throughout this section.

We first describe the galaxy cluster catalogue to which we are comparing the IllustrisTNG clusters. The initial catalogue of 1.58 million DLIS clusters was produced by Wen & Han (2024), whose selection methods are described in Section 4.3. S. Ahad [Ahad et al. in prep] cross-matched this catalogue with the weak lensing shear catalogue from UNIONS (Gwyn et al., 2025). She then further cut the catalogue to include only clusters with at least 10 member galaxies and whose BCG has a spectroscopic redshift measurement. This reduced the sample to 51619 clusters. Ahad classified these clusters as dynamically relaxed or unrelaxed groups based on their magnitude and mass gaps. The results of this classification are shown in Figure 4.19, where the relaxed and unrelaxed groups each account for approximately 10% of the total sample. We see in the left panel of Figure 4.19 that the distribution of r- and g-band magnitude gaps for the observed clusters looks quite different to those seen in IllustrisTNG in Figures 3.23 and 4.5. In IllustrisTNG, the r- and g-band magnitudes of galaxies in massive clusters are almost degenerate because they are all red sequence galaxies, as is explained in Section 3.25. This is clearly not the case for the observed clusters in Figure 4.19. The discrepancy between these distributions may be

due to IllustrisTNG's stellar evolution model or to measurement and photometric redshift uncertainties in the DLIS cluster catalogue. In addition to the difference in the magnitude gap distributions, the splits in magnitude and mass gap required to select the most relaxed and unrelaxed systems in Figure 4.19 are quite different from those used for IllustrisTNG clusters throughout this work. While we acknowledge these differences in the optical properties of the simulated and observed galaxy clusters, the dynamical splits made in Figure 4.19 and in the IllustrisTNG data both serve to identify the most dynamically relaxed and disturbed clusters based on the same optical properties of similarly selected samples.

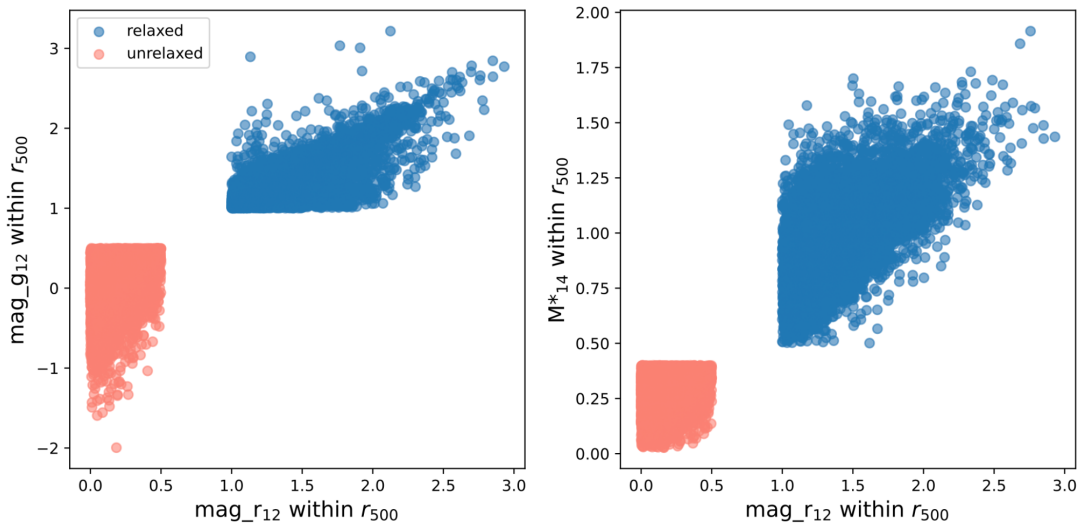


Figure 4.19: The magnitude and mass gaps of galaxies within R_{500} for clusters in the DLIS catalogue developed by Wen & Han (2024), split into relaxed and unrelaxed groups by S. Ahad [Ahad et al. in prep]. The "mag_r$_{12}$" axis represents the magnitude gap between the two brightest galaxies in the r-band. The "mag_g$_{12}$" axis represents the g-band magnitude gap between the same two galaxies. The "M$^*_{14}$" axis represents the difference in $\log_{10}$(Stellar Mass) of the first and fourth most massive subhalos. The relaxed and unrelaxed groups each contain $\sim 10\%$ of the clusters in the total sample. Figure produced by S. Ahad.

In order to best compare the IllustrisTNG clusters to the observational sample produced by Ahad, we must understand the distribution of masses and redshifts of the observed clusters. In Figure 4.20, Ahad plotted these distributions for the relaxed and unrelaxed cluster samples defined in Figure 4.19. We see in the left panel of Figure 4.20 that the

distributions of cluster masses for the relaxed and unrelaxed groups are consistent with each other. From the decrease in cluster counts at the low-mass end of the distribution, we conclude that the survey loses sensitivity at halo masses $M_{500c} \lesssim 1 \times 10^{14}\, M_{\odot}$. In the right panel of Figure 4.20, we see that the redshift distributions of the two groups are similar, though unrelaxed clusters have a slightly higher mean redshift. The mean redshift of the relaxed clusters is $z \simeq 0.4$, and that of the unrelaxed clusters is $z \simeq 0.5$. This difference in mean redshift is likely due to the fact that massive halos at higher redshift have had less time to dynamically relax after forming, resulting in a greater fraction of massive halos at high redshift being unrelaxed.

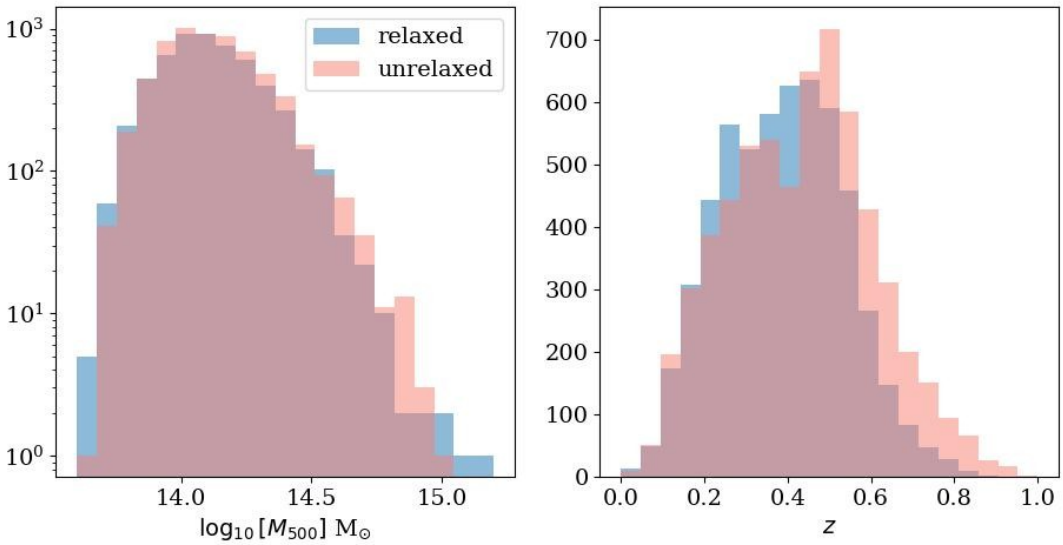


Figure 4.20: The distributions of stellar masses and redshifts of clusters in the DLIS catalogue developed by Wen & Han (2024), split into relaxed and unrelaxed groups by S. Ahad [Ahad et al. in prep]. The relaxed and unrelaxed groups are classified based on magnitude and mass gaps as in Figure 4.19. The left panel shows the distribution of M_{500} cluster masses for each group as estimated by Wen & Han (2024). The right panel shows the distribution of redshifts z for the BCG of each group. The dependent axes are the number of clusters in each bin. Figure produced by S. Ahad.

To compare the projected radial mass structure of dynamically relaxed and unrelaxed halos in IllustrisTNG, we have compared their mean gravitational lensing profiles. In order to compare the structure of the IllustrisTNG halos to those in the observational sample, we do the same for the observed clusters. The lensing profiles for the DLIS catalogue compiled

by Ahad are computed by C. Mpetha [Mpetha et al. in prep] from the UNIONS LSB shear catalogue (Gwyn et al., 2025). The resulting $\Delta\Sigma$ profiles for the relaxed and unrelaxed clusters defined in Figure 4.19 are shown in Figure 4.21. We see that the relaxed halos have a considerably stronger lensing signal in the inner regions, as we saw for the simulated halos in Section 4.1. The lensing profiles of the relaxed and unrelaxed groups converge at radii greater than $\sim 1.5\,\mathrm{cMpc}$, which suggests that the groups are of similar mean mass. Mpetha fit the lensing profiles in Figure 4.21 using a Markov Chain Monte Carlo (MCMC) and found that the relaxed group has a mean mass of $M_{500c} = 1.43 \times 10^{14}\,M_\odot$, while the unrelaxed group has a mean mass of $M_{500c} = 1.45 \times 10^{14}\,M_\odot$. This is notably different from the results of Section 4.1, where we found that clusters classified based on magnitude gap in IllustrisTNG at the average redshift of this sample have significantly more massive unrelaxed clusters than relaxed clusters.

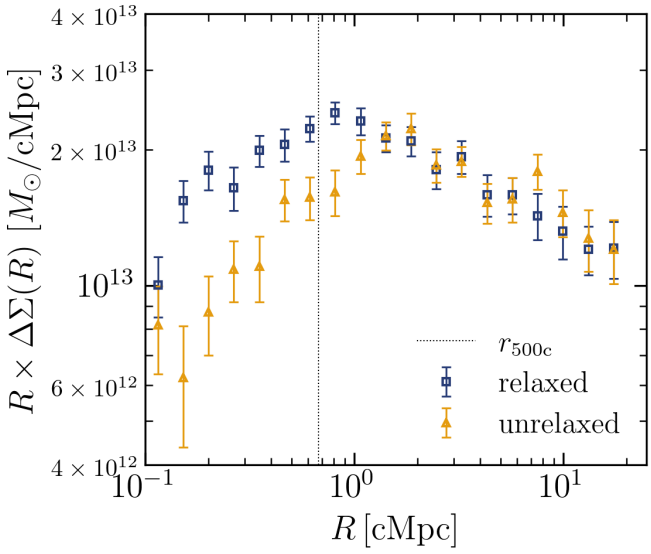


Figure 4.21: The lensing profiles $\Delta\Sigma$ of stacked clusters in the DLIS catalogue developed by Wen & Han (2024), split into relaxed and unrelaxed groups by S. Ahad [Ahad et al. in prep]. The relaxed and unrelaxed groups split based on magnitude gaps, as in Figure 4.19. The points represent the lensing signal at each radius computed from the UNIONS shear catalogue (Gwyn et al., 2025), and the error bars are the uncertainties on the signal. The figure and all results shown were produced by C. Mpetha [Mpetha et al. in prep].

To directly compare the dynamically split lensing profiles in IllustrisTNG and the DLIS x UNIONS catalogue compiled by Ahad and Mpetha, we first produced a simulated cluster

sample with the same mean mass and redshift as the observed cluster sample. By fitting the stacked lensing profiles of the observed clusters with MCMC, Mpetha found the mean mass of the sample to be $M_{500c} = 1.44 \times 10^{14}\, M_{\odot}$. We note that this is significantly lower than the mean mass presented in the cluster mass distribution in Figure 4.20. This is because Mpetha's MCMC fits to the lensing profiles found that the catalogue by Wen & Han (2024) overestimates the masses of the clusters. Given that we found similar overestimates of cluster masses using optical selection in Section 4.3, and given that Mpetha was able to recover the simulated halo masses from fits to their lensing profiles, we consider the cluster mass estimates from the lensing profiles robust. By taking a lower mass limit of $M_{500c} \geq 7.5 \times 10^{13}\, M_{\odot}$ for the IllustrisTNG clusters, we produce a sample with the same mean mass as the observational sample. With reference to the redshift distributions of the observed clusters in Figure 4.20, we chose the IllustrisTNG simulation snapshot at redshift $z = 0.4$ for our cluster sample. We then classify the halos as dynamically relaxed and unrelaxed, as was done in Figure 4.5. The resulting lensing profiles of the IllustrisTNG clusters are compared to those from the DLIS x UNIONS catalogue in Figure 4.22.

There are several notable differences between the simulated and observed gravitational lensing profiles in Figure 4.22. Firstly, the simulated sample's lensing signals are significantly higher than the observed sample's lensing signals for both the relaxed and the unrelaxed clusters. This would typically indicate that the simulated sample has a greater mean mass than the observed sample. However, the mean masses of the samples were specifically selected to be the same. In his MCMC fitting of the lensing profiles for these systems, Mpetha found that the lower amplitude of the observed sample's signal may be due to significant miscentering on the observed clusters. Secondly, the relaxed and unrelaxed groups of observed clusters clearly have the same mean mass, as indicated by the convergence of their lensing profiles above $\sim 1.5\,\mathrm{Mpc}$. This is not the case for the simulated clusters, as is discussed in Section 4.1. This suggests that while dynamical classifications of clusters based on magnitude gaps introduce a bias in mass in the IllustrisTNG simulation, no such bias is introduced for similar classifications in the observed clusters. A significant difference between our simulated and observed cluster samples which may account for these discrepancies is the redshift of the samples. While the IllustrisTNG clusters are all at a particular redshift due to the nature of simulation snapshots, the observed clusters are at a range of redshifts, as reflected in Figure 4.20. Redshift differences and cluster miscentering may account for the differences between the simulated and observed lensing profiles in Figure 4.22. These factors and the differences in the lensing profiles will be explored further in future work, as is discussed in Chapter 5.

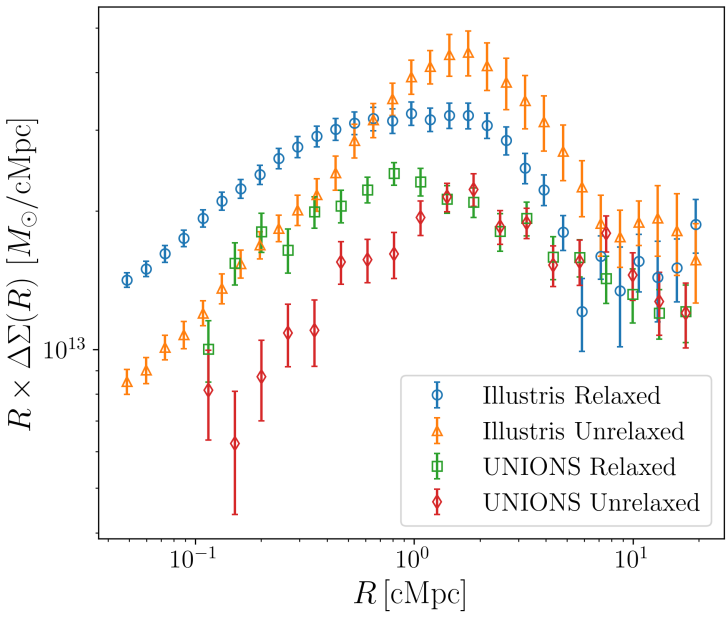


Figure 4.22: The lensing profiles $\Delta\Sigma$ for dynamically relaxed and unrelaxed clusters in the TNG300-1 simulation are compared to those from the DLIS catalogue developed by Wen & Han (2024). The DLIS clusters are split into relaxed and unrelaxed groups by S. Ahad [Ahad et al. in prep], as in Figure 4.19. The simulated clusters are identified in 3D using IllustrisTNG's FoF algorithm and dynamically split based on magnitude gaps analogously to Figure 4.5. The simulated clusters are all at redshift $z = 0.4$, with masses $M_{500c} \geq 7.5 \times 10^{13}\, M_\odot$. This redshift and minimum mass were selected to most closely match the mean redshift and mass of the DLIS sample. The lensing data and uncertainties were computed by C. Mpetha [Mpetha et al. in prep] from the UNIONS shear catalogue (Gwyn et al., 2025). The points for the IllustrisTNG data represent the mean lensing signal for the clusters in each group, and the error bars are the uncertainty on the mean.

Chapter 5

Conclusion

5.1 Summary and Discussion

In this thesis, we sought to relate the structure of galaxy clusters to their mass accretion histories and to compare simulated halos to real observed systems. Our motivation lies in the fact that accurately estimating the formation times of large structures from observational data can in principle break the degeneracy between low-redshift measurements of the cosmological parameters σ_8 and Ω_m. Better low-redshift constraints on our cosmology will help us understand the tension between measurements of these parameters from late- and early-universe structure.

Given the hierarchical formation of structure in the universe as described in Section 1.2, we expect recently formed large systems to have experienced recent mergers. Such systems would be dynamically disturbed due to the mergers, while older systems would be dynamically relaxed. The dynamical state of a cluster is reflected in its structure and should thus be correlated with observable properties. Hence, we target the structural properties of galaxy clusters that are expected to be correlated with their dynamical state as candidates for measurements that reflect the recent mass accretion histories of halos.

In Chapter 3, we compare how well different structural properties of clusters correlate with the mass accretion histories of their halos. We do so by separating clusters into dynamically relaxed and unrelaxed groups based on their structure, then comparing the median mass accretion histories of the halos in each group. This analysis was performed both on structural parameters derived from the total mass distributions of halos and on optical properties of clusters. The structural parameters derived from the total mass distributions of halos are centre of mass offset, axis ratio, concentration and asymmetry. The

optical properties of clusters are galaxy offset, galaxy axis ratio, stellar mass asymmetry and magnitude gap.

From our analysis of the 3D centre of mass offsets of halos and the mass history parameter z_{75}, we found strong evidence for two groups of halos—relaxed and unrelaxed. We found little statistical motivation for splitting the sample into more categories, and so we maintained this binary classification of clusters throughout the rest of our analysis. When splitting the simulated halo sample into dynamically relaxed and unrelaxed groups using any given structural parameter, we found that the median mass accretion histories of these two groups are similar at high redshift, then notably different at low redshift. The dynamically disturbed population of halos has clearly experienced recent major mergers. Following their recent mergers, the unrelaxed halos reach a similar final mass at $z = 0$ as the relaxed group, which accreted its mass earlier. When viewed in projection, the centre of mass offset is able to distinguish between "old" and "young" (i.e. relaxed and unrelaxed) systems fairly well. The projected mass asymmetry of halos does so even more effectively. However, the projected axis ratios and concentrations of halos were not found to be effective at distinguishing young and old clusters. The axis ratio fails to categorise relaxed and unrelaxed halos in part because it loses much of its information when the mass distribution is projected along the line of sight. Halo concentration carries some information about mass accretion, but merging systems have a variety of concentrations that contaminate the trend. Thus, we conclude that with sufficiently precise measurements of the total mass distributions of cluster halos, total mass asymmetry is the most useful parameter in identifying old or young halos. Meanwhile, centre of mass offset is also effective, and concentration could perhaps be used in conjunction with other structural parameters to add more information. Unfortunately, projected axis ratio offers very little information regarding mass accretion history.

The optical properties of clusters can be much more easily measured from observations of clusters than their mass distributions, particularly in large optical or infrared surveys. Since such surveys will contribute most to expanding our cluster catalogues, it is valuable to focus on how the optical properties of clusters relate to their mass accretion histories. Of the optical measurements that we considered, we found that the projected galaxy offset and the galaxy axis ratio perform very poorly at distinguishing systems with different recent mass accretion histories. In contrast, selecting systems based on stellar mass asymmetry and magnitude gaps can quite successfully identify relaxed and unrelaxed halos. From this result, we conclude that the stellar mass asymmetry and magnitude gaps of clusters are the most effective observationally accessible measurements for separating young and old halos.

In Chapter 4, we examined how the projected radial structures of our relaxed and

unrelaxed samples of simulated halos compare to each other, how they compare to samples defined using different structural parameters, and how they compare to analogous samples of real clusters from a DLIS x UNIONS catalogue developed by our collaborators.

To compare the mean projected radial mass structures of cluster samples, we computed their gravitational lensing profiles directly from the mass distributions of the halos. In general, we found that dynamically relaxed clusters have stronger lensing profiles in their cores, indicating steeper density profiles than unrelaxed clusters. We tested these lensing profiles for halo samples classified based on the structural parameters that had the most success at distinguishing halo mass histories in Chapter 3. Namely, we focused on centre of mass offset, halo asymmetry and magnitude gap. Classifications of relaxed and unrelaxed halos based on projected centre of mass offsets produced the least significant difference in the inner lensing profiles of clusters. Despite this, the two groups were still clearly different in their structure. The projected galaxy offset produced a slightly greater difference in the inner structure of clusters. However, the outer regions of the lensing profiles revealed that the relaxed clusters selected based on galaxy offsets were biased to higher masses than the unrelaxed clusters. Dynamical classifications based on both the total and stellar mass asymmetries of halos produced very different inner lensing profiles between relaxed and unrelaxed clusters. They also exhibited no significant mean mass difference between the samples. Interestingly, the stellar mass asymmetry produced more statistically different samples of clusters than the total mass asymmetry, despite not tracing the entire mass distribution. Fortunately, this indicates that the optically accessible measurement of stellar mass asymmetry can distinguish between halos with very different total mass structures and mass accretion histories, as seen in Chapter 3.

Dynamical classification based on magnitude gaps also produced different mass profiles between relaxed and unrelaxed clusters, particularly in the innermost regions. However, the difference from magnitude gap classification is less significant than what is achievable with asymmetry. We also found that magnitude gap classification introduces a significant bias in mass at higher redshift such that the unrelaxed clusters are of much higher mass than the relaxed clusters. This results in different lensing profiles in the outer regions of the clusters. No similar bias is introduced between relaxed and unrelaxed clusters classified based on total or stellar mass asymmetry. This suggests that the halo mass difference at higher redshift is not a generic feature of relaxed and unrelaxed clusters. Rather, it is particular to dynamical classification based on magnitude gaps. This result indicates that over a broader redshift range, asymmetries can more reliably distinguish between dynamically relaxed and unrelaxed clusters than any of the other tested structural parameters. Thus, we recommend the stellar mass asymmetry parameter as an observationally accessible tool for separating dynamically relaxed and unrelaxed clusters with different recent mass

accretion histories. Should measurements of the stellar mass distributions of clusters be inaccessible, magnitude gaps between the brightest galaxies in a cluster can also distinguish between relaxed and unrelaxed clusters, though a redshift-dependent bias in mass may be introduced and should be accounted for.

In order to compare our simulated cluster samples to real observed clusters, we examined the effects of projection along the line of sight and of optical cluster selection on our simulated halo samples. We found that galaxies projected along the line of sight into the inner regions of clusters do not significantly impact the stellar mass functions of relaxed and unrelaxed cluster samples. The characteristic features of the stellar mass functions in both relaxed and unrelaxed clusters were largely preserved under projection rather than washed out. When we classified clusters based on magnitude gaps while including projected galaxies, the mean gravitational lensing profiles of the relaxed and unrelaxed samples were not significantly changed.

We optically selected clusters from our simulation in an analogous fashion to what was done in our DLIS x UNIONS cluster sample in order to best compare IllustrisTNG to the observational data. We found that less than 10% of the mean stellar mass that is apparently in an optically selected cluster is due to projected galaxies. However, the scaling relations used to predict the masses of optically selected clusters significantly overestimate the true masses of the clusters, especially at higher redshift. When the true masses of the clusters are properly accounted for, the mean lensing profiles of optically selected clusters are very similar to those of 3D-identified halos. This holds true for both the total cluster samples and for the relaxed and unrelaxed subsamples. As a result, we conclude that while projection and optical selection may affect the properties of individual clusters, the mean structure of relaxed and unrelaxed samples selected based on magnitude gaps are not significantly affected as long as the halo mass is accurately measured.

To compare our relaxed and unrelaxed clusters from IllustrisTNG to real observed clusters, we collaborated with S. Ahad and C. Mpetha, who worked with the observational catalogues. Ahad selected relaxed and unrelaxed clusters from a DLIS catalogue based on magnitude gaps. The magnitude gaps of these clusters were significantly different from those seen in the simulations. It is not clear how much of this difference is due to the stellar evolution models in the simulations and how much is due to measurement uncertainties in the observations. Despite these differences, the most dynamically relaxed and unrelaxed clusters are selected in each case. Mpetha then used the UNIONS shear catalogue to compute the weak gravitational lensing profiles around the relaxed and unrelaxed clusters. In the observational data, the relaxed halos are again seen to have greater lensing signals in their inner regions compared to unrelaxed halos. We similarly classified our simulated clusters based on magnitude gaps and ensured that the samples had the same mean mass as

determined by fits to the lensing profiles. We found that the clusters in IllustrisTNG have significantly stronger lensing profiles than the observed clusters, despite being of the same mean mass. Ongoing work by Mpetha suggests that this may be due to miscentring on the observed clusters. We also saw that the bias in mass between the relaxed and unrelaxed cluster samples seen in the simulation is not present in the observed lensing profiles. One of the most notable differences between the simulated and real cluster samples is that the simulated clusters are all at a particular redshift of $z = 0.4$, while the observed clusters are at a variety of redshifts. This difference may account for some of the discrepancies between the structures of the simulated and observed systems. All of these differences are discussed further in Section 5.2.

We conclude from the work in Chapter 4 that the projected radial mass structures of cluster samples can be meaningfully compared using gravitational lensing profiles. The degree to which optical classifications of clusters trace the total mass profiles of halos can be identified using gravitational lensing. The differences in structure seen between relaxed and unrelaxed samples, and the stability of the results, trace how well the structural measurements distinguish between halos of different recent mass histories, as seen in Chapter 3. The lensing profiles of simulated halos can also be compared to real observed halos without line of sight projection or optical selection significantly affecting the samples. However, there are notable differences in the structures of relaxed and unrelaxed halos selected based on magnitude gaps in simulations and survey catalogues. These differences are not yet explained, and some remaining questions are addressed in Section 5.2.

5.2 Future Work

The broad aim of this thesis is to study how the observable properties of galaxy clusters can be related to the mass accretion histories of real systems so as to better constrain our cosmology at low redshifts. The conclusion of this work leaves several opportunities for further research, both in addressing some remaining challenges and in further applications of our results.

Firstly, to apply our findings on which structural parameters of clusters best trace their mass accretion histories to real systems, we must ensure that the mass distributions of the simulated and observed clusters are comparable. As was found in Section 4.4, there are significant discrepancies between the mass distributions traced by the gravitational lensing profiles of dynamically relaxed and unrelaxed galaxy clusters in the IllustrisTNG simulation and the DLIS x UNIONS catalogue. Future research will work to resolve these differences from working with both the simulations and the observations. On the simulation side,

we found in Section 4.1 that the dynamical classification of clusters based on magnitude gaps introduces a mass difference between the relaxed and unrelaxed samples at higher redshift. We will work to understand what causes this redshift-dependent bias in mass and why it is not present in the observational data. Additionally, we found the stellar mass asymmetry of clusters is a readily observable parameter that does not produce a similar bias in mass. Thus, we will compare the simulated profiles of halos classified based on asymmetry to similar samples of real clusters. On the observational side, we are working to update our cluster sample to make it more reliable. The current magnitude gap data in the observed cluster sample is based on apparent magnitudes of galaxies rather than their intrinsic magnitudes. This means that we are not comparing precisely the same optical properties between clusters at different redshifts. This may account for some of the differences between the observations and the simulations. The cluster catalogue is being updated to include intrinsic magnitudes using K-correction in order to address this discrepancy. The DLIS cluster sample is also being cross-correlated with other cluster samples with different selection techniques to increase our confidence in the identified clusters and their estimated masses. Additionally, the high-redshift observed clusters in the observed sample have greater uncertainties associated with them, especially with regard to projection. These systems will be removed to increase the reliability of the cluster sample. The narrower redshift range will also make it more comparable to the simulations. Lastly, the issue of miscentring on clusters will be further explored with the weak gravitational lensing profiles to determine whether it can resolve the difference in amplitude between the simulated and observed lensing profiles.

Secondly, we intend to further extend this work so as to better establish the link between galaxy cluster structure and cosmology. The IllustrisTNG simulations have allowed us to identify which structural properties of halos are best correlated to their recent mass accretion histories and to establish how relaxed and unrelaxed halo samples can be compared via lensing profiles. However, we are only able to do so using one cosmology in IllustrisTNG. In order to determine precisely how relaxed and unrelaxed samples of clusters vary as a function of the cosmological parameters σ_8 and Ω_m, their structures and histories must be compared in simulations with different cosmological parameters. The implementation of MHD physics in these simulations must be consistent, as the treatment of baryons can have a notable impact on the results, as discussed in Section 1.4.1. As a result, our future work may include building and running cosmological simulations in a variety of cosmologies on which we can run similar analyses as in this work. The results of this future work will enable us to establish how the observable properties of cluster samples are affected by cosmology. This work will push us toward significantly improving the constraints on our cosmology from measurements of low-redshift structure.

References

Abdalla E., et al., 2022, Journal of High Energy Astrophysics, 34, 49

Adhikari S., Dalal N., Clampitt J., 2016, Journal of Cosmology and Astroparticle Physics, 2016, 022

Akaike H., 1974, IEEE Transactions on Automatic Control, 19, 716

Aliş S., 2024, Journal of Advanced Research in Natural and Applied Sciences, 10, 954

Amoura Y., 2023, PhD thesis, University of Waterloo

Amoura Y., Drakos N. E., Berrouet A., Taylor J. E., 2021, Monthly Notices of the Royal Astronomical Society, 508, 100–117

Anbajagane D., Evrard A. E., Farahi A., 2022, Monthly Notices of the Royal Astronomical Society, 509, 3441–3461

Angulo R. E., Hahn O., 2022, Living Reviews in Computational Astrophysics, 8, 1

Arbey A., Mahmoudi F., 2021, Progress in Particle and Nuclear Physics, 119, 103865

Bartelmann M., 2010, Classical and Quantum Gravity, 27, 233001

Benítez N., 2000, The Astrophysical Journal, 536, 571

Bertone G., Hooper D., Silk J., 2005, Physics Reports, 405, 279

Bett P., 2012, Monthly Notices of the Royal Astronomical Society, 420, 3303–3323

Blumenthal G. R., Faber S. M., Primack J. R., Rees M. J., 1984, Nature, 311, 517

Bullock J. S., Boylan-Kolchin M., 2017, Annual Review of Astronomy and Astrophysics, 55, 343

Condon J. J., Matthews A. M., 2018, Publications of the Astronomical Society of the Pacific, 130, 073001

Conselice C. J., 1997, Publications of the Astronomical Society of the Pacific, 109, 1251

Conselice C. J., 2003, The Astrophysical Journal Supplement Series, 147, 1

Dariush A. A., Raychaudhury S., Ponman T. J., Khosroshahi H. G., Benson A. J., Bower R. G., Pearce F., 2010, MNRAS, 405, 1873

Dey A., et al., 2019, The Astronomical Journal, 157, 168

Duffy A. R., Schaye J., Kay S. T., Vecchia C. D., Battye R. A., Booth C. M., 2010, Monthly Notices of the Royal Astronomical Society, 405, 2161–2178

Engler C., et al., 2021, Monthly Notices of the Royal Astronomical Society, 500, 3957

Euclid Collaboration et al., 2019, Astronomy & Astrophysics, 627, A23

Farahi A., Ho M., Trac H., 2020, Monthly Notices of the Royal Astronomical Society, 493, 1361

Frenk C. S., White S. D. M., 2012, Annalen der Physik, 524, 507

Gilbank D. G., Bower R. G., Castander F. J., Ziegler B. L., 2004, Monthly Notices of the Royal Astronomical Society, 348, 551–580

Gladders M. D., Yee H. K. C., 2000, The Astronomical Journal, 120, 2148

Golden-Marx J. B., et al., 2024, arXiv e-prints, p. arXiv:2409.02184

Guth A. H., 1981, Physical Review D, 23, 347

Gwyn S., et al., 2025, arXiv e-prints, p. arXiv:2503.13783

Hristova K., Wimley W. C., 2023, Public Library of Science One, 18, e0289619

Hubble E. P., 1936, Realm of the Nebulae. Yale University Press

Huterer D., 2023, The Astronomy and Astrophysics Review, 31, 2

Ivezić Ž., et al., 2019, The Astrophysical Journal, 873, 111

Jones L. R., Ponman T. J., Horton A., Babul A., Ebeling H., Burke D. J., 2003, MNRAS, 343, 627

Joudaki S., et al., 2018, Monthly Notices of the Royal Astronomical Society, 474, 4894

Kelkar K., et al., 2023, Astronomy & Astrophysics, 680, A54

Kharchenko N. V., Piskunov A. E., Schilbach E., Röser S., Scholz R. D., 2016, Astronomy & Astrophysics, 585, A101

Komatsu E., et al., 2011, The Astrophysical Journal Supplement, 192, 18

Koussour M., Myrzakulov N., Rayimbaev J., 2024, Advances in Space Research, 74, 1343

Kravtsov A. V., Borgani S., 2012, Annual Review of Astronomy and Astrophysics, 50, 353

Lee C. T., Primack J. R., Behroozi P., Rodríguez-Puebla A., Hellinger D., Dekel A., 2018, Monthly Notices of the Royal Astronomical Society, 481, 4038

Ludlow A. D., Navarro J. F., Li M., Angulo R. E., Boylan-Kolchin M., Bett P. E., 2012, Monthly Notices of the Royal Astronomical Society, 427, 1322

Lynden-Bell D., 1967, Monthly Notices of the Royal Astronomical Society, 136, 101

Macciò A. V., Dutton A. A., Van Den Bosch F. C., Moore B., Potter D., Stadel J., 2007, Monthly Notices of the Royal Astronomical Society, 378, 55–71

Marinacci F., et al., 2018, Monthly Notices of the Royal Astronomical Society, 480, 5113

Merritt D., 1983, Astrophysical Journal, 264, 24

Mo H., van den Bosch F. C., White S., 2010, Galaxy Formation and Evolution. Cambridge University Press, doi:10.1017/CBO9780511807244

Montenegro-Taborda D., Avila-Reese V., Rodriguez-Gomez V., Manuwal A., Cervantes-Sodi B., 2025, Monthly Notices of the Royal Astronomical Society, 537, 3954

More S., 2012, The Astrophysical Journal, 761, 127

More S., Kravtsov A. V., Dalal N., Gottlöber S., 2011, The Astrophysical Journal Supplement, 195, 4

Mpetha C. T., et al., 2025, arXiv e-prints, p. arXiv:2501.09147

Muratov A. L., Kereš D., Faucher-Giguère C.-A., Hopkins P. F., Quataert E., Murray N., 2015, Monthly Notices of the Royal Astronomical Society, 454, 2691

Naiman J. P., et al., 2018, Monthly Notices of the Royal Astronomical Society, 477, 1206

Navarro J. F., Frenk C. S., White S. D. M., 1996, The Astrophysical Journal, 462, 563

Navarro J. F., Frenk C. S., White S. D. M., 1997, The Astrophysical Journal, 490, 493

Nelson D., et al., 2018, Monthly Notices of the Royal Astronomical Society, 475, 624

Onions J., et al., 2012, Monthly Notices of the Royal Astronomical Society, 423, 1200

Ostriker J. P., Steinhardt P. J., 1995, Nature, 377, 600

Paranjape A., Kovač K., Hartley W. G., Pahwa I., 2015, Monthly Notices of the Royal Astronomical Society, 454, 3030

Pillepich A., et al., 2018a, Monthly Notices of the Royal Astronomical Society, 473, 4077

Pillepich A., et al., 2018b, Monthly Notices of the Royal Astronomical Society, 475, 648

Piskunov A. E., Kharchenko N. V., Schilbach E., Röser S., Scholz R. D., Zinnecker H., 2008, Astronomy & Astrophysics, 487, 557

Planck Collaboration et al., 2014, Astronomy & Astrophysics, 571, A16

Planck Collaboration et al., 2016, Astronomy & Astrophysics, 594, A13

Planck Collaboration et al., 2020, Astronomy & Astrophysics, 641, A6

Power C., Knebe A., Knollmann S. R., 2012, Monthly Notices of the Royal Astronomical Society, 419, 1576–1587

Press W. H., Davis M., 1982, The Astrophysical Journal, 259, 449

Räsänen S., Bolejko K., Finoguenov A., 2015, Physical Review Letters, 115, 101301

Renneby M., Henriques B. M. B., Hilbert S., Nelson D., Vogelsberger M., Angulo R. E., Springel V., Hernquist L., 2020, Monthly Notices of the Royal Astronomical Society, 498, 5804

Rephaeli Y., Sadeh S., Shimon M., 2006, Rivista del Nuovo Cimento, 29, 1

Rosati P., Borgani S., Norman C., 2002, Annual Review of Astronomy and Astrophysics, 40, 539

Rudd D. H., Zentner A. R., Kravtsov A. V., 2008, The Astrophysical Journal, 672, 19

Ryden B., 2016, Introduction to Cosmology, 2 edn. Cambridge University Press

Schade D., Lilly S. J., Crampton D., Hammer F., Le Fevre O., Tresse L., 1995, Astrophysical Journal Letters, 451, L1

Schaller M., et al., 2015a, Monthly Notices of the Royal Astronomical Society, 451, 1247–1267

Schaller M., et al., 2015b, Monthly Notices of the Royal Astronomical Society, 452, 343–355

Schaye J., et al., 2015, Monthly Notices of the Royal Astronomical Society, 446, 521

Schaye J., et al., 2023, Monthly Notices of the Royal Astronomical Society, 526, 4978

Schwarz G., 1978, Annals of Statistics, 6, 461

Shirasaki M., Lau E. T., Nagai D., 2018, Monthly Notices of the Royal Astronomical Society, 477, 2804–2814

Shu F. H., 1992, The physics of astrophysics. Volume II: Gas dynamics.. University Science Books

Spergel D. N., et al., 2007, The Astrophysical Journal Supplement Series, 170, 377

Springel V., White S. D. M., Tormen G., Kauffmann G., 2001, Monthly Notices of the Royal Astronomical Society, 328, 726

Springel V., et al., 2018, Monthly Notices of the Royal Astronomical Society, 475, 676

Sunyaev R. A., Zeldovich Y. B., 1972, Comments on Astrophysics and Space Physics, 4, 173

Taylor J. E., 2010, Advances in Astronomy, 2011, 604898

Turner M. S., 1999, Philosophical Transactions of the Royal Society of London Series A, 357, 7

Valentinuzzi T., et al., 2011, Astronomy & Astrophysics, 536, A34

Velliscig M., van Daalen M. P., Schaye J., McCarthy I. G., Cacciato M., Brun A. M. C. L., Vecchia C. D., 2014, Monthly Notices of the Royal Astronomical Society, 442, 2641–2658

Voit G. M., 2005, Reviews of Modern Physics, 77, 207

Wambsganss J., 1998, Living Reviews in Relativity, 1, 12

Wang K., Mao Y.-Y., Zentner A. R., Lange J. U., van den Bosch F. C., Wechsler R. H., 2020, Monthly Notices of the Royal Astronomical Society, 498, 4450

Weinberg D. H., Mortonson M. J., Eisenstein D. J., Hirata C., Riess A. G., Rozo E., 2013, Physics Reports, 530, 87

Wen Z. L., Han J. L., 2013, Monthly Notices of the Royal Astronomical Society, 436, 275

Wen Z. L., Han J. L., 2021, Monthly Notices of the Royal Astronomical Society, 500, 1003

Wen Z. L., Han J. L., 2024, The Astrophysical Journal Supplement Series, 272, 39

Wong A. W. C., Taylor J. E., 2012, The Astrophysical Journal, 757, 102

Wright A. H., et al., 2025, arXiv e-prints, p. arXiv:2503.19441

Zhang B., Cui W., Wang Y., Dave R., De Petris M., 2022, Monthly Notices of the Royal Astronomical Society, 516, 26

Zhang Y., et al., 2024, Monthly Notices of the Royal Astronomical Society, 531, 510